WIND-DRIVEN NEAR INERTIAL OCEAN RESPONSE AND MIXING AT THE CRITICAL LATITUDE

A Dissertation

by

XIAOQIAN ZHANG

Submitted to the Office of Graduate Studies of
Texas A&M University
in partial fulfillment of the requirements for the degree of

DOCTOR OF PHILOSOPHY

May 2009

Major Subject: Oceanography

WIND-DRIVEN NEAR INERTIAL OCEAN RESPONSE AND MIXING AT THE CRITICAL LATITUDE

A Dissertation

by

XIAOQIAN ZHANG

Submitted to the Office of Graduate Studies of
Texas A&M University
in partial fulfillment of the requirements for the degree of

DOCTOR OF PHILOSOPHY

Approved by:

Chair of Committee,	Steven F. DiMarco
Committee Members,	Robert D. Hetland
	David C. Smith, IV
	Ann E. Jochens
	Craig C. Epifanio
Head of Department,	Piers Chapman

May 2009

Major Subject: Oceanography

ABSTRACT

Wind-Driven Near Inertial Ocean Response and Mixing

at the Critical Latitude. (May 2009)

Xiaoqian Zhang, B.S., Ocean University of China;

M.S., Ocean University of China

Chair of Advisory Committee: Dr. Steven F. DiMarco

The spatial structure and temporal evolution of sea breeze and the latitudinal distribution of propagation and mixing of sea breeze driven near-inertial ocean response in the Gulf of Mexico are investigated using comprehensive data sets and a non-linear numerical model. Near 30°N, inertial oceanic response is significantly enhanced by a near-resonant condition between inertial and diurnal forcing frequencies.

Observational results indicate that sea breeze variability peaks in summer and extends at least 300 km offshore with continuous seaward phase propagation. The maximum near-inertial oceanic response occurs in June when there is a shallow mixed layer, strong stratification, and an approximately 10-day period of continuous sea breeze forcing. Near-inertial current variance decreases in July and August due to the deepening of the mixed layer and a more variable phase relationship between the wind and current. River discharge varies interannually and can significantly alter the oceanic response during summer. During 1993, the “great flood” of the Mississippi River deepens the summer mixed layer and reduces the sea breeze response. The near-inertial currents can

provide considerable vertical mixing on the shelf in summer, as seen by the suppression of bulk Richardson number during strong near-inertial events.

Three-dimensional idealized simulations show that the coastal oceanic response to sea breeze is trapped poleward of 30° latitude, however, it can propagate offshore as *Poincare* waves equatorward of 30° latitude. Near 30° latitude, the maximum oceanic response to sea breeze moves offshore slowly because of the near-zero group speed of *Poincare* waves at this latitude. The lateral energy flux convergence plus the energy input from the wind is maximum near the critical latitude, leading to increased vertical mixing. This local dissipation is greatly reduced at other latitudes. Simulations with realistic bathymetry of the Gulf of Mexico confirm that a basin-wide ocean response to coastal sea breeze forcing is established in the form of *Poincare* waves. This enhanced vertical mixing is consistent with observations on the Texas-Louisiana Shelf. Comparison of the three-dimensional and one-dimensional models shows some significant limitations of one-dimensional simplified models for sea breeze simulations near the critical latitude.

DEDICATION

To my wife, Dan Liu,

and

my parents, Zunbao Zhang and Jing Zhang

ACKNOWLEDGEMENTS

I want to express my sincere thanks to the chair of my committee, Dr. Steven DiMarco, for his superb assistance and guidance in the development of my research, and for giving me the opportunities to go on a research cruise, and attend several national conferences to present my research to my colleagues. I want to thank my other committee members: Dr. Robert Hetland for his assistance to set up my numerical model and his guidance to go through the dynamical analysis; Dr. David Smith, IV, for all his invaluable suggestions and comments on my research; Dr. Ann Jochens for her financial support during the first two-year of my study and editorial comments; Dr. Craig Epifanio for his helpful comments of the knowledge of the atmospheric sciences.

Thanks also go to my friends and colleagues and the department faculty and staff for making my time at Texas A&M University a great experience. Sincere thanks go to my parents for their encouragement and to my wife for her patience and love.

I would like to thank the U.S. Department of the Interior Mineral Management Service, whose funding for the Texas-Louisiana Shelf Circulation and Transport Processes Study (LATEX) and Air/Sea interaction Study in the Gulf of Mexico under contract Nos. 1435-01-05-CT-39051 and 1435-0001-30509 made this research possible.

TABLE OF CONTENTS

CHAPTER Page

LIST OF FIGURES

FIGURE Page

FIGURE Page

FIGURE Page

FIGURE Page

FIGURE Page

FIGURE Page

FIGURE Page

FIGURE Page

LIST OF TABLES

CHAPTER I

INTRODUCTION*

1.1. Overview of sea breeze study around the world

The existence of sea breeze circulation patterns in the atmosphere at coastal boundaries was recognized over a century ago (Davis et al. 1890). The diurnal heating of the land surface during summer months produces a land/sea thermal gradient that propagates as an atmospheric gravity current and forces cyclic onshore/offshore wind flows with 24-hour periodicity. Numerous factors can contribute to the strength of the sea breeze, including synoptic and seasonal weather patterns, coastal topography, and latitude. Simpson (1994) provides an overview of many aspects of sea breeze systems. Scatterometer satellite data indicate that sea breeze winds are a ubiquitous feature of all ocean coastlines and can extend 100's km from the coast (Gille et al. 2003; Aparna et al. 2005). Sea breeze winds decrease markedly at latitudes higher than 50°N/S (Gille et al. 2003).

The traditional view of sea breeze is an onshore wind during the day, which replaces convective rising over land. Results presented here and linear theory however indicate that this viewpoint is too simplistic. Linear theory (Rotunno 1983) predicts that

---

This dissertation follows the style of *Journal of Physical Oceanography*.

*Part of this chapter is reprinted with permission from "Near-resonant ocean response to sea breeze on a stratified continental shelf" by X. Zhang, S. DiMarco, D. Smith, M. Howard, A. Jochens, and R. Hetland, *Journal of Physical Oceanography*, Copyright 2009 by American Meteorological Society.

poleward of 30°N/S, sea breeze winds are in phase with the heating cycle, and are onshore (offshore) during the day (night). Equatorward of 30°N/S, however, the same theory predicts that the sea breeze winds are out of phase with the heating cycle, and are offshore (onshore) during the day (night). This different behavior of the sea breeze system on either side of 30°N/S is also seen in nonlinear numerical models and has been attributed to a dominance of the *Coriolis* force over the thermal induced pressure gradient (Yan and Anthes 1987).

1.2. Study of near-inertial oscillations around the world

Near-inertial oscillations have been known as energetic features of the circulation since observations by Helland-Hansen and Ekman (1931) in the Atlantic Ocean. They are seen as clockwise (counterclockwise) rotating, near-circular horizontal currents in the northern (southern) hemisphere (Webster 1968; Munk and Phillips 1968). Many observational, theoretical and numerical studies have suggested that wind is one of the primary energy sources for the near-inertial motions (e.g., Munk and Wunsch 1998). Such motions can be generated by sudden change of the local surface wind stress (e.g., passage of a front, storm, or hurricane), or periodic wind forcing associated with sea breeze near the coast. Locally generated near-inertial motions can propagate in the form of rotationally modified (*Poincare*) internal waves up to thousands of kilometers (Alford 2003). As the inertial energy cascades into small scale motions or produces local vertical shear, it can dissipate and contribute to the ocean mixing.

In the coastal regions, sea breeze has been observed to drive significant near-inertial motions (Rosenfeld 1988; DiMarco et al. 2000; Simpson et al. 2002; Hunter et al. 2007; Zhang et al. 2008; Zhang et al. 2009). At 30° latitude, the diurnal period of sea breeze forcing coincides with the *Coriolis* frequency of planetary rotation resulting in a resonant effect that leads to a maximum ocean near-inertial response. This resonance has been identified by DiMarco et al. (2000) and Zhang et al. (2008) on the Texas-Louisiana Shelf (~30°N) in the Gulf of Mexico and by Simpson et al. (2002) in current meter moorings off the coast of Namibia (~30°S). Because these energetic near-inertial motions have first-baroclinic vertical modal structure (strong velocity shears near the thermocline), they have the potential to promote vertical mixing through a shear-instability (Simpson et al. 2002). Observations on the Texas-Louisiana Shelf in the summer months show that a ~4 m s^{-1} sea breeze (weak in comparison to synoptic winds) can efficiently deepen the summer mixed layer (Zhang et al. 2008). This enhanced mixing by a relatively weak sea breeze near 30° latitude is one of the principal motivations for this study.

To date, the modeling studies of the coastal near-inertial ocean response to wind forcing have focused on one- and two-dimensional simulations. Analytical work (Orlic 1987) and single-point models (Simpson et al. 2002; Rippeth et al. 2002) show the coastal ocean response to wind forcing has a first-baroclinic modal structure. The magnitude of the currents in the lower layer is comparable to (but out of phase with) that in the surface mixed layer, driven by the pressure gradient imposed by the no-flow condition at the land boundary. Cross-sectional two-dimensional models have been used

to study the coastal generation and offshore propagation of internal waves, and examine the interaction between the near-inertial internal waves and along shore flows (e.g., Tintore et al. 1995; Federiuk and Allen 1996). Chen and Xie (1997) reproduced the cross-shelf structure of observed near-inertial oscillations on the Texas-Louisiana Shelf using a cross-section model forced by an impulsive wind. In a more recent work, Xing et al. (2004) found that although the major features of the synoptic wind induced deepening of the thermocline could be reproduced by the single-point model, the absence of propagating internal waves and associated mixing lead to a sharper thermocline than in the three-dimensional model.

So far, most of the modeling studies on wind-driven inertial motions have focused on the ocean response to an impulse of the wind. Little modeling work has been done to study the near-inertial ocean response to periodic sea breeze forcing near the coast. Recent papers by Simpson et al. (2002) and Rippeth et al. (2002) used an idealized single-point model to study the vertical structure of ocean response to sea breeze. In my research, a three-dimensional non-linear oceanic model will be used to study the oceanic response to sea breeze forcing. Results from the three-dimensional simulations are compared with those from simpler one- and two-dimensional simulations to show the limitation of these simplified simulations of sea breeze.

1.3. Physical description of the Texas-Louisiana Shelf

In this research, wind, hydrography, and current data collected over approximately three years during the Texas-Louisiana Shelf Circulation and Transport Processes Study

(LATEX) (Nowlin et al. 1998) were analyzed to study the spatial structure and temporal evolution of sea breeze and near-inertial oceanic response to sea breeze forcing in the northern Gulf of Mexico near the critical latitude. Numerical simulations were performed to extend this research to other latitudes and explore the latitudinal distribution of sea breeze driven propagating inertial internal wave ocean response and associated vertical mixing. Since the observational results focus on the Texas-Louisiana Shelf in the Gulf of Mexico, a brief review of the physical background of this shelf will be described in this section.

The Texas-Louisiana Shelf is one of the northern shelves of the Gulf of Mexico. The Gulf of Mexico is a semi-closed basin with broad and narrow continental shelves surrounding a deep abyss that reaches ~3800 m, which is connected to the open ocean through entrances at the Yucatan Channel and Florida Straits. The shelf width, which is from the coast to ~200 m isobath, is about 200 km and widest near the Texas-Louisiana border. It narrows to about 90 km off the Rio Grande Delta at the border between Mexico and Texas and virtually disappears off the Mississippi Delta near the mouth of the Mississippi River. The area of this shelf is approximately 105 km^2 (Etter et al. 2004).

The annual low-frequency circulation on the Texas-Louisiana Shelf is primarily driven by wind. The dominant feature of the prevailing circulation on this shelf is a cyclonic elongated gyre, with inshore westward flow near the coast and eastern flow near the shelf break at about the 200-m isobath (Cochrane and Kelly 1986; Cho et al. 1998; Nowlin et al. 2005). In the non-summer months (approximately September through June), the winds are downwelling-favorable, drive the currents

downcoast, and transport the freshwater away from Louisiana to Texas. The mean wind stress changes direction in June from predominantly westward to north and northeast, which interrupts the gyre and results in a current reversal to eastward flow over the shelf (Cochrane and Kelly 1986; Nowlin et al. 1998; Wang et al. 1998). The gyre is normally absent in July, but reapprears as the prevailing wind direction shifts back to the west in August-September (Cochrane and Kelly 1986).

The circulation patterns of the outer Texas-Louisiana Shelf are highly influenced by motions of the Loop Current and its eddies (Nowlin et al. 2001; Sturges et al. 2005; Nowlin et al. 2005). The Loop Current is a portion of the Atlantic western boundary current. It flows northward through the Yucatan Channel, and makes a sharp 90° clockwise turn at approximately 26°N to exit the Gulf at the Florida Straits (Leben 2005). Loop Current Eddies up to 400 km in diameter separate from the Loop Current at an average frequency of 11 months and move westward in the Gulf due to topographic and planetary beta effects (Sturges and Leben 2000). The Loop Current Eddies with strong current velocities up to 2.5 m s^{-1} can interact with the currents on the outer edge of the Texas-Louisiana Shelf. The estimates of kinetic energy show peaks in the mesoscale band of the spectrum, corresponding to the mesoscale Loop Current Eddies (Nowlin et al. 2005). The offshore circulation features are episodic in nature due to the chaotic character of the Loop Current intrusions into the northern Gulf of Mexico and the non-regular separation of periods of the Loop Current Eddies (Sturges and Leben 2000; Leben 2005).

The physical and biochemical activities on the Texas-Louisiana Shelf are highly

affected by the Mississippi-Atchafalaya River System discharge, which has an average annual outflow of about 530 km^2 of water (Milliman and Meade 1983), and constitutes 55% of the total freshwater input to the Gulf of Mexico (Solis and Powell 1999). The Mississippi River discharges onto the Louisiana Shelf through the delta at about 89°W, 29°N. The mean annual discharge of the Mississippi River at Tarbert Landing, LA, is approximately 13,500 $m^3 s^{-1}$, 50% of which goes west and enters the Texas-Louisiana Shelf (Dinnel and Wiseman 1986; Etter et al. 2004). The Atchafalaya River discharges onto the Louisiana Shelf through Atchafalaya Bay near Morgan City, LA, at about 91.5°W, 29.3°N. It constitutes approximately 30% of the total Mississippi-Atchafalaya discharge. The huge amount of fresh water discharge from the Mississipi-Atchafalaya River system can significantly influence the stratification on the Texas-Louisiana Shelf, and thus the physical and biochemical activities. The freshwater from this system exhibits an annual cycle that is dominated by the spring flood (Dinnel and Wiseman 1986). Maximum shelf freshwater volume occurs approximately one month after peak spring runoff, while minimum freshwater volume occurs just prior to the spring maximum. Etter et al. (2004) estimated monthly mean freshwater budgets for the Texas-Louisiana Shelf for the period May 1992 to November 1994 using the hydrographic and meteorological data.

The tides on the Texas-Louisiana Shelf are small. DiMarco and Reid (1998) studied the eight principal tidal current constituents (O1, K1, P1, Q1, S2, M2, K2, and N2) using the current measurements collected from 81 current meter measurements deployed on the Texas-Louisiana Shelf from 1992-1994. Tides in the region are predominantly

diurnal. The dominant tidal constituents are found to be K1, O1, and M2. The largest tidal surface current is about 9 cm s^{-1} at the northeast corner of the shallow shelf near the Atchafalaya Bay. The tidal current decreases to about 2 cm s^{-1} at the shelf edge (DiMarco and Reid 1998). New results shown here, however, indicate that some shallow water tides are important inshore of the 50-m isobath on this shelf.

The strength and frequency of synoptic frontal passages increase during the nonsummer months (Nowlin et al. 1998). These can break down the stratification of the water column through the shear mixing processes. In summer, the infrequency of atmospheric fronts allows the shelf to remain stratified and inhibits vertical mixing. Therefore, the seasonal pattern of frontal passages favors the establishment of strong stratification on the Texas-Louisiana Shelf in summer. However, the research shown here will demonstrate that sea breeze, which peaks in summer, can act as a substitute for winter frontal passages and can drive significant near-inertial motions in the water column and enhance the vertical mixing in the summer months. The eastern Texas-Louisiana Shelf experiences seasonal near-bottom hypoxia (dissolved oxygen concentration less than 1.4 ml l^{-1}) (Rabalais et al. 2007). The sea breeze driven near-inertial motions provide a potential mechanism to ventilate seasonally occurring near-bottom hypoxic waters of the coastal ocean.

1.4. Scientific questions and hypotheses

Although, some progress has been made in our understanding of the spatial and temporal characteristics of sea breeze and associated sea breeze driven oceanic near-

inertial motions in the Gulf of Mexico (DiMarco et al. 2000), there are still many fundamental issues that are not well understood. The main questions include: what are the temporal and spatial characteristics of sea breeze forcing; what is the seasonal variability of sea breeze driven near-inertial currents over the whole Texas-Louisiana Shelf and on a longer time scale than previously considered; what is the role of river discharge in controlling the generation and distribution of near-inertial oceanic responses; how does the coastal-generated sea breeze driven oceanic near-inertial energy propagate in the form of waves; and how do these near-inertial motions contribute to the vertical mixing on the continental shelf in the Gulf of Mexico. The research outlined here aims at testing four specific hypotheses regarding sea breeze and the associated near-inertial oceanic motions in the Gulf of Mexico:

(1) Sea breeze forcing is not trapped to the coast, but can extend at least 300 km offshore.

(2) The combination of river-associated stratification and critical latitude intensifies the diurnal current driven by sea breeze.

(3) Coastal generated, sea breeze driven, near-inertial energy can propagate offshore in the form of internal inertial-gravity waves in the Gulf of Mexico. This offshore propagation varies with latitudes.

(4) The combination of maximum oceanic response to sea breeze near the critical latitude and the low group speed of inertial-gravity waves causes promotion of vertical mixing on the northern continental margins in the Gulf of Mexico.

The overall goal of this dissertation is to examine the temporal evolution and spatial structure of sea breeze winds and near-inertial oceanic response to sea breeze forcing on the Texas-Louisiana Shelf (~30°N) in the Gulf of Mexico using both an extensive data set of hydrography, wind and current collected over approximately 3 years and numerical simulations of a fully non-linear oceanic model. Despite the fact that the emphasis here is on the Texas-Louisiana Shelf in the Gulf of Mexico, these results have significant applications for other coastal oceans near 30°N/S. Likely examples are the East China Sea where there is a broad shelf and large river inflow from the Yangtze River, the Mid-Atlantic Bight region of the eastern U.S. coastline, and the Persian/Arabian Gulf.

1.5. Organization

Chapter II presents the overview of the data and research methods used in this study. The general description of the LATEX data sets, data analysis methods, numerical model, and numerical experiment setup is provided.

Chapter III covers the results from the LATEX observations. In particular, I focus on the following four new objectives: (1) to characterize the spatial structure of sea breeze forcing and near-inertial oceanic response in summer on the Texas-Louisiana Shelf; (2) to explain the occurrence of maximum near-inertial responses to sea breeze forcing in June; (3) to examine the influence of buoyancy forcing from the Mississippi River discharge on the near-inertial response to sea breeze forcing on the Texas-

Louisiana Shelf; and (4) to explore the effect of sea breeze driven near-inertial motions on the promotion of vertical mixing on the Texas-Louisiana Shelf.

Chapter IV covers the results from numerical modeling. The goals of this chapter are to explore the latitudinal dependence of lateral propagation of sea-breeze driven near-inertial motions, and to offer an explanation for the enhanced vertical mixing by these sea-breeze driven motions at the critical latitude based on an examination of the energy budget.

Chapter V discusses the observational and numerical results presented in Chapters III and IV. The critical mechanism between sea breeze and near-inertial motions is compared with other critical mechanisms.

Chapter VI summarizes results presented in Chapters III, IV, V, and provides the conclusions.

At this point of writing (February 1, 2009), two manuscripts based on this dissertation have been submitted to Journal of Physical Oceanography for possible publication. These two papers, focusing on observational analysis and numerical simulations, are referred to herein as Zhang et al. (2008) and Zhang et al. (2009), respectively.

CHAPTER II

DATA AND RESEARCH METHODS*

As indicated by the research objectives, a combination of *in situ* sampling and numerical modeling is used to investigate the spatial structure and temporal evolution of sea breeze and associated sea breeze driven near-inertial motions on the Texas-Louisiana Shelf near the critical latitude of 30°N. The field observations of hydrography, current, and wind collected during the LATEX project are used to accomplish these goals. The purposes of the numerical experiments are (1) to test the dynamical hypotheses found from the observational results; (2) to study the offshore propagati[1]on of sea-breeze driven near-inertial energy; (3) to explain the enhanced vertical mixing by sea breeze driven near-inertial motions near 30° latitude; and (4) to examine the oceanic response to sea breeze forcing at other latitudes, and compare the results with those observed near 30°N. These four aspects are unable to be addressed only using the field observations.

2.1. Description of the LATEX data sets

LATEX was supported by the Minerals Management Service (MMS) of the U.S. Department of the Interior. It covered the Texas-Louisiana continental shelf from the

* Part of this chapter is reprinted with permission from "Near-resonant ocean response to sea breeze on a stratified continental shelf" by X. Zhang, S. DiMarco, D. Smith, M. Howard, A. Jochens, and R. Hetland, *Journal of Physical Oceanography*, Copyright 2009 by American Meteorological Society.

10-m isobath to the continental slope between the Mississippi River and the Rio Grande (Fig. 2.1). The field work of the LATEX study was conducted between April 1992 and December 1994 (Nowlin et al. 1998). It consisted of five field components: moored ocean measurements, drifting buoys, hydrography, acoustic Doppler current profiling (ADCP), and meteorological measurements. Historical and concurrent data sets were assembled. Twenty-eight cruises were conducted during the LATEX field program; 18 were mooring deployment or maintenance cruises (Table 2.1) and 10 were hydrographic/ADCP cruises. Data considered in this study include: meteorological fields (Wang et al. 1996), moored current meter measurements (DiMarco et al. 1997), and hydrography (Jochens et al. 1998; Howard and DiMarco 1998). The data collected from the hydrographic cruises are not used in this analysis. The locations of the moorings and meteorological measurements are displayed in Figs. 2.2 and 2.3.

2.1.1. Wind observations

A network of wind observations was maintained at eight meteorological buoys over the northwestern Gulf of Mexico throughout the LATEX study (Wang et al. 1996). The LATEX wind observations, in combination with the meteorological measurements collected from six National Data Buoy Center (NDBC) buoys, and nine Coastal-Marine Automated Network (C-MAN) sites (Fig. 2.3), were used in this dissertation to study the temporal evolution and spatial structure of sea breeze on the Texas-Louisiana Shelf. All wind products have a one-hour temporal sampling interval. A detailed description of the meteorological measurements is shown in Table 2.2.

Table 2.1. Current mooring deployment/maintenance cruise schedule with dates based on UTC.

Cruise #	Start Date	End Date
M01	4/7/92	4/16/92
M02	5/26/92	6/4/92
M03	7/13/92	7/27/92
M04	8/28/92	9/6/92
M05	10/13/92	10/23/92
M06	12/8/92	12/18/92
M07	1/9/93	1/21/93
M08	7/13/93	7/19/93
M09	5/18/93	5/28/93
M10	7/13/93	7/19/93
M11	9/21/93	10/1/93
M12	12/3/93	12/13/93
M13	2/9/94	2/16/94
M14	3/21/94	4/1/94
M15	5/26/94	6/1/94
M16	7/23/94	8/2/94
M17	9/27/94	10/4/94
M18	11/29/94	12/7/94

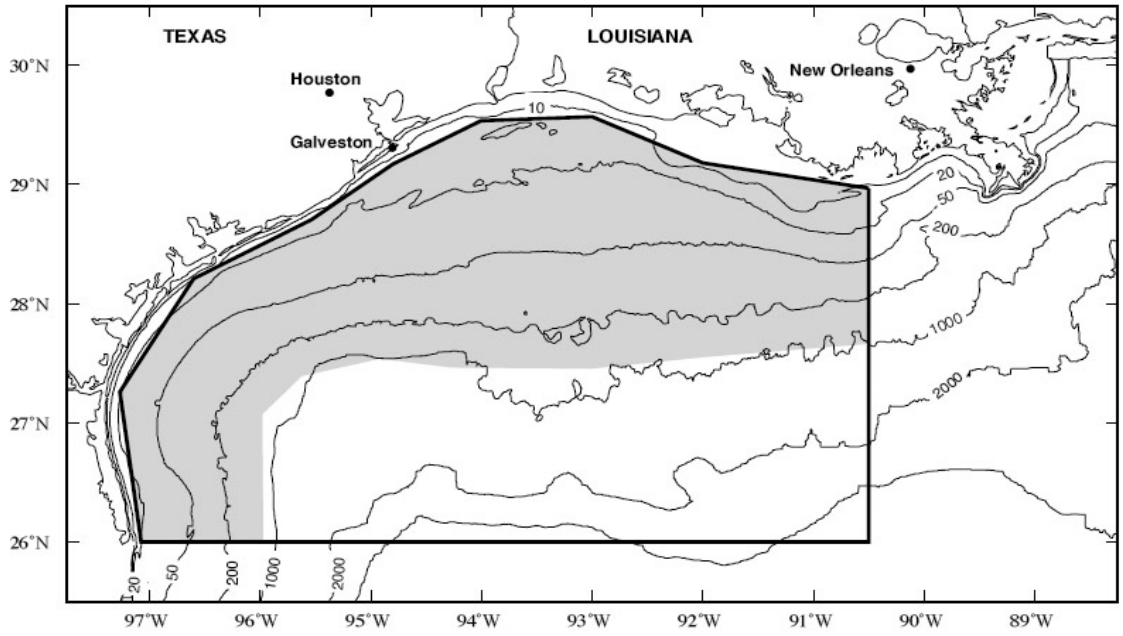

Fig. 2.1. Study area and bathymetry for the LATEX program over the Texas-Louisiana shelf and slope. LATEX hydrography stations and moorings were located over the shelf region within the shaded area. LATEX used data obtained mostly from other studies to examine the slope regime (from Nowlin et al. 1998).

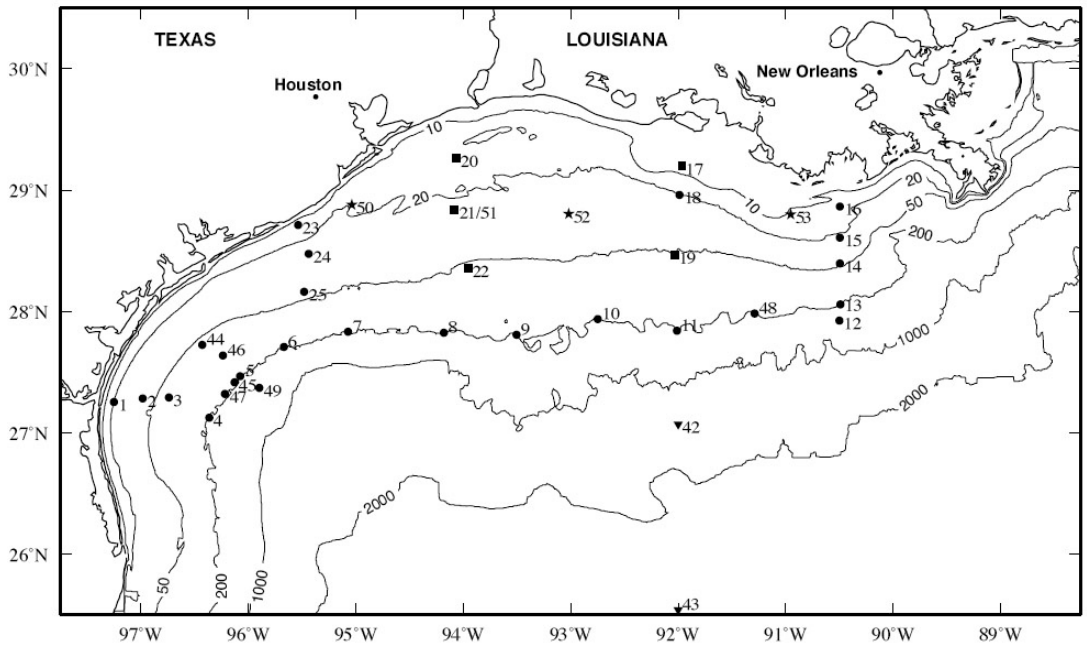

Fig. 2.2. Locations for LATEX current meter moorings and meteorological buoys (solid circle denotes a current mooring, star a meteorological buoy, square a current mooring with meterological buoy attached, and triangle an inverted echo sounder) (from Nowlin et al. 1998).

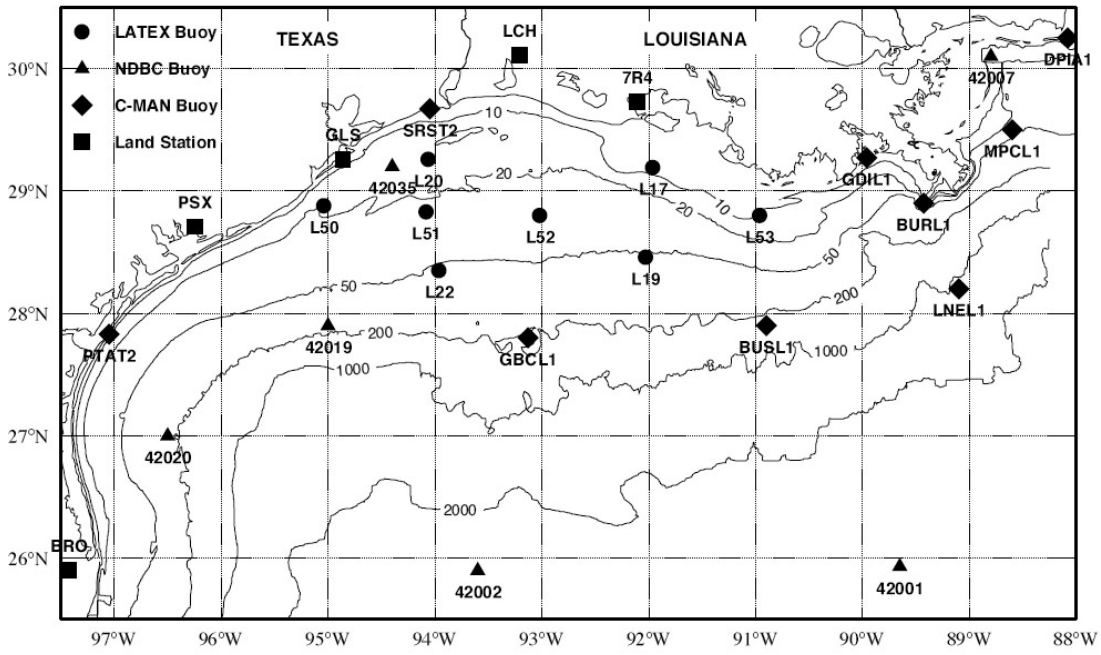

Fig. 2.3. Locations of observing stations in the construction of the LATEX surface meteorological fields (from Nowlin et al. 1998).

2.1.2. Moored time series

Horizontal current velocity, temperature, and conductivity (salinity) were observed with 81 current meters from April 1992 through November 1994 at 31 mooring locations on the Texas-Louisiana Shelf (DiMarco et al. 1997). These current meters recorded at 5-min to 2-hour intervals; however, most recorded at 30-min. Raw data were first 3-hour, low-pass filtered using Lanczos filters to reduce high-frequency sampling noise. Filtered data were subsequently resampled to 1-hour intervals. Data gaps of less than 6 hours (mainly due to instrument replacement) were filled using linear interpolation, while longer gaps were filled using a maximum entropy (spectral-preserving) method

(DiMarco et al. 1997; DiMarco and Reid 1998). A detailed description of all the mooring locations is shown in Table. 2.3.

Table 2.2. Positions and instrument heights for meteorological stations used in this dissertation.

Buoy	Lat. (°N)	Long.(°W)	Anemometer Ht (m)	Thermometer Ht (m)	Type
Met17	29.19	91.96	3.6	3.0	LATEX
Met19	28.46	92.03	3.6	3.0	LATEX
Met20	29.26	94.06	3.6	3.0	LATEX
Met22	28.35	93.96	3.6	3.0	LATEX
Met50	28.88	95.04	3.6	3.0	LATEX
Met51	28.83	94.08	3.6	3.0	LATEX
Met52	28.80	93.02	3.6	3.0	LATEX
Met53	28.80	90.96	3.6	3.0	LATEX
42001	25.90	89.70	10.0	10.0	NDBC
42002	25.90	93.60	10.0	10.0	NDBC
42007	30.10	88.80	10.0	10.0	NDBC
42019	27.90	95.00	5.0	5.0	NDBC
42020	27.00	96.50	5.0	4.0	NDBC
42035	29.20	94.40	5.0	4.0	NDBC
BURL1	28.90	89.43	33.8	13.7	CMAN
BUSL1	27.90	90.90	93.6	21.3	CMAN
DPIA1	30.25	88.08	17.4	9.1	CMAN
GBCL1	27.37	93.80	57.6	57.6	CMAN
GDIL1	29.27	89.96	17.6	17.0	CMAN
LNEL1	28.67	89.17	60.0	34.7	CMAN
MPCL1	29.50	88.60	40.2	40.2	CMAN
PTAT2	27.83	97.05	14.9	9.1	CMAN
SRST2	29.67	94.05	13.4	12.8	CMAN
7R4	29.73	92.11	10.0	1.5	Airport
BRO	25.90	97.43	10.0	1.5	Airport
GLS	29.26	94.86	10.0	1.5	Airport
LCH	30.11	93.21	10.0	1.5	Airport
PSX	28.71	96.25	10.0	1.5	Airport

Table 2.3. Locations of current meter moorings as initially deployed with depth of the water at each site and the planned mooring maintenance interval.

Mooring Number	Latitude (°N)	Longitude (°W)	Water Depth (m)	Maintenance Interval (Days)
1	27.256	97.246	20	45/120
2	27.284	96.980	37	45/120
3	27.290	96.736	65	90/120
4	27.126	96.358	200	90/120
5	27.468	96.073	200	90/120
6	27.708	95.664	201	90/120
7	27.834	95.069	200	90/120
8	27.825	94.179	200	90/120
9	27.808	93.503	200	90/120
10	27.936	92.745	201	90/120
11	27.842	92.009	200	90/120
12	27.924	90.495	504	180/180
13	28.058	90.486	200	90/120
14	28.395	90.493	47	45/60
15	28.608	90.492	27	45/60
16	28.867	90.491	18	45/60
17	29.196	91.965	8	45/60
18	28.963	91.983	22	45/60
19	28.465	92.035	53	45/60
20	29.261	94.064	14	45/60
21	28.837	94.080	24	45/60
22	28.356	93.956	55	45/60
23	28.713	95.536	15	45/60
24	28.474	95.437	28	45/60
25	28.162	95.476	37	45/60
42	27.069	92.001	1890	360/360
43	25.542	92.000	3130	360/360
44	27.726	96.424	57	90/120
45	27.418	96.126	198	90/120
46	27.638	96.234	91	90/120
47	27.322	96.213	204	90/120
48	27.983	91.283	201	90/120
49	27.369	95.894	502	180/180

Principal tidal constituents (e.g., O1, K1, P1, Q1, S2, M2, K2, and N2 etc.) were removed from the current measurements using the T_Tide Harmonic Analysis Toolbox of Pawlowicz et al. (2002) to eliminate the influence of principal tidal energy. Estimated amplitudes of diurnal tidal current components average around 5 cm s^{-1} on the Texas-Louisiana Shelf (DiMarco and Reid 1998). These detided data are used for the analyses in this dissertation.

2.1.3. Hydrographic data

Eighteen mooring maintenance cruises were undertaken during the LATEX study with a general interval of 60 days for the shallow water moorings (Table 2.1). CTD casts were taken during these cruises using a Sea-Bird SBE 19 self-contained CTD profiling instrument (Howard and DiMarco 1998). These casts were usually taken prior to recovering and after deploying mooring instruments. These hydrographic profiles were used to show the seasonal variability of stratification at the mooring locations on the Texas-Louisiana Shelf.

2.2. Data methods: wavelet analysis

Wavelet analysis has been used in previous studies to examine the temporal variability of ocean currents at certain frequency band (e.g., Schott et al. 2005; Bunge et al. 2006). To study the temporal evolution of different frequency components, especially the near-inertial component, wind and current measurements are analyzed with the wavelet transform. The wavelet package developed by Torrence and Compo (1998,

hereafter TC98) is used for this study. The wavelet base function is chosen to be Morlet, which is typically used in geographical data analysis. The functional form of the Morlet wavelet is comprised of a complex exponential modulated by a Gaussian envelope: $e^{i\omega_0 t/s}e^{-t^2/(2s^2)}$, where t is the time, s is the wavelet scale, and ω_0 is a non-dimensional frequency. For $\omega_0 = 6$, used here, there are approximately three oscillations within the Gaussian envelope. The window width of the Morlet wavelet is approximately $2 * \sqrt{2} * period$, and so is a function of the period of oscillation being analyzed (Torrence and Compo 1998). Therefore, for the near-inertial motions (~1 day period) on the Texas-Louisiana Shelf, the window width of the Morlet wavelet is ~2.8-day (Fig. 2.4). For the Morlet wavelet, the wavelet scale s is almost identical to the corresponding Fourier period of the complex exponential; hence, the two terms "scale" and "period" are used interchangeably in this study. A recent report that a bias problem in TC98 is also removed based on Liu et al. (2007). Further details on wavelet analysis can be found in Foufoula-Georgiou and Kumar (1995).

The main objective of this dissertation is to study the temporal variability that is associated with sea breeze forcing. Therefore, after the wavelet spectrum is estimated, the variance associated with periods near 24 hours, i.e., the near-inertial band, are calculated and analyzed. The definition of the near-inertial band used here is from 20 hr (0.83 cpd) to 28 hr (1.17 cpd), which covers both the diurnal period and inertial periods at the mooring locations on the Texas-Louisiana Shelf (Fig. 2.2).

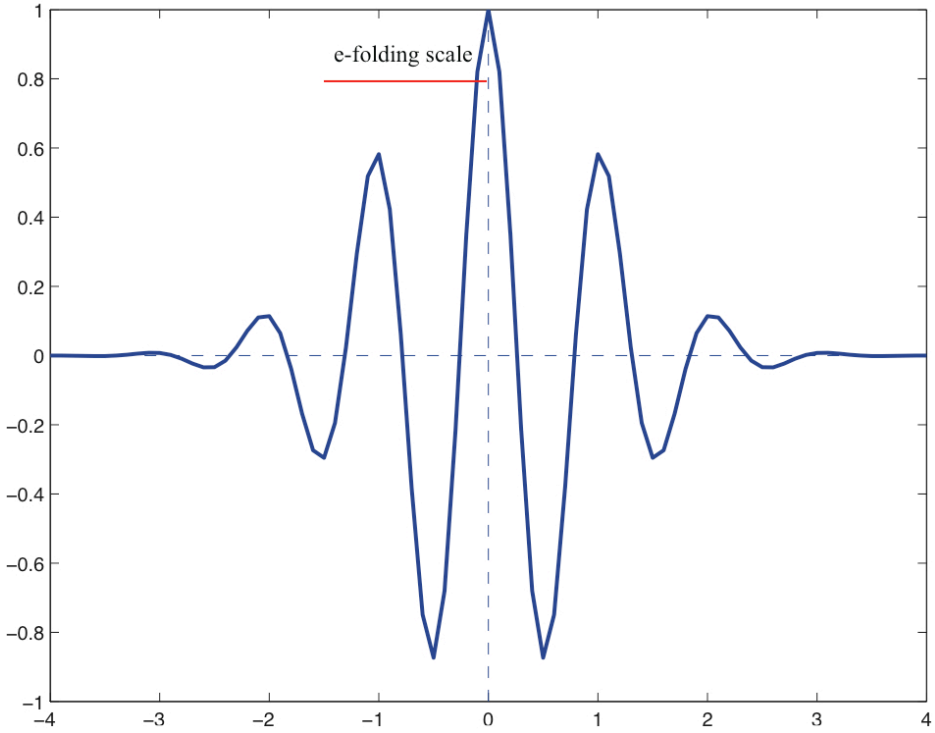

Fig. 2.4. Morlet wavelet for the diurnal-inertial band motions (s=1).

2.2.1. Wavelet power spectrum

The wavelet power spectrum, defined as the squared absolute value of the wavelet transform, estimates the variance at each period as a function of time. To test the confidence of peaks in the wavelet power spectrum, an appropriate background spectrum is needed. Based on the data analyzed in this dissertation, a theoretical red-noise wavelet power spectrum (TC98) is used to establish a null hypothesis for the confidence of a peak in the wavelet power spectrum. The wavelet power spectrum then is distributed as a chi-square about the background spectrum.

2.2.2. Wavelet coherency spectrum

In this dissertation, the wavelet-squared coherency is used to study the temporal change of coherency for a given frequency band. The cross-wavelet spectrum is defined as

$$W_n^{xy} = W_n^x(s)W_n^{y*}(s), \tag{2.1}$$

where $W_n^x(s)$ and $W_n^y(s)$ are the wavelet transforms of two time series X and Y respectively, n is the time index, s is the scale, and (*) indicates complex conjugate. The wavelet squared coherency then is defined as the squared absolute value of the smoothed cross-wavelet spectrum, normalized by the smoothed wavelet power spectra,

$$\gamma_n^2(s) = \frac{\left|\left\langle s^{-1}W_n^{xy}(s)\right\rangle\right|^2}{\left\langle s^{-1}\left|W_n^x(s)\right|^2\right\rangle\left\langle s^{-1}\left|W_n^y(s)\right|^2\right\rangle}, \tag{2.2}$$

where $\langle\cdot\rangle$ indicates ensemble averaging in both time and scale (Torrence and Webster 1999).

The statistical confidence level of the wavelet coherence is estimated using Monte Carlo methods. A large number (300 in this dissertation) of red noise time series pairs with similar distribution of the data are generated (Fig. 2.5). For each pair, the wavelet coherence is calculated, and the confidence level for each scale is then estimated based on this large set of wavelet coherence spectra. A detailed description of how the confidence level is estimated for the wavelet coherency spectrum can be found in Grinsted et al. (2004), and TC98.

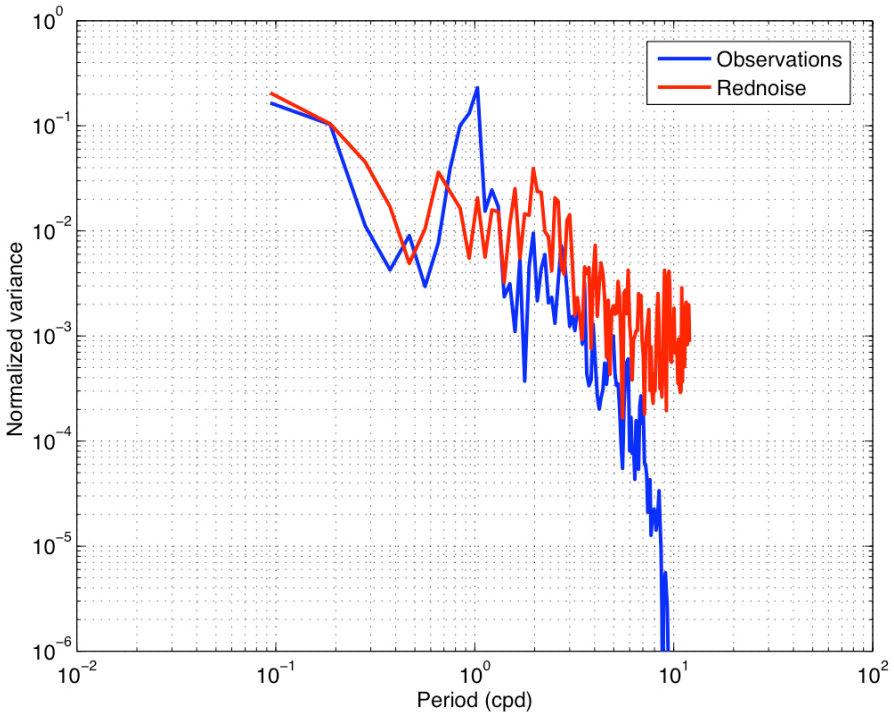

Fig. 2.5. Comparison of the spectrum of the current measurements in June 1994 at mooring 22 and the spectrum of the red noise time series generated by the wavelet package. Note: the current data have been detided and 3-hr low-passed filtered.

2.3. Numerical methods

The hydrodynamic simulations were performed using the Regional Ocean Modeling System (ROMS-3.0). ROMS-3.0 is a free-surface and terrain-following ocean model widely used by the scientific community for a diverse range of applications (Shchepetkin and McWilliams 2005). In this dissertation, one- and three-dimensional idealized simulations and three-dimensional realistic simulations are conducted. The water depth is uniform in the idealized cases. In the realistic case, the numerical domain covers the entire Gulf of Mexico, and orthogonal-curvilinear coordinate grids are used

for calculation, with the grid focused in the north-western section of the Gulf where grid resolution is about 5 km. The realistic model configuration is identical to that used for the Texas Automated Buoy System (TABS) modeling effort, which is a real-time nowcast/forecast of surface currents over the Texas-Louisiana continental shelf (Hetland and Campbell 2007). Real-time TABS model results are available at http://seawater.tamu.edu/tglo. The lateral boundaries in the one-dimensional idealized and three-dimensional realistic model simulations are set to periodic open boundaries and no slip walls, respectively. Radiation open boundary conditions are used for the three-dimensional idealized experiments, and a Flather (1976) condition with no mean barotropic background flow is used for the two-dimensional velocities and free surface. In order to minimize the effect of reflection of waves at the open boundary, a sponge layer is also applied, in which horizontal mixing in the region of the open boundary is increased to avoid spurious reflection of internal waves. The common turbulence closure scheme $k-\varepsilon$ (Umlauf and Burchard 2003) is used to calculate vertical mixing in all the numerical experiments. The background, or minimum, mixing is 5×10^{-6} m^2 s^{-1} for both momentum and tracers. These and other parameters used by the closure scheme are the default parameters for ROMS version 3.0.

All numerical experiments are forced by analytical wind stress, and sea surface heat flux (including short wave, long wave, latent, and sensible heat fluxes). Sea breeze is simulated by imposing a clockwise-rotating 24-hr periodic wind field with a maximum magnitude of 4 m s^{-1} at the coast, gradually decreasing to zero amplitude at ~300 km from the boundary. The magnitude and extent of sea breeze is chosen to approximately

simulate strong sea breeze situations, which have been observed in the summer months in the Gulf of Mexico (Zhang et al. 2008). Daily diurnal cycling of the solar heat flux is represented by the positive lobes of a clipped sinusoidal signal that reaches a midday (1200 local) maximum of 150 W m^{-2}. The salinity field is constant (35 psu). In the subsequent calculations, initial temperature vertical profiles are based upon climatological observations in the Gulf of Mexico in the summer months and correspond to a surface mixed layer of approximately 10 m. Below 10 m, the temperature decreases exponentially. The model uses a full equation of state to calculate density from temperature and salinity. In all numerical experiments, the model is forced from rest.

A range of non-linear models, from a simple one-dimensional model to a three-dimensional model of the Gulf of Mexico incorporating realistic topography, are performed. I will examine the characteristics of fields including sea surface elevation, temperature, currents, stratification, shear, and vertical eddy viscosity (vertical temperature diffusivity has similar pattern, so in this study only vertical eddy viscosity is examined and it is referred to as vertical mixing coefficients later in the rest of this dissertation). The model output will be compared qualitatively with the current and hydrographic observations collected from the LATEX moorings and cruises (Zhang et al. 2008; Nowlin et al. 1998; DiMarco et al. 1997).

CHAPTER III

OBSERVATIONAL RESULTS*

3.1. Temporal evolution and spatial structure of winds

In this section, I present an analysis of the meteorological forcing in the northwest Gulf of Mexico to characterize the spatial structure and temporal evolution of sea breeze based on the wind measurements described in chapter II.

3.1.1. Sea breeze as the primary driver of summer diurnal wind variability

First, I consider the establishment of sea breeze as the primary driver of summer diurnal wind variability in the northern Gulf of Mexico. The presence of diurnal period wind energy is an assumption for the occurrence of land/sea breeze and has been used to identify land/sea breeze regimes (Rotunno 1983; Masselink and Pattiaratchi 2001; Hyder et al. 2002; Simpson et al. 2002). Diurnal winds may be forced by mechanisms other than sea breeze on the Texas-Louisiana Shelf, these may include diurnal tides, reflection effect of clouds, synoptic winds, feedback effect of diurnal va^{2}riation of the air-sea temperature difference, and near-inertial high-pressure gradients in the atmosphere (Chen et al. 1996; Hunter et al. 2007).

---

* Part of this chapter is reprinted with permission from "Near-resonant ocean response to sea breeze on a stratified continental shelf" by X. Zhang, S. DiMarco, D. Smith, M. Howard, A. Jochens, and R. Hetland, *Journal of Physical Oceanography*, Copyright 2009 by American Meteorological Society.

However, for the summer months (~ the focus period of this study) on the Texas-Louisiana Shelf, I determined that all of these are secondary to sea breeze forcing for the following reasons. A harmonic analysis was performed to extract the diurnal tidal components from the wind time series and found the diurnal tidal wind energy can contribute at most 10 percent of the diurnal band wind energy. The cloud cover feedback effects would only occur locally under cloud-covered regions. Synoptic winds are weak on the Texas-Louisiana Shelf in the summer period with an average value of approximately 1 event in June and July (Nowlin et al. 1998). The feedback effect of the air-sea temperature difference on diurnal winds on the Texas-Louisiana Shelf was tested by Chen et al. (1996), and was found to be negligible.

The final mechanism of a diurnal atmospheric pressure gradient was identified by Chen et al. (1996) by analyzing meteorological data 100 km offshore in the Gulf. I interpret this pressure gradient in summer to be mainly sea breeze related for three reasons. Firstly, from the diurnal wind ellipses in summer 1992 at stations SRST2, 51, 22, GBCL1 and 42002 (see Fig. 2.3 for locations), the phase propagation of the diurnal wind signal can be seen from the coast to 300 km offshore (Section 3.1.3 below). Secondly, the Fourier spectrum for the summer and non-summer wind measurements was calculated at NDBC buoy 42002 (more than 300 km offshore) separately. The summer diurnal band wind energy is about four times as large as that of the non-summer seasons (not shown). The significant summer enhancement of diurnal peak at NDBC buoy 42002 and the clear phase propagation of the sea breeze signal offshore corroborate the fact that it is sea-breeze driven. Thirdly, large scale synoptic wind events (i.e.,

atmospheric fronts) are rare on the Texas-Louisiana Shelf in the summer period with an average of approximately 1 event per month in June and July (Nowlin et al. 1998; DiMego et al. 1976).

For these reasons, the dominant temporal and spatial structure found for the diurnal winds on the Texas-Louisiana Shelf in summer will be considered to represent that of sea breeze. During the non-summer seasons, sea breeze becomes weaker and other mechanisms could contribute more to the diurnal wind energy. This hypothesis is consistent with the climatology of the land/sea breeze system that indicates the majority of land/sea breeze days occur during the hot summer season due to the day-night variation of the temperature gradient between the land and the sea, with few in winter and the transitional periods in the spring and fall (Hsu 1972; Hunter et al. 2007; Masselink and Pattiaratchi 2001; Furberg et al. 2002).

3.1.2. Temporal evolution

The wavelet power spectrum for the east-west wind component at NDBC buoy station PTAT2 (Fig. 3.1) illustrates the temporal evolution of wind variance from December 1997 to April 2004, which is the longest continuous wind time series available at these stations without any large gaps (small gaps are filled with linear interpolation). The magnitude of diurnal wind variance peaks in summer (June-August), and is weaker during the non-summer (September-May) months. The summer diurnal

peaks in the wind spectrum are mainly associated with sea breeze. The integrated variance in the diurnal band at this station is shown in the lower panel of Fig. 3.1. Here, the diurnal wind variance is more than 6 $m^2 s^{-2}$ in summer and usually on the order of 0.1 $m^2 s^{-2}$ in the non-summer months. The magnitude of the 3-month smoothed diurnal wind energy is remarkably similar during all six summers of the observation period. However, the greatest diurnal wind variance of up to 12 $m^2 s^{-2}$ occurs in July 2003 as a consequence of the hurricane Claudette during that month. This severe hurricane impulsively inputs a significant amount of energy in all frequency bands. This feature reveals an advantage of wavelet analysis compared to the often-used Fourier spectrum, by illustrating the temporal evolution of the spectrum associated with an extremely strong weather event, whereas with a Fourier representation, this event would be averaged into the spectral band estimated over the entire recordlength.

Wind energy in the weather band (periods of 2 days to 8 days) is seen to be low during summer as compared to the non-summer seasons (Fig. 3.1). As will be discussed, the absence of weather-band wind variance in summer is important for the development of strong ocean near-inertial current oscillations.

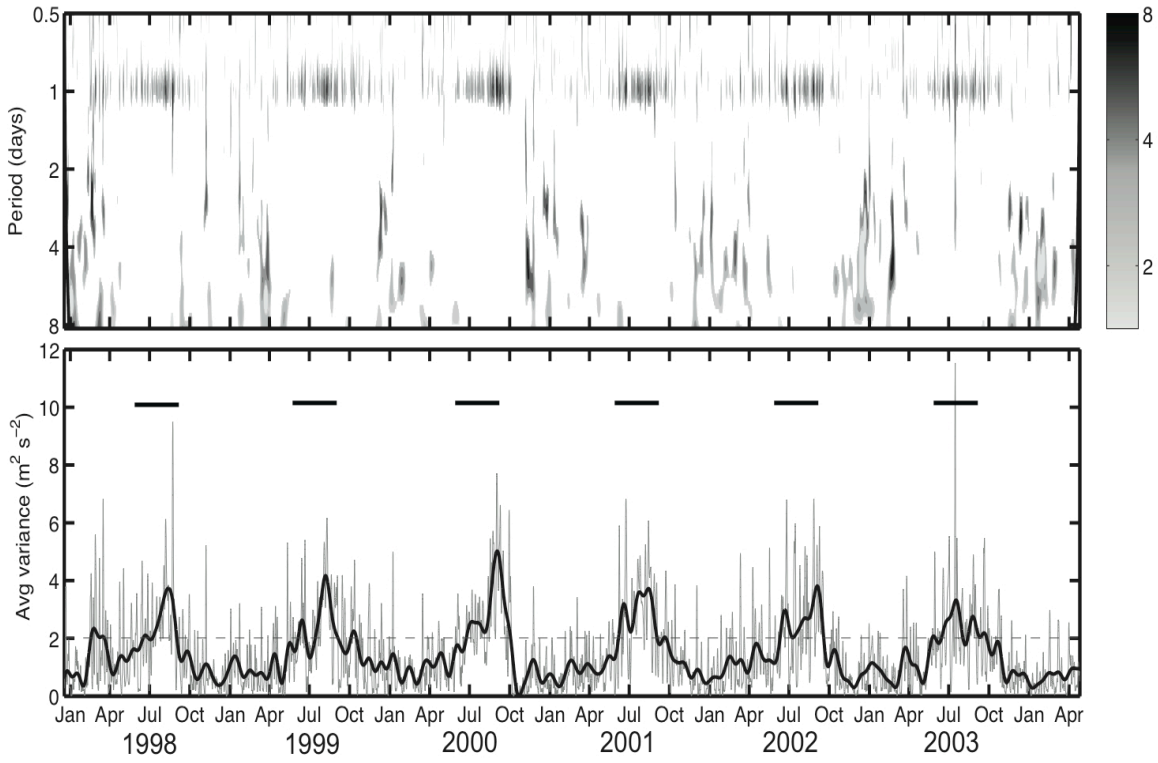

Fig. 3.1. (Upper panel) Wavelet power spectrum (unitless) of the normalized 10-m east-west wind component at NDBC buoy station PTAT2 (97.05°W, 27.83°N). Only significant values are plotted, which are greater than 95% confidence for a red-noise process with a lag-1 coefficient of 0.72 (Torrence and Compo 1998). (Lower panel) The gray solid curve is the frequency(period)-averaged wavelet variance time series (units of $m^2 s^{-2}$) over the 0.83cpd-1.17cpd band during the observation period. The black solid curve is the three-month low-passed values of the gray curve. The horizontal gray dashed line is the 95% confidence level. The black bars indicate summer periods.

3.1.3. Spatial structure of sea breeze

Previously, sea breeze was considered to be confined to coastal areas in the Gulf of Mexico extending less than 50 km offshore from the coast (e.g., Chen et al. 1996). To investigate the spatial distribution of sea breeze in the northwest Gulf of Mexico, wind measurements during the LATEX period are analyzed at locations shown in Fig. 2.3. Fig. 3.2 shows the spatial distribution of the diurnal wind ellipses during the period 4-11 July 1992. This period of measurement is selected based on the following criteria: (1) The diurnal wind was strong; (2) The phase and amplitude of the diurnal wind was nearly constant; (3) There were no atmosphere frontal passages in this month (Nowlin et al. 1998); and (4) The data coverage is good on the shelf during this period. A Butterworth digital band-pass filter is first applied to the wind data at each station to isolate the diurnal wind component from other spectral components. A least-squares harmonic analysis is then used to fit the one-week diurnal wind time series to estimate the phase and amplitude of the east-west and north-south wind components, respectively. The diurnal ellipses in Fig. 3.2 are constructed from the phase and amplitude of the east-west and north-south diurnal wind components. A quantitative summary of these wind ellipses is listed in Table 3.1.

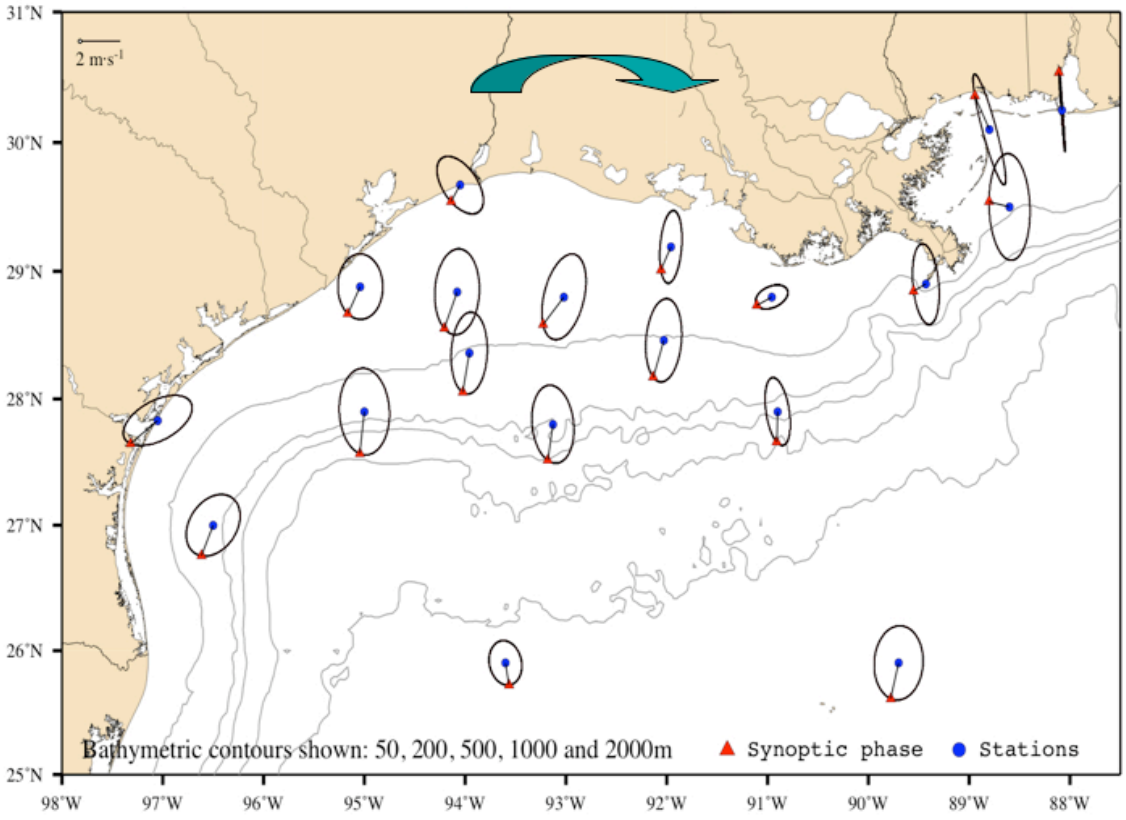

Fig. 3.2. Diurnal wind ellipses during the period 4-11 July 1992, calculated from harmonic analysis of the wind measurement time series taken at the center of each ellipse during the LATEX project (see Fig. 2.3 for basemap). The vectors shown in this figure are displayed in the oceanographic convention (vectors show direction toward which flow is going), and represent a synoptic snapshot of sea breeze at 7 PM local time. The diurnal band used for this plot is from 0.95 cpd to 1.05 cpd. Note: only stations that have data coverage during this period are plotted.

Table 3.1. Statistics of diurnal wind ellipses during the period of 4-11 July 1992. All the angles are compass angles relative to the north.

Station	Longitude	Latitude	Major Axes (m/s)	Minor Axes (m/s)	Orientation (degree)	Phase (degree)
Mooring 17	91.96 °W	29.19 °N	1.42	0.53	186	209
Mooring 19	92.03 °W	28.46 °N	1.64	0.88	187	200
Mooring 22	93.96 °W	28.35 °N	1.61	0.89	184	192
Mooring 50	95.04 °W	28.88 °N	1.28	1.12	178	211
Mooring 51	94.08 °W	28.83 °N	1.68	1.10	185	204
Mooring 52	93.02 °W	28.80 °N	1.75	0.98	200	224
Mooring 53	90.96 °W	28.80 °N	1.42	0.57	206	246
NDBC 42001	89.70 °W	25.90 °N	1.49	1.21	187	195
NDBC 42002	93.60 °W	25.90 °N	0.92	0.78	152	169
NDBC 42007	88.80 °W	30.10 °N	2.26	0.33	161	331
NDBC 42019	95.00 °W	27.90 °N	1.71	1.24	175	188
NDBC 42020	96.50 °W	27.00 °N	1.47	1.06	233	205
CMAN BURL1	89.43 °W	28.90 °N	1.58	0.64	173	246
CMAN BUSL1	90.90 °W	27.90 °N	1.36	0.57	168	182
CMAN DPIA1	88.08 °W	30.25 °N	1.60	0.04	175	354
CMAN GBCL1	93.13 °W	27.80 °N	1.55	1.03	170	190
CMAN MPCL1	88.60 °W	29.50 °N	2.07	1.01	177	281
CMAN PTAT2	97.05 °W	27.83 °N	1.80	0.81	249	236
CMAN SRST2	94.05 °W	29.67 °N	1.40	0.78	134	215

The magnitude of the diurnal wind ellipse (Fig. 3.2) exhibits somewhat complex spatial structure presumably depending on a number of issues such as coastal geometry, Louisiana inland waters, and differential coastal heating. The magnitude of sea breeze increases offshore first and then decreases with distance offshore. The reason why sea breeze is relatively small near the coast might be related to the frictional effect near the coast. Phase information of the diurnal winds is displayed as a solid red triangle on each ellipse; this represents a synoptic snapshot of the diurnal wind vectors at 7 PM local time (Fig. 3.2). The green arrow on land at the top of the figure signifies that the diurnal wind vectors rotate clockwise. This phase distribution indicates that diurnal phase is leading at the near-coast stations and propagates offshore; this is consistent with the coastal origination of sea breeze. Phase distribution along the transect stations SRST2, 51, 22, GBCL1, and 42002 (Fig. 3.2 and Table 3.1) indicates the sea breeze is not restricted to the coastal area, but can extend to more than 300 km offshore in summer beyond the Texas-Louisiana Shelf to the deep ocean. Since all the diurnal wind vectors rotate clockwise, this phase distribution indicates it takes about three hours for the sea breeze signal to propagate from 30°N to 26°N, indicating a phase speed of the diurnal winds around 120 km hr^{-1} during this time period. Fig. 3.2 is shown here to be an example. These phase relationships are examined for several other summer periods and found to be robust. More wind data are used in the full analysis later in section 3.2.

3.2. The ocean current variability

Ocean currents on the continental shelf of the northwest Gulf of Mexico are analyzed in a manner similar to that of winds presented previously in section 3.1. First, wavelet power spectra are constructed for selected mooring locations. The upper panel of Fig. 3.3 shows the wavelet power spectrum of the north-south current time series at the top meter (14 m) of mooring 21. From Fig. 3.3, near-inertial current energy clearly peaks in summer compared to the non-summer seasons. The maximum near-inertial current variance occurs around 10 June during 1992 and 1994, and on 3 July during 1993. The increase of near-inertial current energy is episodic and can last from 2-10 days. The gray curve in the lower panel of Fig. 3.3 exhibits the near-inertial current variance time series at the upper meter of mooring 21 during the LATEX study period. This variance can be as large as 200 $cm^2 s^{-2}$ and is an order of magnitude greater than that in the non-summer seasons. The peaks of the near-inertial current are largest in summer 1994 and smallest in 1993. The reasons for the interannual variability are related to changes in stratification and will be discussed later. The peak of near-inertial current energy in summer is seen at most of the mooring stations on the Texas-Louisiana Shelf, where current measurements are available. Wavelet power spectra for moorings 25 (water depth 50 m) and 8 (water depth 200 m) are shown in Fig. 3.4 and Fig. 3.5 as other examples, from which we can see the near-inertial current energy on this shelf is typically an order of magnitude larger in summer than in the non-summer months.

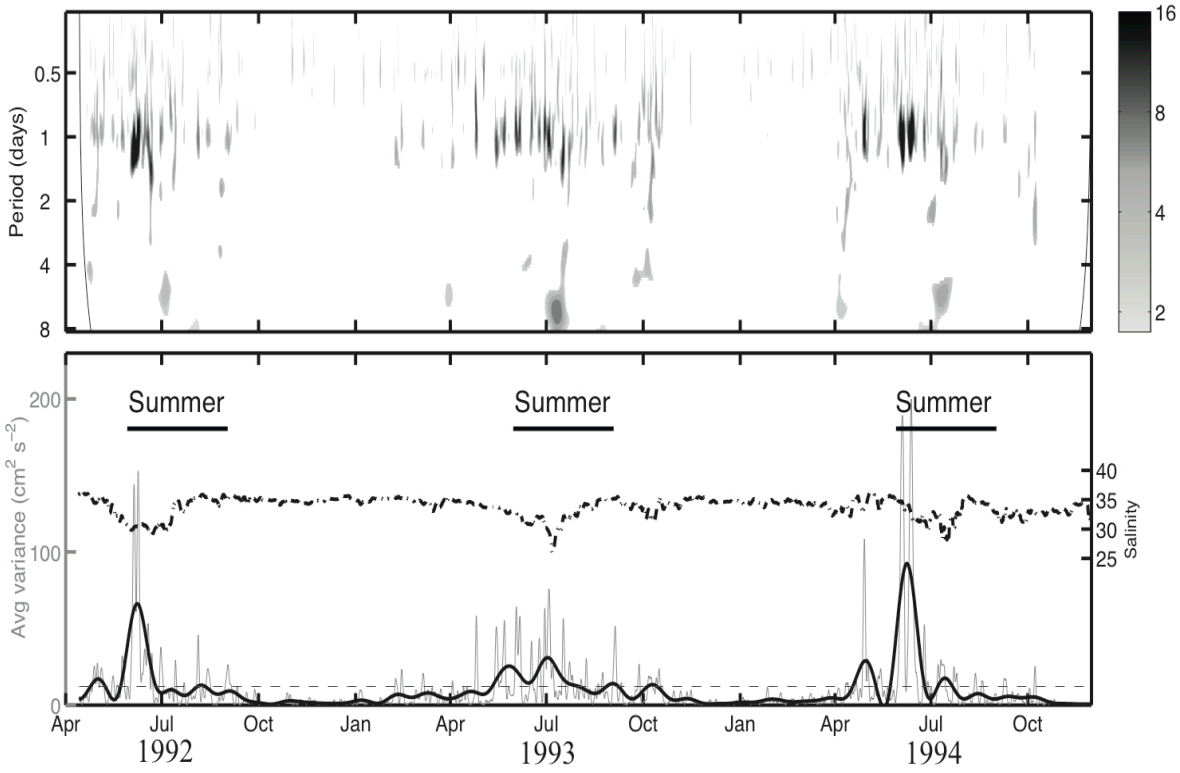

Fig. 3.3. (Upper panel) Wavelet power spectrum (unitless) for the hourly north-south current time series at the upper meter (14 m) of mooring 21. Only significant values are plotted, which are greater than 95% confidence for a red-noise process with a lag-1 coefficient of 0.72 (Torrence and Compo 1998). Those two gray lines on either end indicate the "cone of influence", where edge effects become important. (Lower panel) The gray solid curve is the frequency(period)-averaged wavelet variance time series (units of $cm^2\ s^{-2}$) over the 0.83cpd -1.17cpd band during the observation period. The black curve is the one-month low-passed values of the gray curve. The horizontal gray dashed line is the 95% confidence level. The black dash-dotted curve is the two-day running averaged salinity time series at the upper meter of mooring 21.

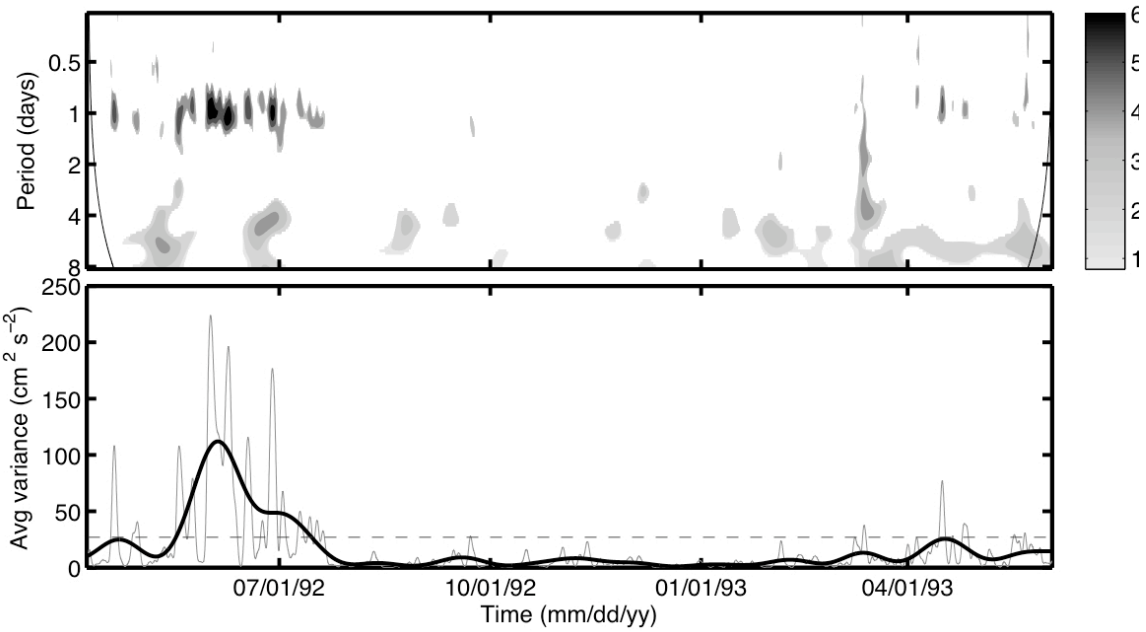

Fig. 3.4. Same as fig. 3.3 but for the top meter (11 m) of mooring 25.

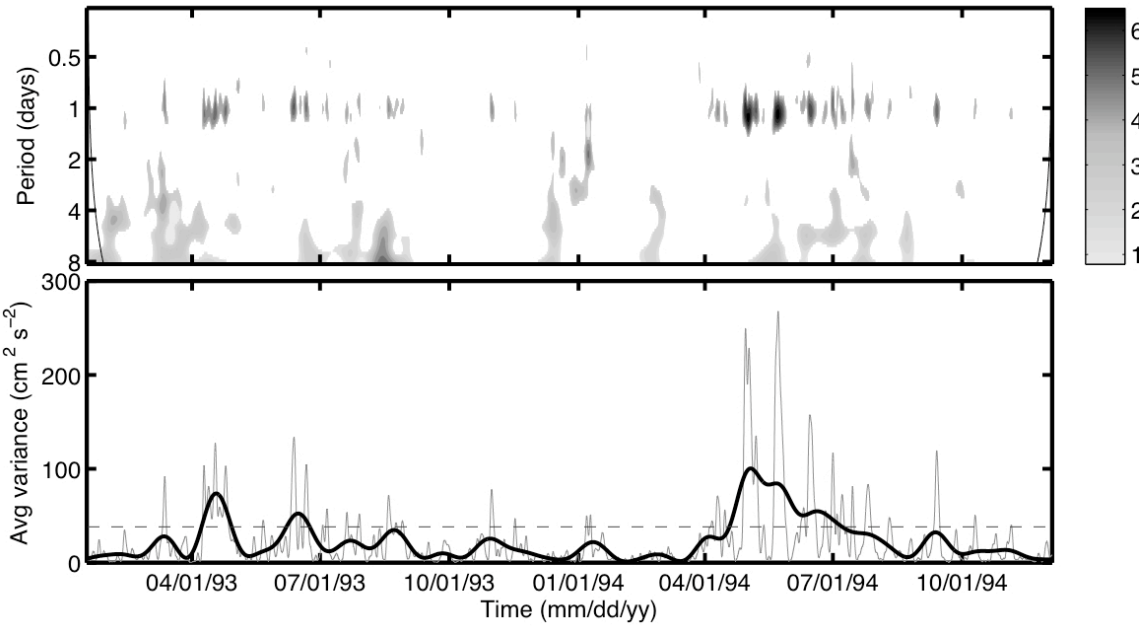

Fig. 3.5. Same as fig. 3.3 but for the top meter (10 m) of mooring 8.

The magnitude of the near-inertial currents is variable among different summer months. Wavelet analysis is done to the one-year time series from December 1993 to November 1994 for the top meter (3m) at mooring 22, when the observations have no gaps. The upper panel of Fig. 3.6 shows the wavelet power spectrum of the north-south current time series from June to August 1994. The near-inertial current variance is much larger at mooring 22 in the summer of 1994 (Fig. 3.6) compared to that at moorings 21, 25, and 8 (Figs. 3.3, 3.4, and 3.5, respectively). This appears to be caused by the fact that the top meter at mooring 22 (3 m) is in the summer mixed layer while the top meters at moorings 8, 21, 25 (10 m, 14 m, and 11 m, respectively) are below it. The maximum

near-inertial current variance at mooring 22 is as large as 1400 cm^2 s^{-2} in June while it only reaches about 700 cm^2 s^{-2} in July or August (black curve in the middle panel of Fig. 3.6). In comparison, the weather band (2-8 days) current variance, plotted in the middle panel of Fig. 3.6 (gray curve), is much lower and less than 50 cm^2 s^{-2} during most of the summer time. This demonstrates that near-inertial current energy dominates on the shelf during the summer time, and when the near-inertial current variance is strongest in June, it contributes more than 90% of the total current energy at this location. The band-passed diurnal wind time series at this station shows that sea breeze actually peaks in August of summer 1994. The larger near-inertial response in June at these mooring locations on the Texas-Louisiana Shelf despite peak sea breeze forcing in August appears to be related to two factors: duration of diurnal wind with uninterrupted phase and strength of stratification. I now examine these effects on the development of the near-inertial current response to sea breeze forcing.

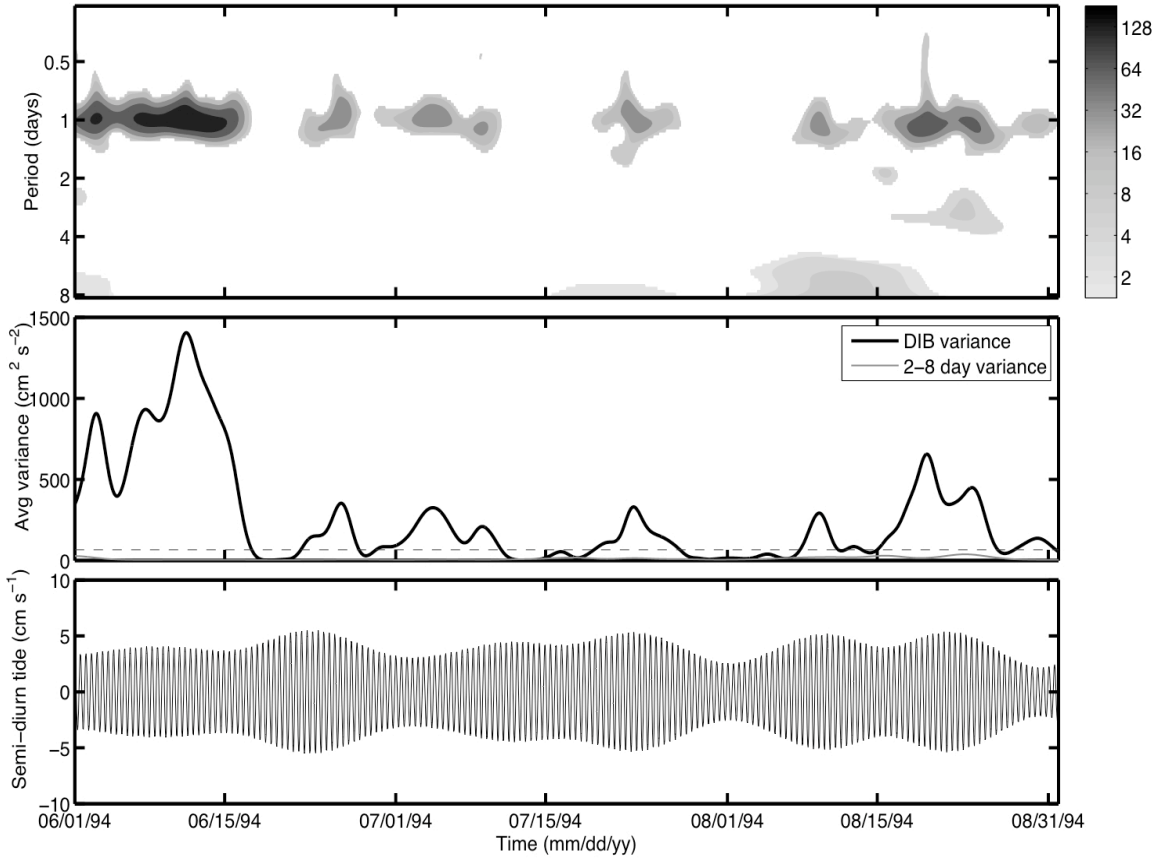

Fig. 3.6. (Upper panel) Wavelet power spectrum (unitless) for the hourly north-south current time series from December 1993 to November 1994 at the upper meter (3m) of mooring 22. Only the wavelet spectrum from June to August 1994 is plotted. Only significant values are plotted, which are greater than 95% confidence for a red-noise process with a lag-1 coefficient of 0.72 (Torrence and Compo 1998). (Middle panel) The black curve is the frequency(period)-averaged wavelet variance time series (units of cm^2 s^{-2}) over the 0.83cpd -1.17cpd band, and the gray curve is the frequency(period)-averaged wavelet variance over the 2cpd-8cpd band in summer 1994. The horizontal gray dashed line is the 95% confidence level. (Lower panel) North-south semi-diurnal tidal current time series in summer 1994, calculated using the T_Tide Harmonic Analysis Toolbox of Pawlowicz et al. (2002).

3.2.1. Effects of near-inertial band phase on near-inertial band response

The wavelet coherency and phase spectra between the north-south wind and current components at mooring 22 (3 m instrument) in January, June and August 1994 are

estimated (Fig. 3.7a,b,c, respectively). The red color in Fig. 3.7 means the coherency is high, while the blue means it is low. The arrows in Fig. 3.7 indicate the phase difference between the wind and current at each time with in-phase pointing right, anti-phase pointing left, and wind leading current by 90° pointing straight down. For clarity, only one vector is plotted per day at each period. We can see from Fig. 3.7b that the wind and current show significant coherency (γ^2>0.9) in the near-inertial band for most of June 1994. Low coherency occurs around 16 June 1994, when a cold front passes through the northwestern part of the Gulf of Mexico. In the near-inertial band, the wind and current are almost in phase during June except for the interruption period of the front. During the frontal passage, the sea breeze wind and near-inertial current become approximately 90 degrees out of phase with the wind leading the currents and the coherency is low and insignificant. The sea breeze wind and near-inertial current are almost in phase with very high coherency for about 10 days during the period of 5-14 June 1994. This corresponds to the period when the near-inertial current variance reaches 1400 cm^2 s^{-2} (Fig. 3.6) and is also the highest of the measurement period. This suggests that the duration of the in-phase relationship between the wind and currents is important for the generation and accumulation of the near-inertial current energy. In the weather band, we can see that both the variance and coherency are very low during this period (Fig. 3.6; Fig. 3.7b), indicating few events in the weather band. From this result, I conclude that the infrequency of summer frontal passages, particularly in June, contributes to the in-phase relationship between the sea breeze wind and near-inertial current, and allows it to

persist for up to 10 days without phase interruption. Because infrequent summer-frontal passages are typical for this region (DiMego et al. 1976; Nowlin et al. 1998), we can expect these conditions to occur each summer. Because of the near-resonant condition at this latitude, the diurnal wind is very efficient in generating large near-inertial current energy. It can generate near-inertial ocean energy in several cycles and the longer this in-phase relationship persists, the larger the magnitude of the near-inertial current becomes (maximum sea breeze driven near-inertial current observed is ~ 70 cm s^{-1}). The coherency is also very high, with an almost in-phase relationship in the near-inertial band, during the periods of 21-24 June and 28-30 June, with a three-day interruption from 25-27 June. The increased wind variance at this station around 25 June (not shown), as well as high coherency in the weather band (Fig. 6b) indicates the occurrence of weather band processes. With this interference, the near-inertial current variance is only about 250 cm^2 s^{-2} (Fig. 3.6).

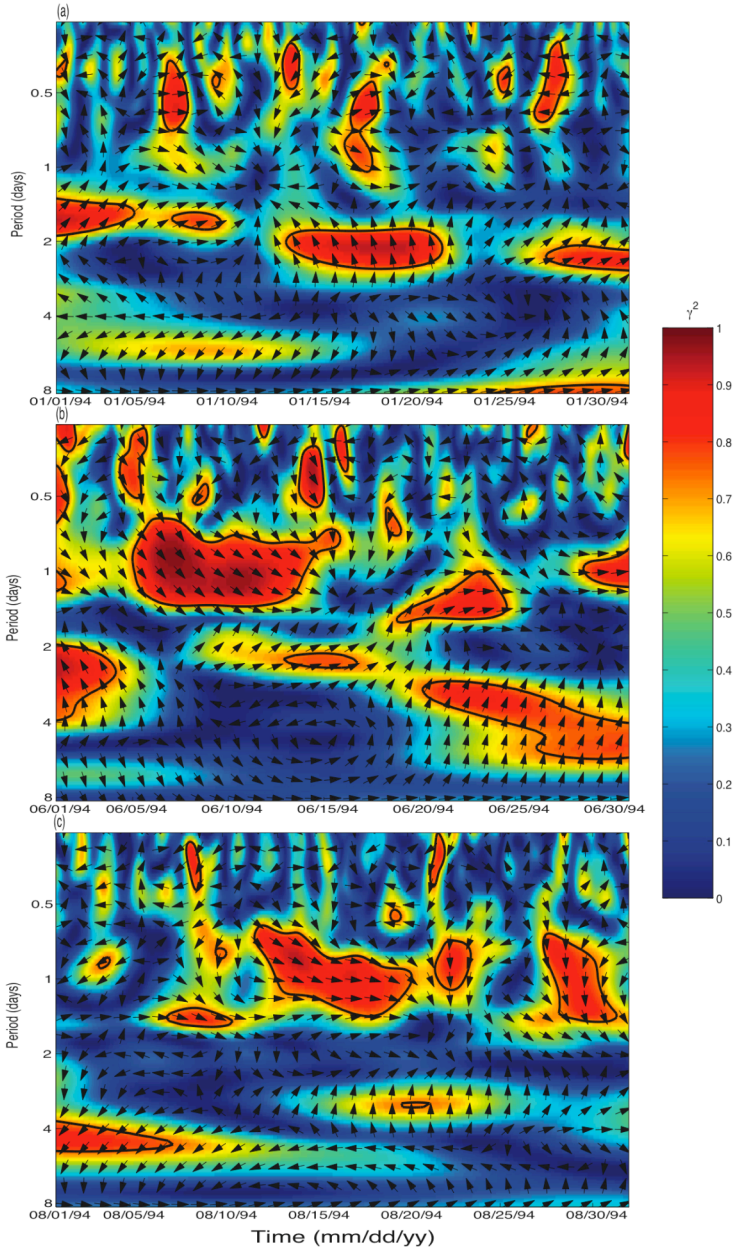

Fig. 3.7. (a) Squared wavelet coherency and phase spectra between north-south wind component and north-south current component at mooring 22 in January 1994. The thick contour encloses regions of greater than 95% confidence from a Monte Carlo simulation of wavelet coherency between 300 sets (two each) of red noise time series. The vectors indicate the phase difference between the wind and current at different frequency (with in-phase pointing right, anti-phase pointing left, and wind leading current by 90° pointing straight down). Only one vector is plotted each day in time. Thirty vectors are plotted in frequency/period domain. (b) Same as (a) but for June 1994. (c) Same as (a) but for August 1994.

Fig. 3.7c shows the wavelet coherency and phase spectra for August 1994. The coherency between the wind and current is low compared to that found in June (Fig. 3.7b), with 95% significant coherency between 0.7 and 0.9 during 14-20, 22, and 28-29 August and very low coherency, less than 0.4, during the rest of the month. In August, the phase between the sea breeze wind and near-inertial current changes more frequently than in June. However, during the high coherency period of 14-20 August, the sea breeze wind and near-inertial current are almost in phase, when the near-inertial current variance increases to 700 $cm^2 s^{-2}$ (Fig. 3.6). After that, the phase between the wind and current gradually changes from in phase to 90 degrees out of phase with leading wind on 22 August; the corresponding near-inertial current energy drops to 400 $cm^2 s^{-2}$. On 23 August, a relatively strong atmospheric front approaches the mooring location, which can also be seen from the high current variance between 2-day and 4-day period in Fig. 3.6, and the near-inertial current energy drops down precipitously to less than 50 $cm^2 s^{-2}$ on 26 August, which is below the 95% significant level. The near-inertial current variance increases again to about 150 $cm^2 s^{-2}$ after the front (Fig. 3.6), which corresponds to the high coherency patch between 28-29 August in Fig. 3.7c.

In comparison with the summer situation, the wavelet coherency and phase spectra for January 1994 at mooring 22 are an example that shows the phase relationship between wind and currents during the non-summer months (September – May; Fig. 3.7a). The diurnal wind variance in this month is typically less than 1.0 $m^2 s^{-2}$, indicating that strong sea breeze does not usually occur in non-summer months. The sea breeze wind and near-inertial current coherency is low, below 0.4 and not significant

during most of January. In comparison with summer, the distribution of the near-inertial band phase between wind and current is highly variable, mainly due to the passage of seven cold fronts (Nowlin et al. 1998). There is high coherency in the weather band in January. From Fig. 3.1, the weather band wind energy is strong in January on the Texas-Louisiana Shelf. This high coherency between the wind and current suggests that the weather band processes dominate in this month of the year and is consistent with previous observational and numerical studies of circulation of this shelf, which support the dominance of wind driving of the inner shelf flow (DiMarco et al. 2000; Nowlin et al. 2005; Cho et al. 1998; Chen et al. 1996; Oey 1995).

3.2.2. Effects of stratification on near-inertial band response

The near-inertial current energy at mooring 22 in June 1994 is approximately double that of August. This is likely because the sea breeze winds are continuous in June with fewer interruptions compared to August. This is also manifested in the coherency, which is also higher in June.

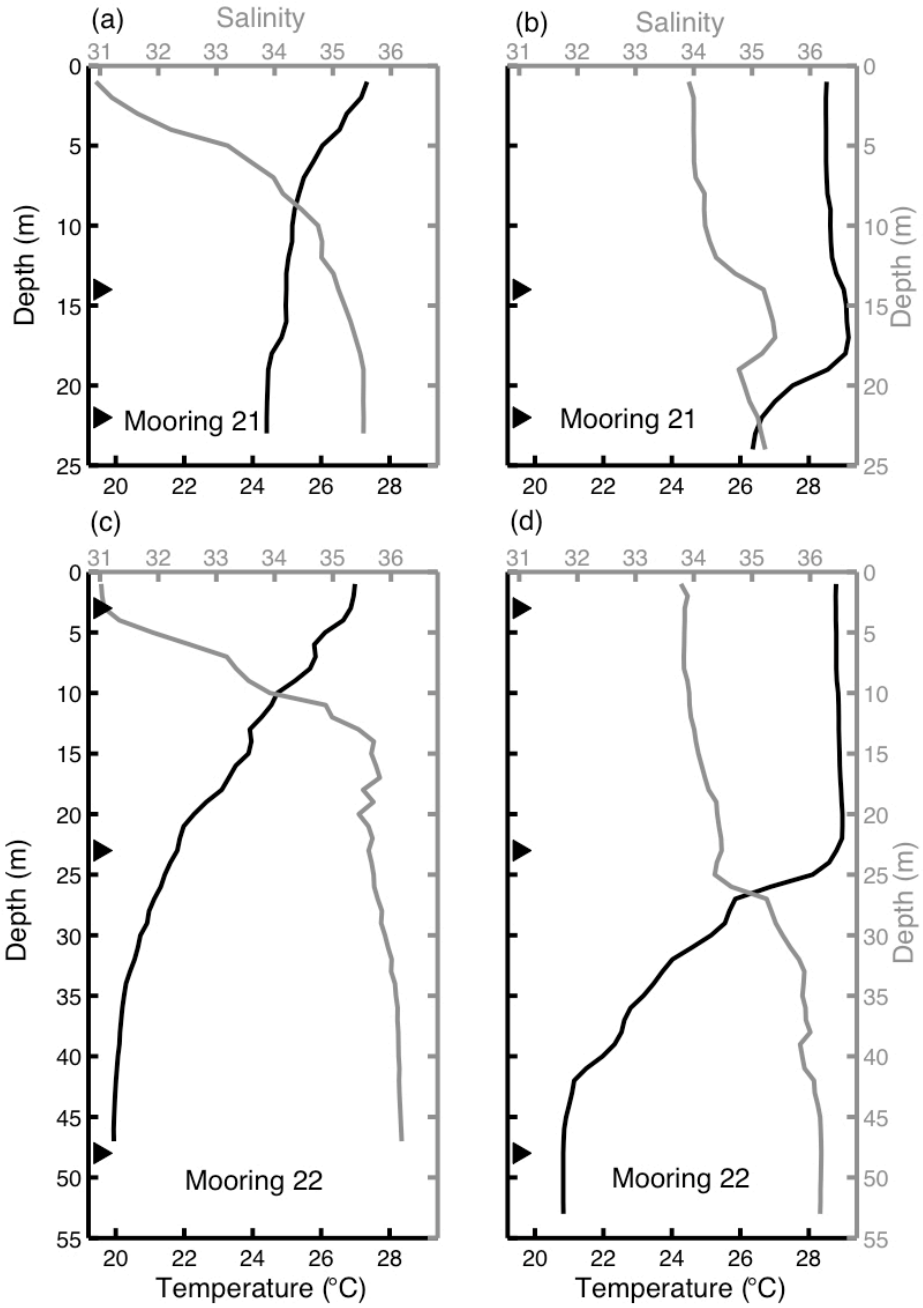

Fig. 3.8. (a) Profiles of temperature and salinity at mooring 21. The measurements were made on 28 May 1994. (b) Same as (a) but the measurements were made on 1 August 1994. (c) Profiles of temperature and salinity at mooring 22. The measurements were made on 29 May 1994. (d) Same as (c) but the measurements were made on 1 August 1994. Triangles in each panel represent the current-meter locations on moorings 21 and 22, respectively.

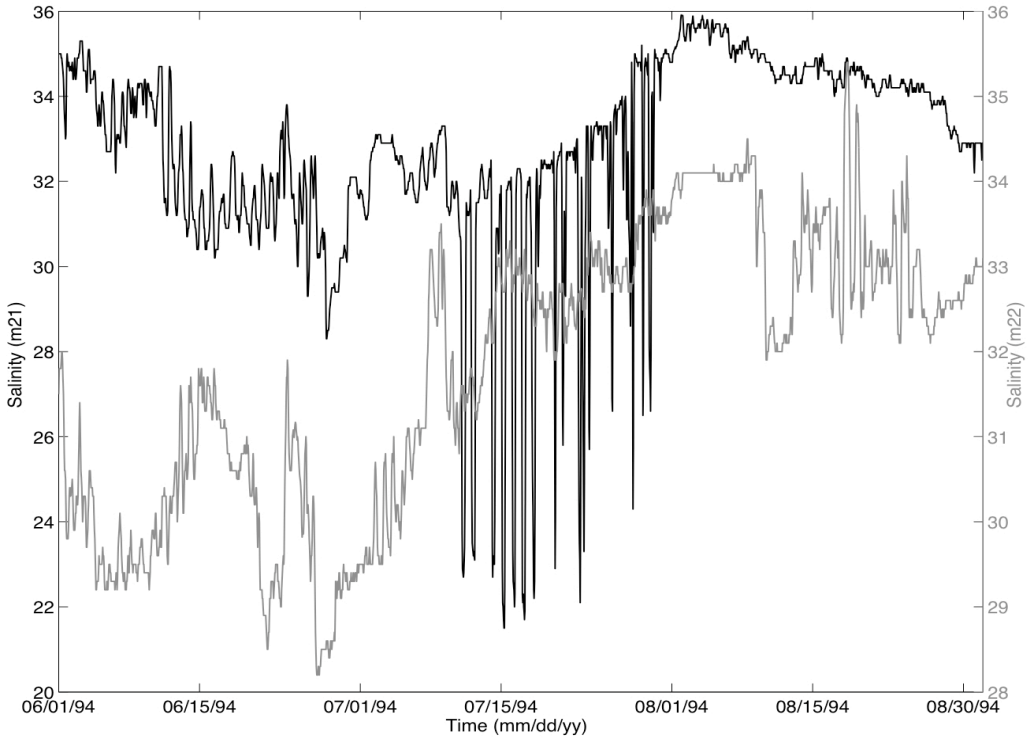

Fig. 3.9. Salinity time series at moorings 21 and 22 from June to August 1994. Black curve is the top-meter (14 m) salinity time series at mooring 21 and gray curve is the top-meter (3 m) salinity time series at mooring 22. Note: scale is changed for clarity.

Additionally, stratification plays an important role in controlling the oceanic response to sea breeze. Fig. 3.8 shows a comparison of temperature and salinity profiles at moorings 21 and 22 for 28-29 May and 1 August 1994. Because no CTD profiles are available for early June, I assume that the temperature and salinity profiles for 28-29 are representative of the stratification in early June. This assumption is not unreasonable based on examination of the moored time-series records. Fig. 3.8 shows that the mixed layer depth in late May 1994 is about 3 meters at both mooring stations. In contrast, on 1 August, the mixed layer extends to ~15 meters at mooring 21 and ~25 meters at mooring

22. Considering a first baroclinic mode ocean response, diurnal wind forcing of a thicker upper layer can result in a weaker depth averaged near-inertial ocean response in August.

To further illustrate the importance of stratification, the correlation between the salinity and the near-inertial current variance time series at the top meter of mooring 21 is calculated. The near-inertial current variance peaks are quite coincident with the salinity minimum period in summer (Fig. 3.3). The correlation coefficient between the salinity time series and the near-inertial current variance time series is 0.25 and is significant at the 99% significance level. This also indicates the important influence of stratification, which is partially determined by the river run off (Belabbassi 2006), in determining near-inertial ocean response to sea breeze forcing. The gray curve in Fig. 3.9 shows the top-meter salinity time series at mooring 22 in summer months 1994. The salinity changes from around 30 in June to around 33 in July and August 1994. This suggests the change of mixed layer depth from June to August, consistent with the CTD profiles.

From the wavelet power spectrum of 30-month current measurements for the top meter at mooring 21 (Fig. 3.3), the interannual variability of the near-inertial current energy is apparent. Peak near-inertial current variances during 1992 and 1994 are of similar magnitude and both occur in mid-June of each year. However, in 1993, the maximum value of the near-inertial current variance is about one half to one third of that in 1992 and 1994. Further, it occurs in early July 1993, or about one month from the

peak time in 1992 and 1994. These differences are mainly caused by two factors: difference in stratification and the occurrence of synoptic wind variations in June 1993.

During 1993 an anomalously large discharge of the Mississippi River occurred when the Mississippi River basin in the Midwestern United States experienced unusually high rainfall (Nowlin et al. 1998; Walker et al. 1994). The river discharge in April and May 1993 was on average 31,000-32,000 $m^3 s^{-1}$, compared to typical spring values of 20,000 $m^3 s^{-1}$. It is estimated that there is about a 1-month lag between discharge observations at Tarbert Landing, MS, and arrival of river waters at mid-shelf locations (Wiseman et al. 1997). Therefore, the freshwater discharge reaches the moorings 21 and 22 locations around June. CTD profiles collected on 23 May 1993 indicate that the mixed layer depth is about 15 m (not shown), much deeper than the 3-m mixed layer observed at about the same time in 1994 (Fig. 3.8). Further, the vertical salinity gradient is significantly reduced as compared with 1992 and 1994. This deeper mixed layer at the mooring locations in June 1993 is probably caused by the combined effects of the large volume of fresh water discharge and the associated vertical mixing along the ~500 km path from the mouth of the Mississippi River to the middle Texas-Louisiana Shelf. However, the details of mixing between the freshwater and the fluid below along this long pathway are beyond the scope of this research. The second factor is the occurrence of weather band wind processes around 1 June and 13 June 1994. As a consequence, the coherency is relatively low between the wind and current in June 1993 compared to that in 1992 and 1994, and the phase between the sea breeze wind and near-inertial current is variable (not shown). Together these two reasons explain the relatively low near-inertial

current energy in June 1993 and the forward shift in time of peak variance compared with 1992 and 1994.

It is interesting to note that weather band (2-8 days) current variance at 14-m depth (mooring 21) also peaks in summer (Fig. 3.3), although the weather-band wind variance on the Texas-Louisiana Shelf is more energetic in non-summer months (Fig. 3.1) (DiMarco et al. 2000; Nowlin et al. 2005). However, this is likely associated with the very different summer versus winter shelf stratification. The observations are taken at 14 m, which is below the nominal mixed layer in summer and within the deeper nominal mixed layer during winter.

3.2.3. Vertical structure of the sea-breeze driven near-inertial current and its effects on the vertical mixing on the Texas-Louisiana Shelf

In this section, the vertical structure of the near-inertial current and its effects on the vertical mixing will be discussed. First, the wavelet power spectrum is estimated for the current velocity time series collected at the bottom meter (22 m) of mooring 21, the middle meter (23 m) and the bottom meter (48 m) of mooring 22. The near-inertial current variances at the bottom meter of mooring 21, the middle and bottom meters of mooring 22 also peak in summer. However, the magnitudes in the lower layer are weaker than those found at the top meters. The maximum near-inertial current variance at the bottom meter of mooring 21 is about 150 $cm^2\ s^{-2}$ and less than 50 $cm^2\ s^{-2}$ most of the time. Fig. 3.10 shows the wavelet near-inertial current variance time series at the

depth of the top, middle and bottom meters of mooring 22, respectively. The maximum near-inertial current variance at the middle meter of mooring 22 is only 200 cm^2 s^{-2} and one seventh of that at the upper meter depth. The maximum near-inertial current variance at the bottom meter of mooring 22 is only about 50 cm^2 s^{-2}. The near-inertial current variance is weak at the middle and bottom meters in the non-summer months at mooring 22 (Fig. 3.10).

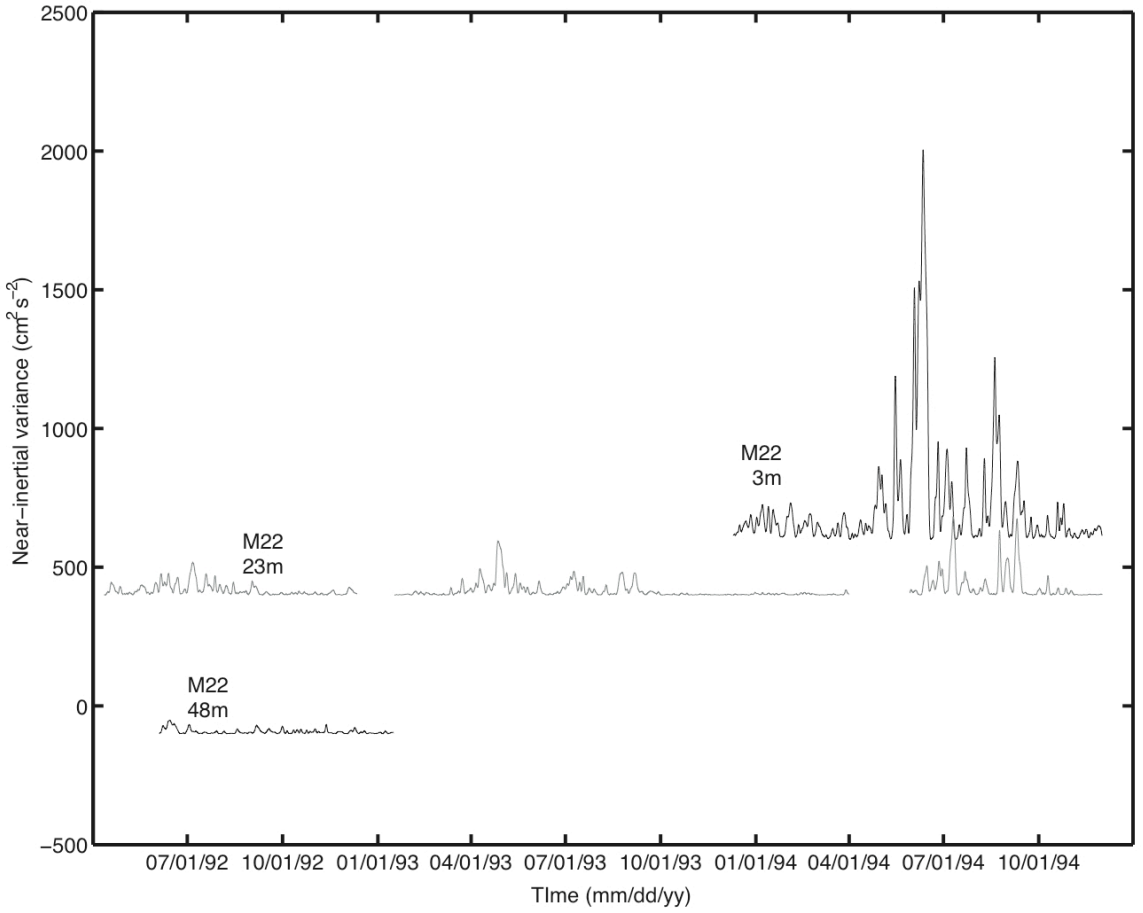

Fig. 3.10. Frequency(period)-averaged wavelet variance time series (units of cm^2 s^{-2}) for the north-south current component over the 0.83cpd -1.17cpd band at the top, middle, and bottom meters of mooring 22.

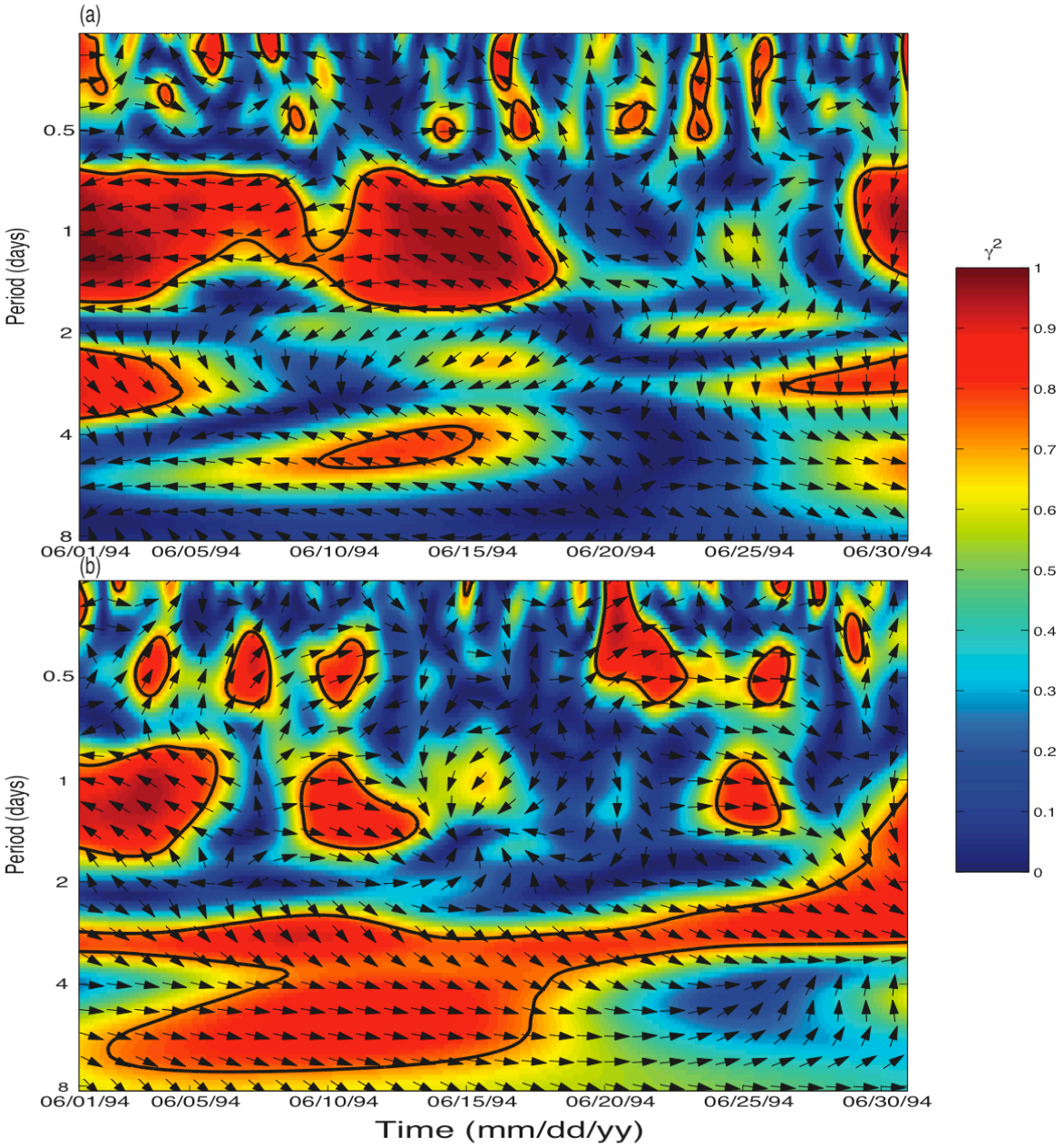

Fig. 3.11. (a) Squared wavelet coherency and phase between north-south current components of mooring 22 at 3 m (top meter) and at 23 m (middle meter) in June 1994. (b) Squared wavelet coherency and phase between north-south current components of mooring 21 at 14 m (top meter) and at 22 m (bottom meter) in June 1994.

The wavelet coherency and phase spectra between the top- and middle-meter currents in June 1994 at mooring 22 (Fig. 3.11a) show strong near-inertial current period during 1-16 June. The near-inertial currents at 3 m and 23 m are very well correlated, with coherency greater than 0.9 and 180-degree phase. Based on the temperature and salinity profiles (Fig. 3.8), the pycnocline at mooring 22 in early June 1994 is between 5 m and 15 m. Therefore, the top and middle current meters at mooring 22 are above and below the pycnocline, respectively. This reversal of near-inertial current direction at depth indicates a first baroclinic mode response, which is consistent with the previous study on the Texas-Louisiana Shelf (Chen et al. 1996) and the Namibian shelf (Simpson et al. 2002).

Fig. 3.11b shows the wavelet coherency and phase spectra between the top- (14 m) and bottom- (22 m) meter currents at mooring 21 in June 1994. The coherency is high during three time periods: 1-5 June, 9-12 June, and 23-26 June, respectively. Near-inertial current variance is also large during these three periods (Fig. 3.3). Near-inertial currents for the top meter and bottom meter are out of phase (180° phase) during the first high-coherency period and in phase (zero phase) during the other two periods. A shoaling of the mixed layer may have occurred on 6 June 1994, which is indicated by the sudden decrease of the salinity from 35 to 33 at 14-m depth on June 6 (black curve in Fig. 3.9). This changes the location of the top current meter (14 m) from within the mixed layer to below the mixed layer. The top meter and bottom meter at mooring 21 change from being on different sides of the pycnocline during 1-5 June to the same side of the pycnocline during 9-12 June. As a consequence, the phase difference between the

near-inertial currents for the top and bottom meters changes from out-of-phase to in-phase. This result also indicates that the first baroclinic mode structure existed for the near-inertial current at mooring 21 during these strong near-inertial current events in June 1994.

Previous research on this topic has indicated first baroclinic mode structure associated with sea breeze driven near-inertial currents (Chen et al. 1996; Simpson et al. 2002; Rippeth et al. 2002). However, observations of vertically sheared currents are not in themselves evidence of mixing. To study the effects of sea breeze driven near-inertial currents on vertical mixing, we need to know the relative importance of stratification versus shear, which can be characterized by the Richardson number. In this dissertation, the temperature, conductivity (salinity) and current measurements at the top (3 m) and middle (23 m) meters of mooring 22 are used to estimate the bulk Richardson number time series during June 1994, when sea breeze driven near-inertial currents are strongest at this location (Fig. 3.6). Previously, the bulk Richardson number has been used to study the stability of the upper ocean due to diurnal heating, cooling, and wind forcing (Price et al. 1986) and the vertical mixing rates in the thermocline (Gregg 1989). The bulk Richardson number calculated here from these two meters can suggest the stability of the water column between 3 m and 23 m. Mathematically, it can be calculated by,

$$Ri_b = \frac{N^2}{S^2}, \tag{3.1}$$

where N is the Brunt-Väisälä frequency, and S is the vertical current shear. The Brunt-Väisälä frequency N is defined as

$$N^2 = -\frac{g}{\rho_0}\frac{d\rho}{dz} \approx -\frac{g}{\rho_0}\frac{\Delta\rho}{\Delta z}, \tag{3.2}$$

where ρ is the potential density calculated from the temperature and conductivity measurements at the top and middle meters, respectively, g is the gravity constant, ρ_0 is the averaged potential density, and Δz is the distance between the two meters (20 m for this case). The vertical squared shear is defined as

$$S^2 = (\frac{du}{dz})^2 + (\frac{d\upsilon}{dz})^2 \approx (\frac{\Delta u}{\Delta z})^2 + (\frac{\Delta \upsilon}{\Delta z})^2, \tag{3.3}$$

where Δu and $\Delta \upsilon$ are the east-west and north-south current differences between the top and middle meters, respectively.

Fig. 3.12 shows the Brunt-Väisälä frequency, squared shear, and bulk Richardson number time series in June 1994 at mooring 22. Comparing Fig. 3.6 and Fig. 3.12, I find that when sea-breeze driven near-inertial currents are strongest (~ 12 June 1994), the velocity shear in the water column is significantly increased, stratification is decreased and the bulk Richardson number is smallest with the values on the order of 1. After the front passes by mooring 22 on 16 June 1994, the near-inertial motions are suppressed during the following week (Fig. 3.6). The corresponding bulk Richardson number becomes much larger (~ 30 most of the time and even larger sometimes) because of the increase of the stratification and significant decrease of velocity shear. During another strong near-inertial current event (21-24 June 1994, Fig. 3.6), the bulk Richardson number is also suppressed. The bulk Richardson number time series shown in Fig. 3.12 supports the idea that strong near-inertial response to sea breeze forcing in summer could significantly enhance vertical mixing in the water column on the Texas-Louisiana Shelf.

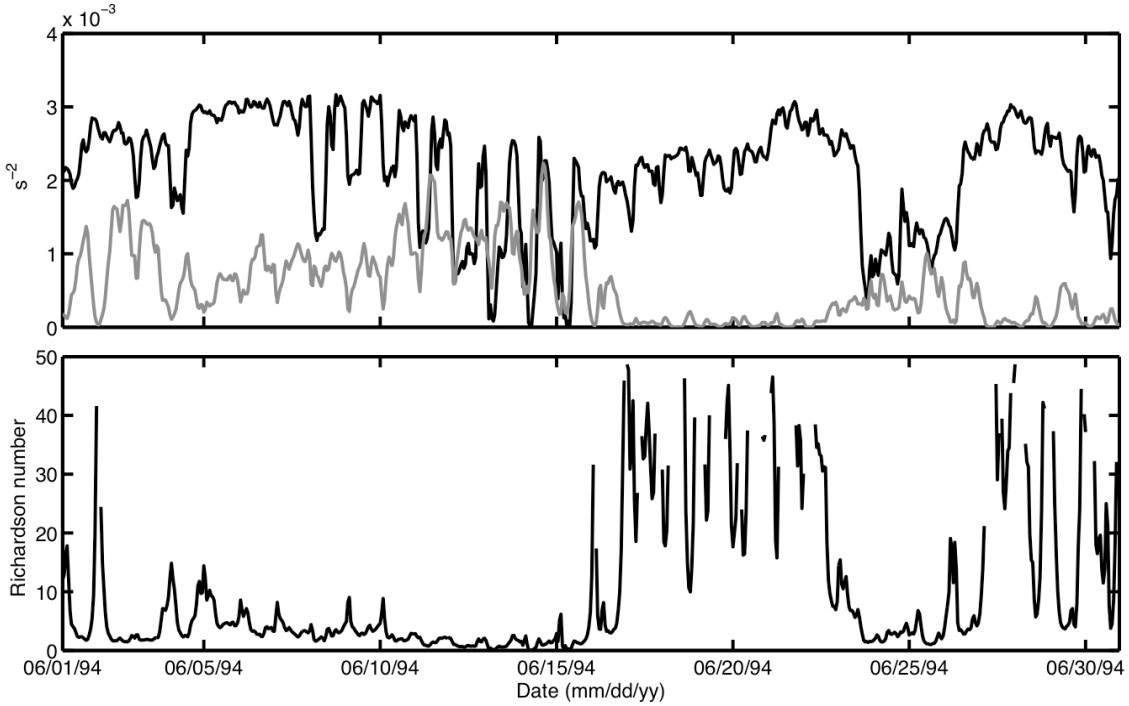

Fig. 3.12. (Upper panel) The black and gray curves are the Brunt-Väisälä frequency and squared shear time series calculated from the temperature, conductivity and current measurements at mooring 22, respectively. (Lower panel) Bulk Richardson number time series calculated from the Brunt-Väisälä frequency and squared shear time series (Ri_b). For clarity, bulk Richardson number is plotted only when it is less than 50.

The eastern Texas-Louisiana Shelf experiences seasonal near-bottom hypoxia (dissolved oxygen concentration less than 1.4 ml l^{-1}) (Rabalais et al. 2007), which is believed to be caused by the combined effects of high nutrient loading that leads to eutrophication of the coastal waters (Turner and Rabalais 1994) and increased water column stability in summer (Wiseman et al. 1997; Hetland and DiMarco 2008). A mechanism to increase vertical mixing and therefore increase ventilation of oxygen poor bottom waters would contribute to the control of the extent, duration, and severity of the

Texas-Louisiana Shelf hypoxic region, the details of which are beyond the scope of this study.

3.2.4. Spatial structure of sea breeze driven ocean response

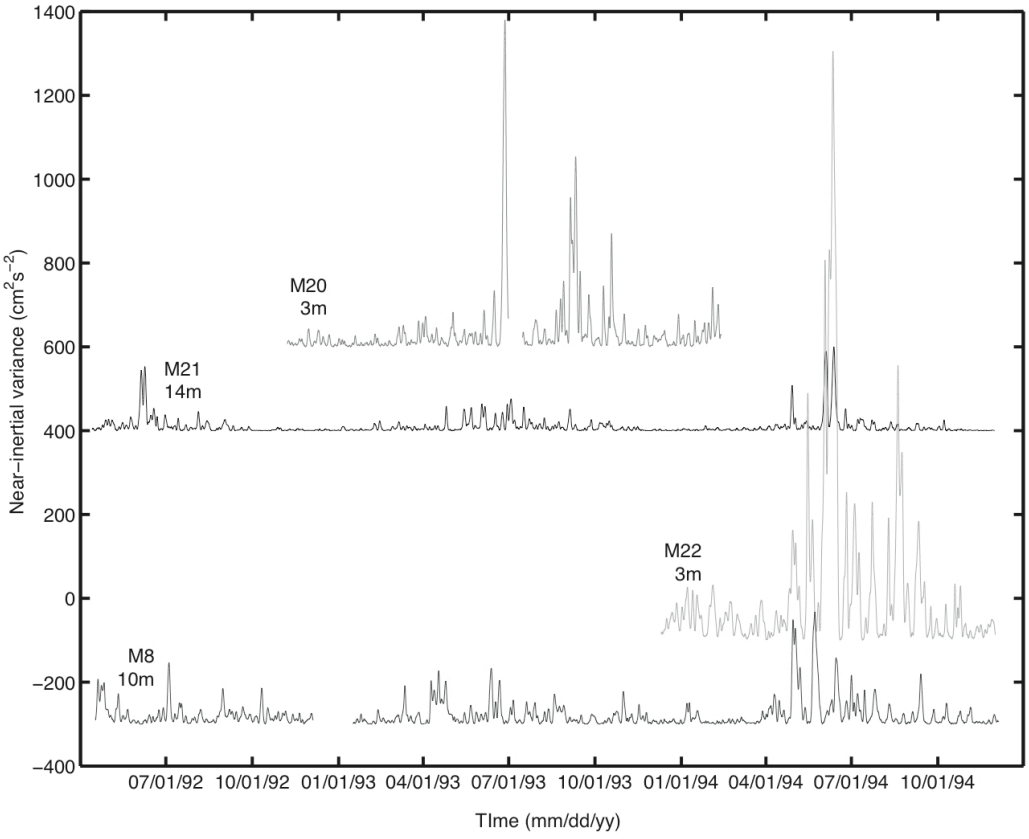

Fig. 3.13. Frequency(period)-averaged wavelet variance time series (units of $cm^2\ s^{-2}$) for the north-south current component over the 0.83cpd -1.17cpd band at the top meters of cross-shelf mooring stations 20, 21, 22, and 8. The water depths at these four stations are 14 m, 24 m, 55 m, and 200 m, respectively.

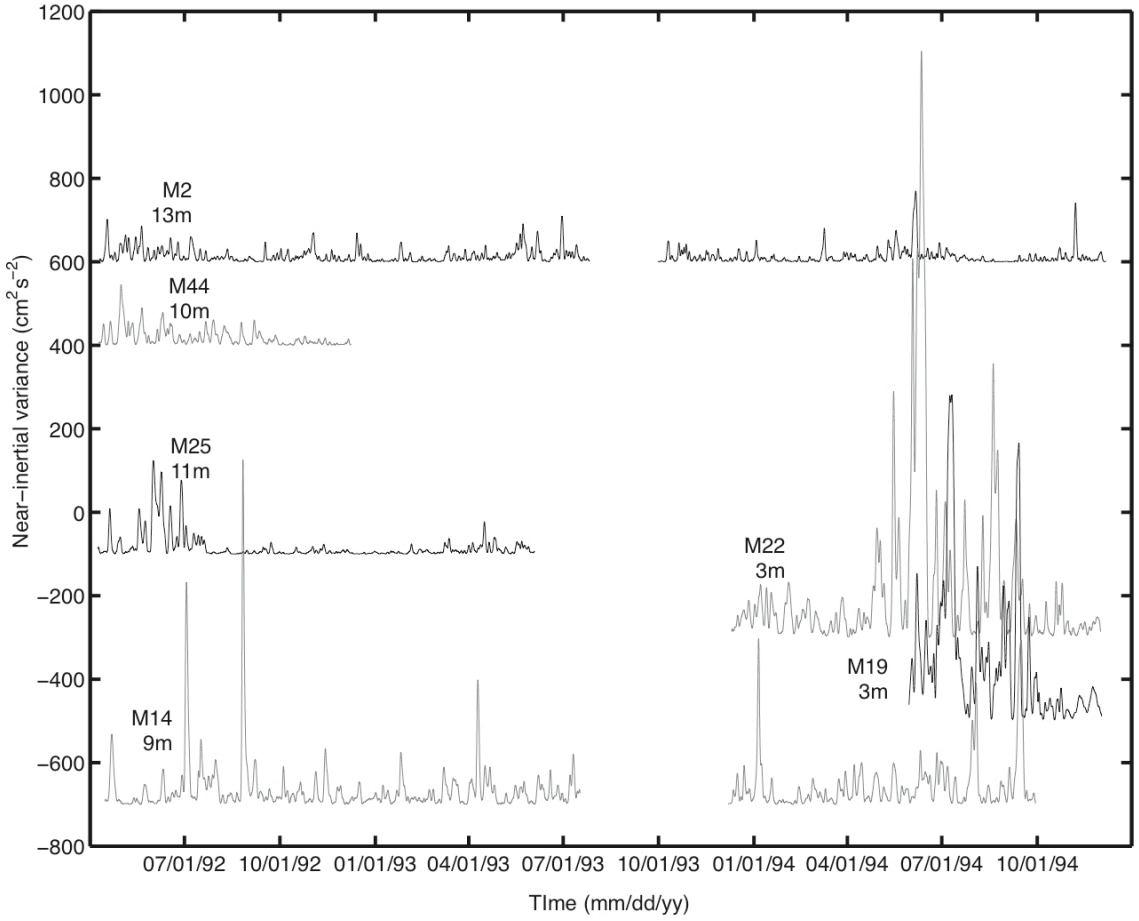

Fig. 3.14. Frequency(period)-averaged wavelet variance time series (units of cm^2 s^{-2}) for the north-south current component over the 0.83cpd -1.17cpd band at the top meters of mooring stations 2, 44, 25, 22, 19, and 14 along the 50 m isobath.

In this section, the spatial structure of the near-inertial oceanic response to sea breeze on the Texas-Louisiana Shelf will be discussed. Two different transects are chosen here to illustrate the along- and across- shelf spatial structure, respectively. The cross-shelf transect includes mooring stations 20, 21, 22, and 8 ranging from water depth 14 m to 200 m. The along-shelf transect includes mooring stations 2, 44, 25, 22, 19 and 14 (along 50-m isobath) starting from the southwest boundary of the Texas-Louisiana

Shelf to the mouth of the Mississippi River. Current data at these stations are first detided and then wavelet analysis is applied afterward.

The summer intensification of the near-inertial oceanic response to sea breeze can be seen at all the stations along these two transects on the Texas-Louisiana Shelf. Fig. 3.13 shows the spatial structure of the near-inertial wavelet current variance time series at the top meter of the mooring locations in the cross-shelf direction. The summer near-inertial current variance can be at least an order of magnitude larger than that in the non-summer months at these stations. Summer intensification of near-inertial currents can extend to the shelf break (mooring 8), consistently with the horizontal extent of sea breeze (Fig. 3.2). The magnitude of near-inertial current variance is on the order of 1000 $cm^2\ s^{-2}$ at the top meters of moorings 20 and 22. However, it is an order of magnitude weaker at the top meters of moorings 21 and 8. The difference in the magnitude of the near-inertial oceanic response may be related to the strength of sea breeze forcing at different locations and the depth of the top current meter that may be above or below the pycnocline depending on the stratification.

Fig. 3.14 shows the spatial structure of the near-inertial wavelet current variance time series at the top meter of the mooring locations along the 50-m isobath. The magnitude of near-inertial ocean response is maximum at moorings 22, 19, and 14, due to the same reasons discussed above for the across-shelf structure. However, in the northeast part of the shelf (mooring 14), the near-inertial oceanic response shows more seasonality, probably because it is closest to the mouth of the river and more influenced by the river discharge.

3.3. A correction to the tides on the middle Texas-Louisiana Shelf

In order to evaluate the energy in the sea breeze driven near-inertial band, the LATEX data had to be detided. In the process of doing this, it was determined that more tidal constituents than previously considered had to be removed. DiMarco and Reid (1998) studied the characteristics of the tidal constituents using the 30-month *in situ* current measurements on the Texas-Louisiana Shelf from the LATEX project. In their analysis, eight principal tidal constituents (O1, K1, P1, Q1, S2, M2, K2, and N2) were examined using the iterated least-squares method of cyclic descent (Bloomfield 1976). In this research, I used the T_Tide Harmonic Analysis Toolbox of Pawlowicz et al. (2002) to extract the principal tidal energy. This method includes more tidal constituents depending on the length of the current records (usually 50 to 68 constituents are considered when the time series is longer than a year). Some higher order shallow water tides were found to be strong over the middle Texas-Louisiana Shelf. They can contribute a significant portion of the tidal energy. The shallow water tides are strong when (1) the water depth is shallow (water depth less than 50 m); and (2) the principal lunar and solar semidiurnal and diurnal tides are strong. These tides include M3, MN4, M4, MS4, S4, and M8. For example, the shallow water tidal constituents can contribute up to 30% of the total semi-diurnal tidal variance at mooring 21 (water depth 24 m) on the middle shelf (Fig. 3.15). The magnitude and phase information of the tidal constituents at mooring 21 was displayed in Table 3.2. This phenomenon of enhanced shallow water tides is not seen on the outer shelf region (water depth greater than 50 m)

or at those stations where the principal semidiurnal and diurnal tides are weak (e.g., mooring 20, water depth 14 m).

Table 3.2. Characteristics of tides at mooring 21 (only tidal constituents that are significant at 95% confidence level are listed).

Semi-diurnal				
Species	Symbol	Period (hr)	Amplitude (cm s^{-1})	Phase (degree)
Larger lunar elliptic semidiurnal	N2	12.66	1.32	168
Principal lunar semidiurnal	M2	12.42	5.62	187
Principal solar semidiurnal	S2	12	1.71	182
Diurnal				
Species	Symbol	Period (hr)	Amplitude (cm s^{-1})	Phase (degree)
Lunar diurnal	K1	23.93	3.43	313
Solar diurnal	S1	24	0.97	321
Lunar diurnal	O1	25.82	3.63	307
Larger lunar elliptic diurnal	Q1	26.87	0.93	289
Higher harmonics				
Species	Symbol	Period (hr)	Amplitude (cm s^{-1})	Phase (degree)
Variational	MU2	12.87	0.33	113
Lunar terdiurnal	M3	8.28	0.12	110
Shallow water quarter diurnal	MN4	6.27	0.09	129
Shallow water overtides of principal lunar	M4	6.21	0.20	166
Shallow water quarter diurnal	MS4	6.10	0.10	180
Shallow water overtides of principal solar	S4	6	0.09	322
Shallow water eighth diurnal	M8	3.11	0.01	141

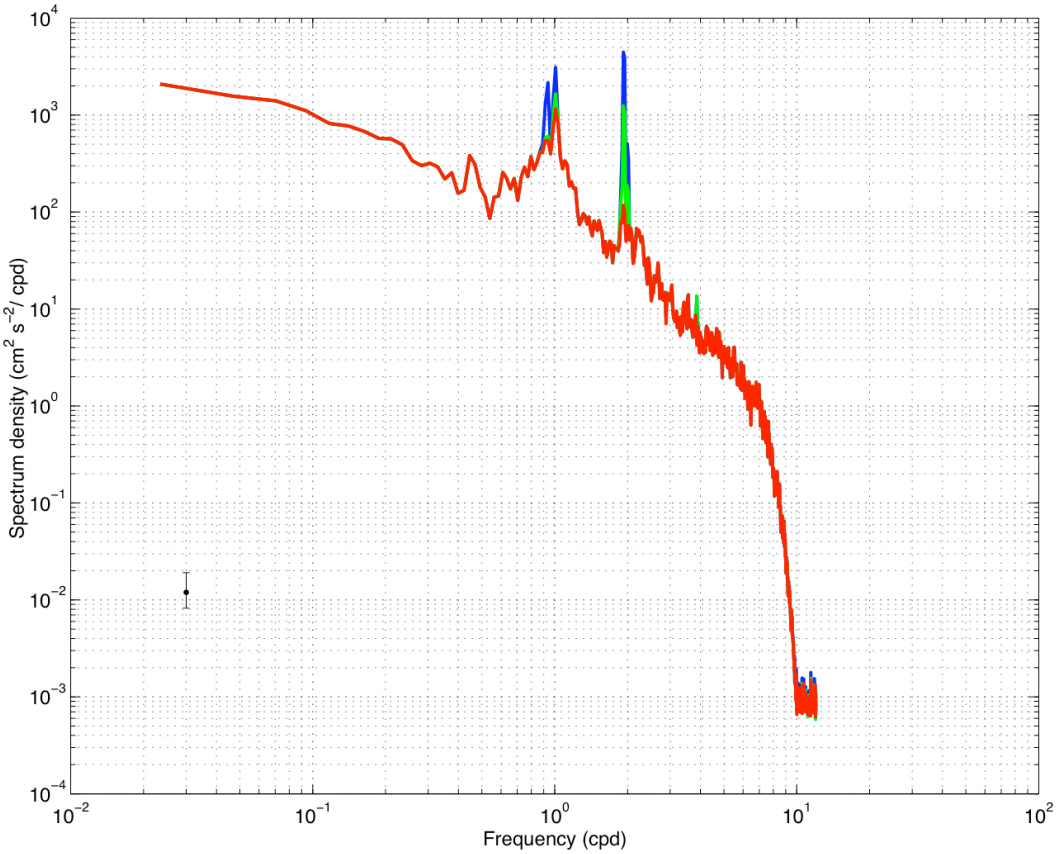

Fig. 3.15. Spectra of the raw north-south current component (blue), the detided north-south current component (green; only eight principal tidal constituents are removed), and the detided north-south current component (red; eight principal tides and all the shallow water tides are removed) at LATEX mooring 21.

CHAPTER IV

NUMERICAL MODEL SIMULATIONS

Although the observational analysis is confined mostly to the continental shelf, the wind observation strongly indicates that the diurnal signal extends to the deep Gulf of Mexico and to the southern shelves. This will likely have implication for mixing of upper oceanic layers through deepening of the mixed layer depth and exchange between the continental shelf and open ocean. Modeling analysis in this chapter will show that the oceanic response to sea breeze forcing can be manifest as propagating *Poincare* waves, south of 30° latitude, thus establishing a basin-wide response. Therefore, the shelf response reported in Chapter III is but a small part of a much larger response. *Poincare* waves have the characteristic that the group speed decreases with latitude, making them more efficient at transferring energy offshore in the southern portion of a basin with geometry like the Gulf of Mexico. Therefore, it is important to understand the dynamics of these propagating *Poincare* waves (e.g., wavelengh, phase and group speed, energetics, and lateral energy flux etc.), and their influence on the redistribution of sea breeze driven oceanic energy and mixing in the upper ocean. However, the available observations are unable to resolve these issues. This chapter will emphasize these aspects based on numerical simulations.

4.1. One- and two- dimensional calculations

4.1.1. One-dimensional calculation

Initially, one-dimensional simulations are performed to investigate the ocean response to sea breeze forcing at different latitudes in the northern hemisphere. Four 20-day simulations are run, in which the *Coriolis* frequency corresponds to four different latitudes (20°N, 25°N, 30°N, and 40°N), otherwise the runs are identical. The temporal evolution of temperature and current profiles at different latitudes are shown in Figs. 4.1 and 4.2 respectively, from which we can see that the stratification of the upper water column is weakest and the ocean response is strongest at 30°N. The ocean response to sea breeze displays similar patterns at latitudes 20°N, 25°N, and 40°N. The mixed layer gradually deepens with time, with no further deepening after about 5 days at 20°N, 25°N, and 40°N (Fig. 4.1). Since the magnitude of the wind is relatively weak (4 m s^{-1}; strong sea breeze but weak in comparison to synoptic winds), little influence of the wind is seen below 15 m. However at 30°N, this sea breeze can deepen the 24°C isotherm from around 15 m downward to 23 m. This indicates that the wind at 30°N is more efficient in mixing the heat downward than at other latitudes. As for the currents, the magnitude of the currents approaches 70 cm s^{-1} at 30°N, while it is approximately 15 cm s^{-1} at other latitudes (Fig. 4.2). The ocean response decreases as the latitude decreases from the critical latitude. This is because sea breeze is resonant with the inertial period of the ocean at 30°N. Therefore, the wind driving has an in-phase relationship with the inertial current and continuously inputs energy into the ocean. Fig. 4.3 shows the distribution of the squared *Brunt-Väisälä* frequency (N^2), squared shear (S^2), gradient

Richardson number (*Ri*), and vertical mixing coefficients at 30°N, all of which indicate the deepening of the mixed layer with time. The depth of maximum stratification coincides with the depth of maximum shear. *Ri* is smallest (<0.25) above the thermocline, which is consistent with the high mixing coefficients in the upper mixed layer.

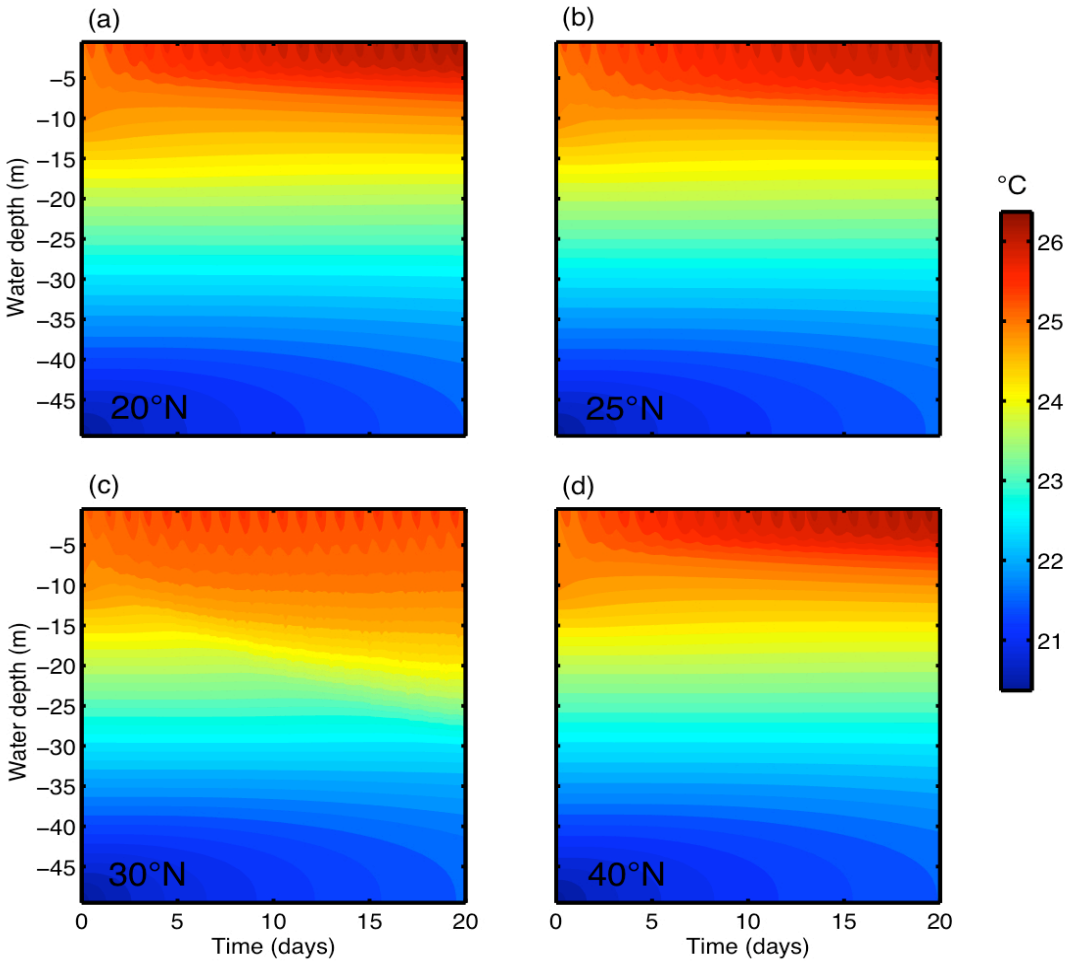

Fig. 4.1. Temporal evolution of temperature fields from 1-D ROMS simulation. (a) 20°N (b) 25°N (c) 30°N (d) 40°N.

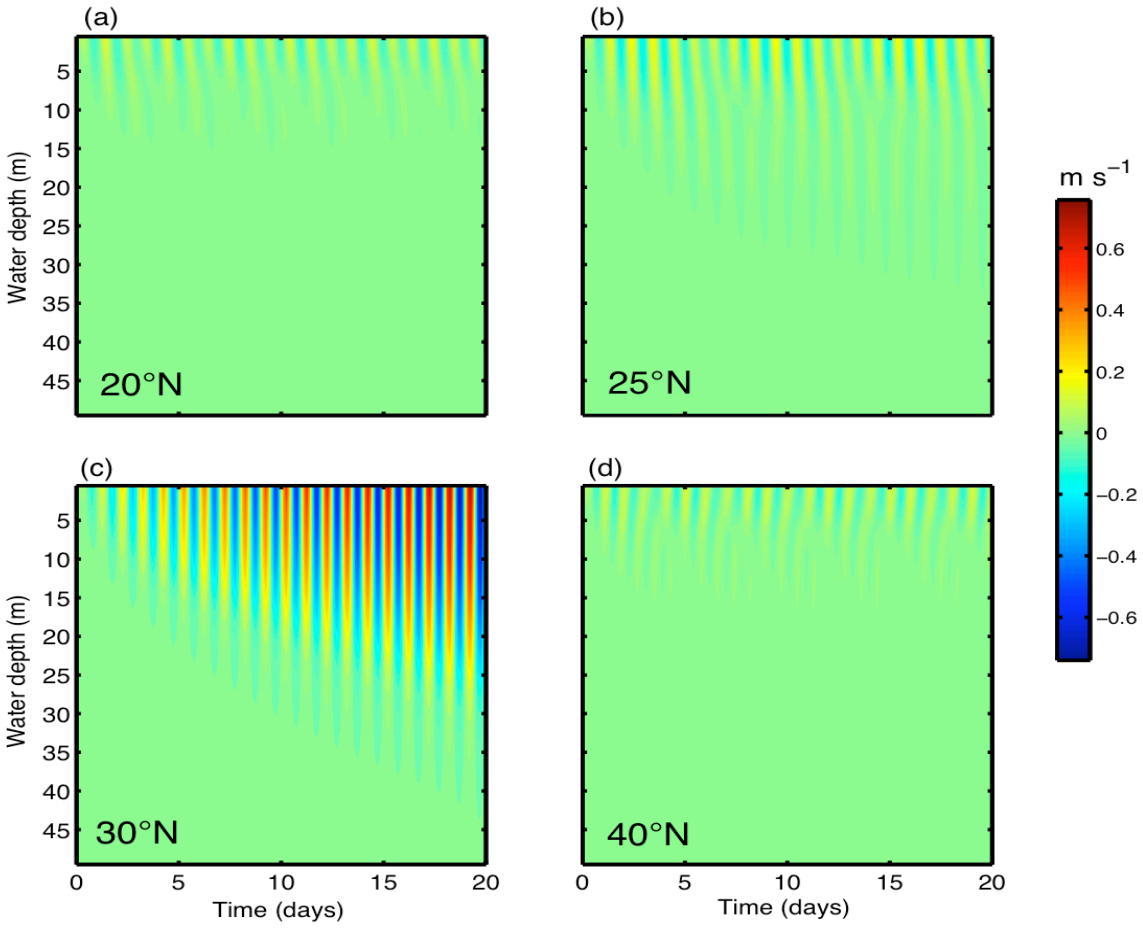

Fig. 4.2. Temporal evolution of east-west current component from 1-D ROMS simulation. (a) 20°N (b) 25°N (c) 30°N (d) 40°N.

Because the one-dimensional experiment does not include the lateral pressure gradient, the occurrence of first baroclinic mode wave structure is not seen, and hence, no horizontal propagation of *Poincare* waves. As a consequence, the mixed layer deepens continuously with time at 30°N, and the ocean does not reach a steady state for this experiment (Figs. 4.1c and 4.2c). The mixed layer can unrealistically reach the ocean bottom (~50 m) if the duration of forcing is allowed to persist for a long period of

time. As will be discussed, these aspects are significant limitations of the one-dimensional model.

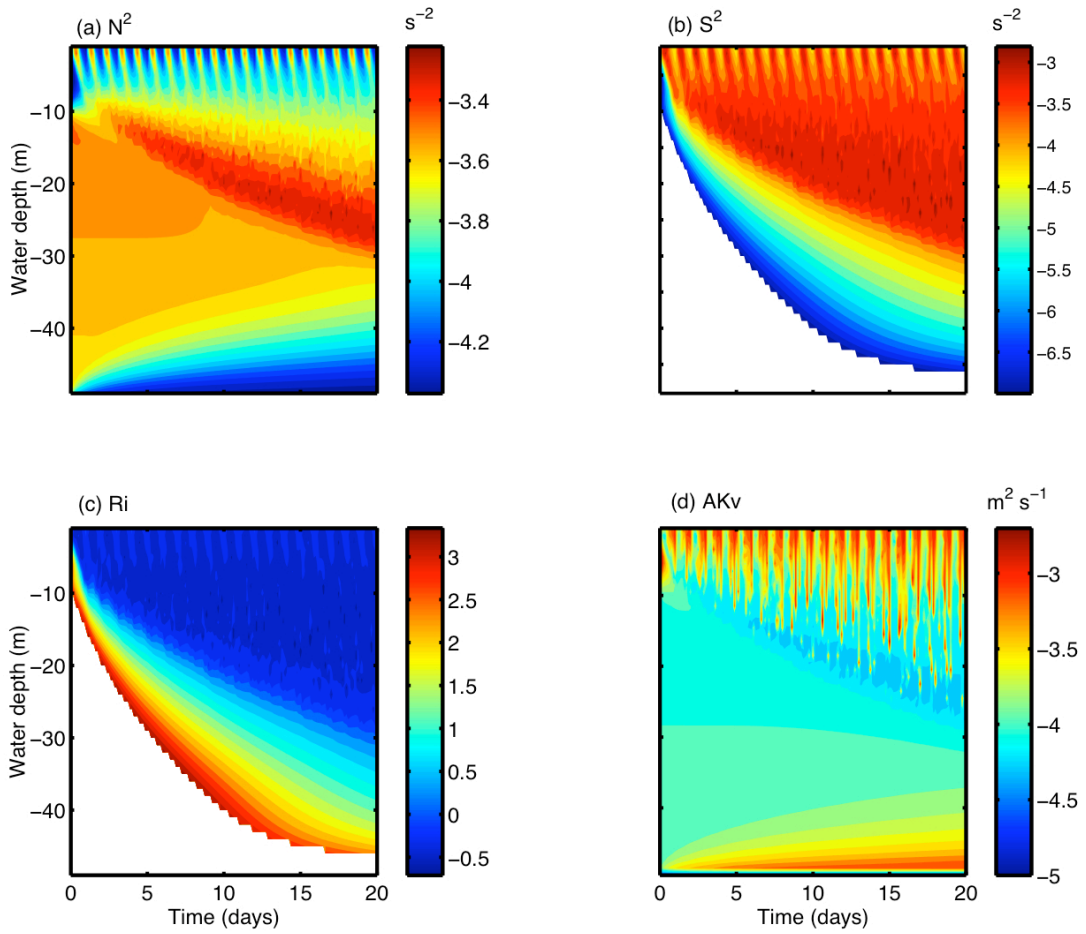

Fig. 4.3. Distribution of (a) Squared Brunt-Väisälä frequency (b) Squared velocity shear (c) *Ri* (d) Vertical mixing coefficients for the 1D ROMS simulation at 30°N.

4.1.2. Two-dimensional calculation

In order to determine the influence of the ocean coastal boundary, a two-dimensional cross-section case with flat bottom is performed for different latitudes. The

northern boundary of the cross-section is set to be a no-slip wall and the southern boundary is radiation open boundary. The case corresponding to 30°N is shown in Fig. 4.4. The forcings are identical to those used in the one-dimensional simulation. The two-dimensional case has 128 points in the y-direction, with a grid interval of 1 km. Twenty day time series of the temperature, current, the *Brunt-Väisälä*, squared shear, *Ri*, and the vertical mixing coefficients at the center of the section are plotted in Fig. 4.4.

The most apparent change, when a boundary exists is the vertical structure of the current profiles. It shows a first baroclinic modal structure instead of just a surface trapped jet (Figs. 4.1 and 4.2). Since there is no wave propagation carrying out energy in the one-dimensional model, all the wind energy is accumulated locally. As a consequence, the magnitude of near-inertial currents in the upper layer increases with time constantly, and a steady state is not reached at the critical latitude during the first 20 days (Figs. 4.1 and 4.2). However, in the two-dimensional simulation, the locally input wind energy can propagate away in the form of waves. In Fig. 4.4, the deepening of the mixed layer can be seen during the first 10 days. A steady state is then established. The mixed layer depth is not changing anymore, when the wind energy input is balanced by the total energy propagating away by waves and dissipated locally by friction. The propagation of sea-breeze driven near-inertial motions (ocean adjustment problem) is addressed in more detail later in the three-dimensional simulations.

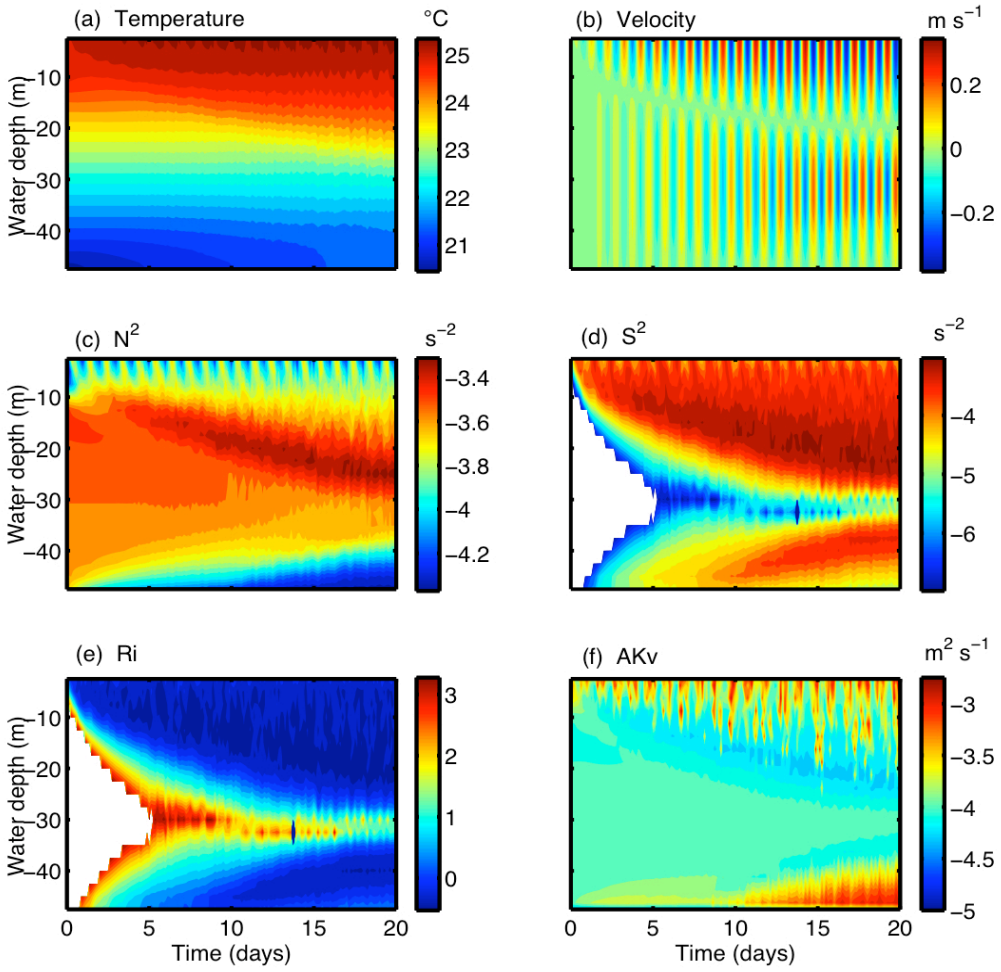

Fig. 4.4. Distribution of (a) temperature (b) east-west current (c) Squared Brunt-Väisälä frequency (d) Squared velocity shear (e) *Ri* (f) Vertical mixing coefficients for the 2D ROMS simulation at 30°N.

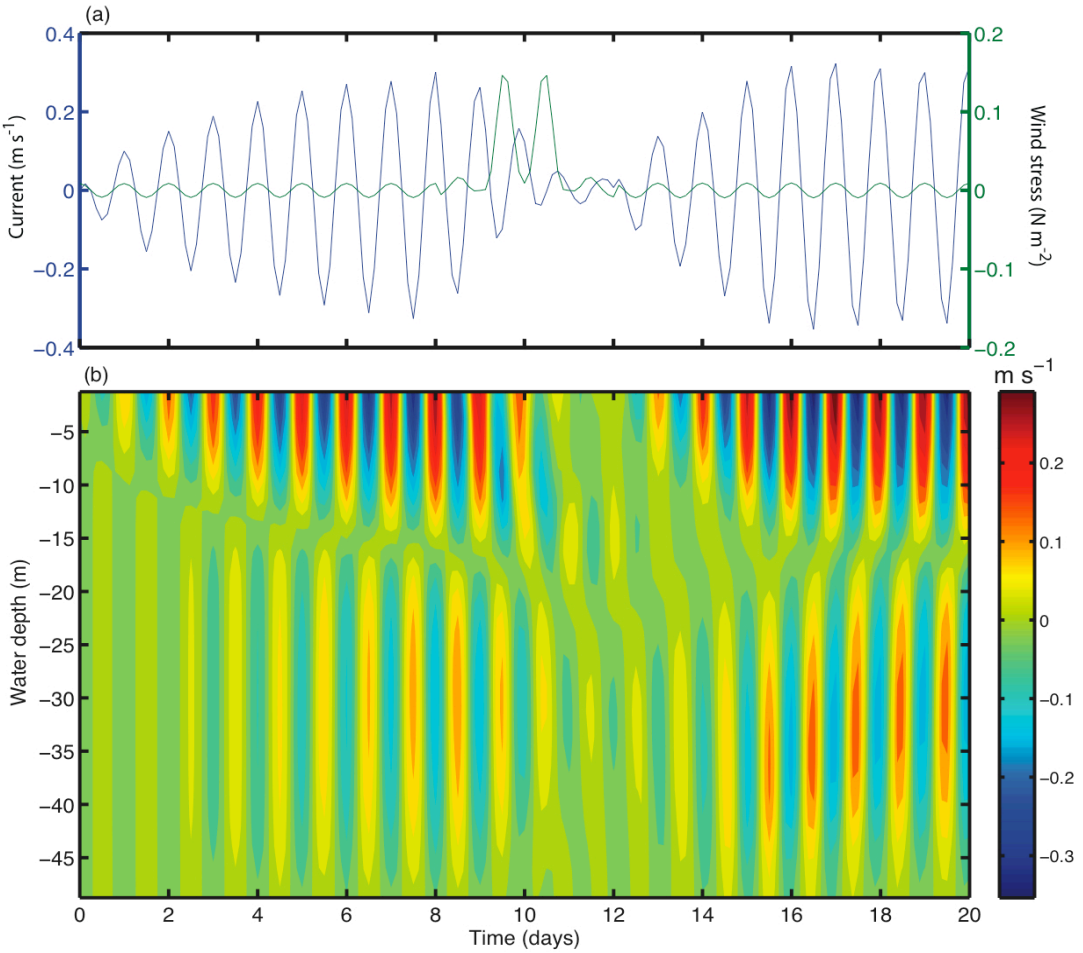

Fig. 4.5. Channel case to testify the effect of synoptic winds on sea-breeze driven near-inertial motions. (a) Temporal series of sea surface wind stress and surface current. (b) Temporal evolution of east-west current profiles.

Previous observations have indicated that synoptic winds (wind impulse) can significantly reduce the sea-breeze driven near-inertial energy by breaking down the in-phase relationship between the sea breeze and inertial currents in the Gulf of Mexico near the critical latitude (section 3.2.1). In order to test this issue, another two-dimensional experiment is conducted. A synoptic wind event is added to the previous two-dimensional case between days 8-12. The synoptic wind event is represented by a

Gaussian bump, which reaches its maximum magnitude of 8 m s^{-1} at day 10. The temporal variation of east-west wind stress and surface current component at the center of the domain is shown in Fig. 4.5, from which we can see that the magnitude of sea-breeze driven near-inertial motions is significantly suppressed during the synoptic wind event. This is because when synoptic winds are not present, sea breeze can build an in-phase relationship with the near-inertial current. This relationship can persist because the wind forcing and current have the same period. However, when a synoptic wind event passes by, this in-phase relationship can be interrupted and even be turned into an out-of-phase situation. As a consequence, the wind starts to remove energy from the current, and we see a significant drop of magnitude of near-inertial motions (Fig. 4.5). After the synoptic event passes by, the in-phase relationship between the wind and current is built up again. The inertial current energy starts to increase (Fig. 4.5). It can also be seen that when the synoptic wind event passes the location, the first baroclinic modal structure is suppressed. This experiment explains the reduced sea breeze driven near-inertial currents observed during the frontal events on the Texas-Louisiana Shelf in summer months (section 3.2.1).

4.2. Three-dimensional idealized case

4.2.1. Wave characteristics from 3-D idealized simulation

In order to investigate the latitudinal dependence of lateral propagation of sea breeze driven near-inertial motions and its effect on the vertical mixing, a three-dimensional idealized experiment is performed in a rectangular basin for 80 days. The

numerical model domain has 300 points in the latitudinal direction ranging from 18°N to 42°N, and 160 points in the longitudinal direction, with a uniform resolution of 10×10 km. The western boundary is set to no-slip wall, while the other open boundaries are radiation with a sponge layer. The water depth is a constant 200 m, and there are 20 vertical layers. Sea breeze forcing is applied at the western coast and decreases with a Gaussian distribution to zero approximately 300 km offshore. The numerical output in the sponge layer is excluded from all the analyses.

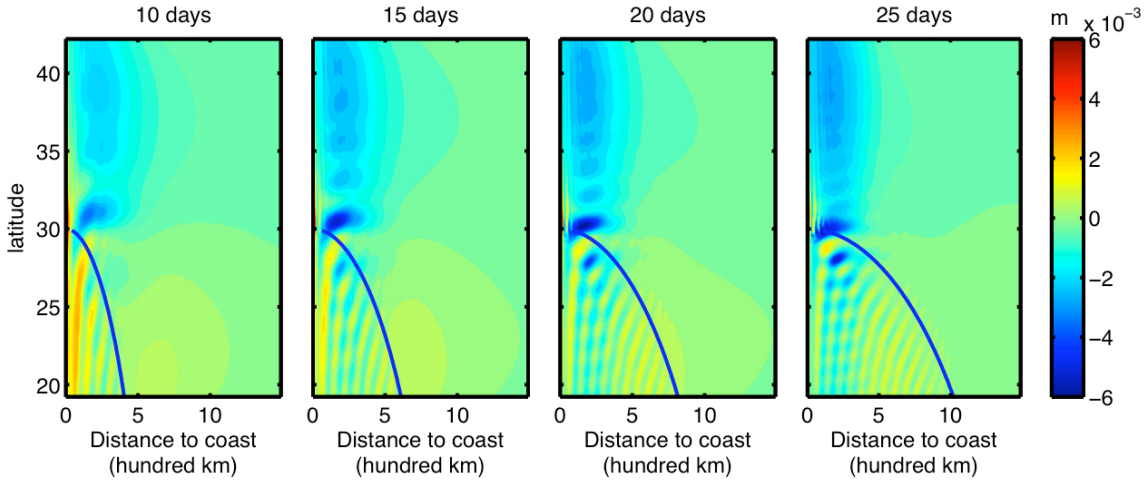

Fig. 4.6. Distribution of sea surface elevation for the 3D idealized simulation on days 10, 15, 20, and 25, respectively. Blue curves indicate the distance that the energy can propagate at different latitudes (south of 30°N) during different time periods based on the analytical solution of group speed for *Poincare* waves (Eqs. 4.1-4.4; distance = $C_{gx} \cdot t$, where t is equal to 10, 15, 20, 25 days, respectively). North of 30°N, the *Poincare* wave solution does not exist. The sea breeze driven energy is trapped to the coast in the forcing area. Note: sea breeze forcing extends from coast to 300 km only.

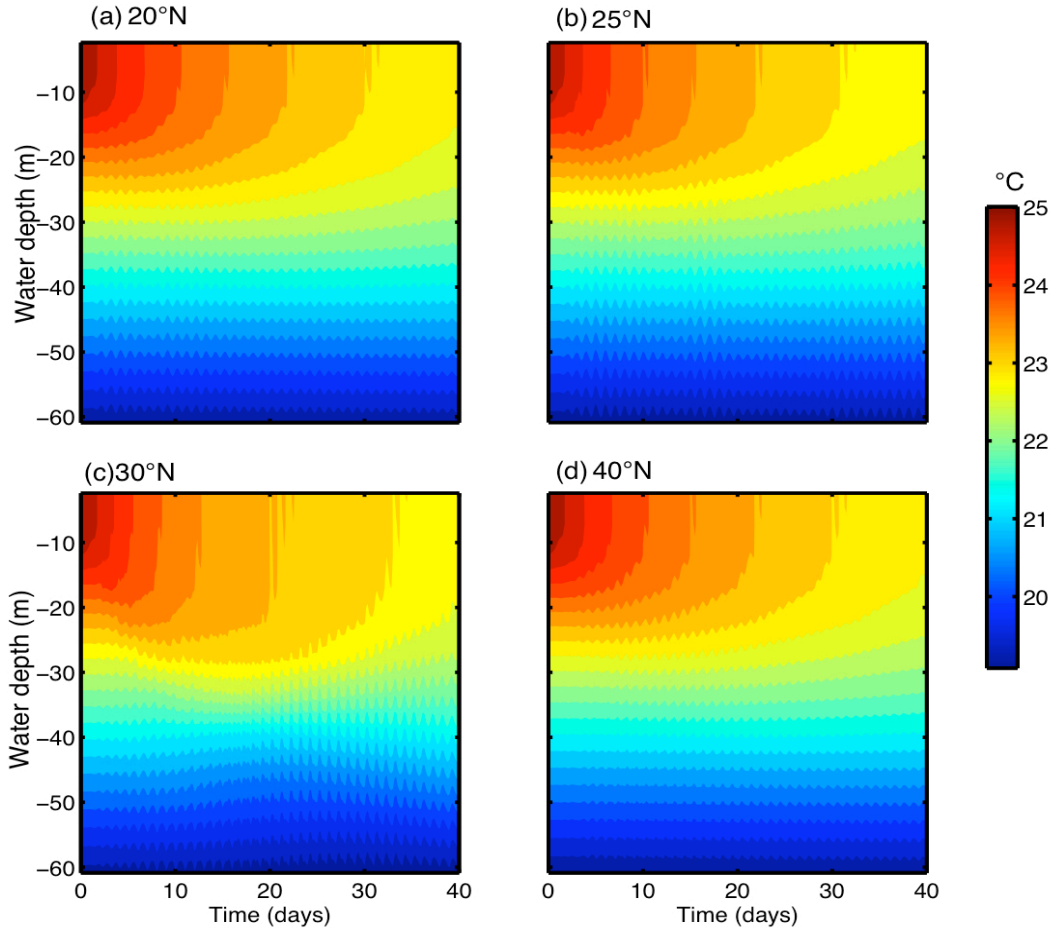

Fig. 4.7. Temperature fields at different locations along a north-south transect 70 km offshore for 3D idealized ROMS simulation (a) 20°N (b) 25°N (c) 30°N (d) 40°N. For clarity, only the upper 60 m is plotted.

In the three-dimensional simulation, the ocean response to sea breeze manifests as propagating internal *Poincare* waves. According to the wave theory (e.g., Pedlosky 1987), the dispersion relationship and the group speed components for *Poincare* waves in a two-layer ocean are

$$\omega = \pm\{f^2 + c_0^2(k^2 + l^2)\}^{1/2}, \qquad (4.1)$$

$$\frac{\partial \omega}{\partial k} = c_0^2 \frac{k}{\sqrt{f^2 + c_0^2 K^2}}, \tag{4.2}$$

$$\frac{\partial \omega}{\partial l} = c_0^2 \frac{l}{\sqrt{f^2 + c_0^2 K^2}}, \tag{4.3}$$

$$c_0 = \sqrt{g'h}, \tag{4.4}$$

where ω is the frequency of the waves, f is the *Coriolis* frequency, k and l are horizontal wave numbers for wave vector K, c_0 is the phase speed of the first-baroclinic mode waves, g' is the reduced gravity acceleration, and h is the depth of the thermocline corresponding to the first baroclinic mode. Fig. 4.6 shows the sea surface signature of *Poincar*e waves generated by sea breeze forcing at different time steps. It illustrates the evanescent latitudinal character and decay of the wave solution from 18°N to 42°N. By day 10, the wave field is fully developed. Although the forcing is only applied near the western coast, coastal ocean response propagates in the form of *Poincare* waves, and the near-inertial energy is redistributed and is transferred offshore. The *Poincare* wave solution, however, behaves quite differently poleward and equatorward of 30°. Poleward of 30°, the diurnal frequency is less than the local inertial frequency. As a consequence, the wave solution is evanescent and the coastal ocean response energy is trapped. However, equatorward of 30°, the diurnal frequency is greater than the local inertial frequency, and real wave solutions exist. Fig. 4.6 shows that the energy can propagate further away from the coast at lower latitudes, indicating a slower group speed of these waves near the critical latitude. However, the curvature of crest and trough lines shows that the phase speed of these waves is larger near the critical latitude. The propagation of

these near-inertial motions is consistent with the wave theory, in that *Poincare* waves have the characteristic that the group speed decreases with increasing latitude (Eqs. 4.2 and 4.3) making them more efficient in transferring energy offshore in the southern portion of the simulation domain. The distance that the energy can propagate based on the analytical group speed (Eqs. 4.1 - 4.4; $C_{gx} \cdot t$, where t is equal to 10, 15, 20, 25 days, respectively) is plotted on Fig. 4.6, from which we can see the offshore extent of the wave field in the model simulation agrees well with the analytical prediction.

After the horizontal distribution of sea surface signature is examined, a transect, which is 100 km offshore in the forcing area, is chosen to examine the latitudinal distribution of sea-breeze driven near-inertial motions and their effects on the vertical mixing in the water column. Fig. 4.7 shows the temporal evolution of temperature profiles at 20°N, 25 °N, 30°N, and 40 °N along this transect, respectively, from which we can see sea breeze is more efficient in deepening the mixed layer at the critical latitude. The 22.5°C isotherm reaches approximately 30 m after a 20-day run at the critical latitude. While at other latitudes, it is barely influenced by the sea breeze. Fig. 4.7 also shows the vertical stratification is weakest at the critical latitude indicating more mixing occurred. The temperature profiles at other latitudes display similar patterns (Fig. 4.7).

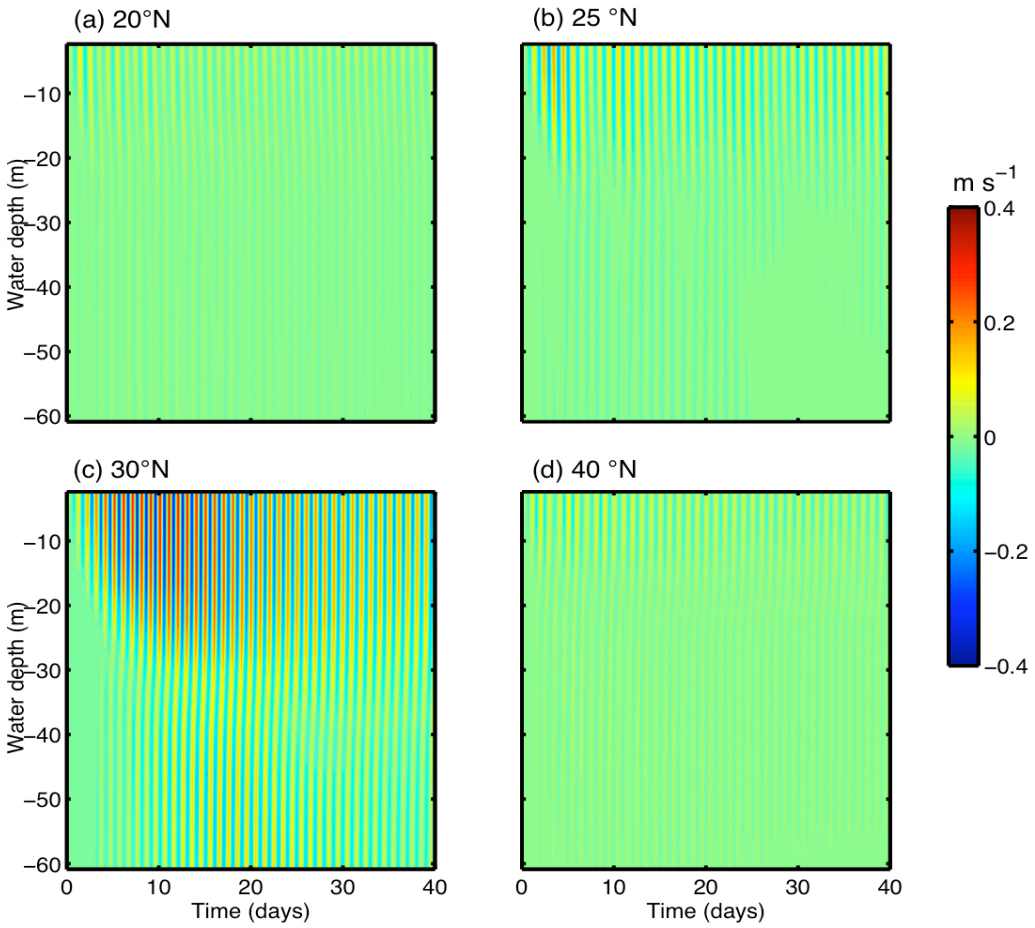

Fig. 4.8. Same as fig. 4.7 but for the east-west current component (a) 20°N (b) 25°N (c) 30°N (d) 40°N. For clarity, only the upper 60 m is plotted.

The east-west current profiles at these four different locations are shown in Fig. 4.8, which displays the maximum inertial ocean response at 30°N. The maximum current is about 40 cm s^{-1}which occurs after 10 days of forcing. The maximum current gradually decays with time after 20 days. Also the magnitude of the current from a three-dimensional simulation has similar magnitude as that from the two-dimensional simulation but much smaller than that from a one-dimensional calculation (Figs. 4.2, 4.4,

and 4.8). The magnitude of the currents at other latitudes decreases with the distance to the critical latitude.

The latitudinal distribution of temperature and vertical mixing coefficients along a transect 100 km offshore after 30 days is shown in Fig. 4.9. As can be seen, the sea breeze is more efficient in deepening the mixed layer near the critical latitude. From Fig. 4.9a, it can be seen that the mixed layer is deepest near 30°N reaching 32 m. It is only about 18 m deep at other latitudes. The vertical mixing coefficients are largest near 30°N. Although the forcing has the same magnitude along this transect, the vertical mixing coefficients are on the order of 0.01 $m^2 s^{-1}$ near 20 m at 30°N and at least an order of magnitude larger than those at other latitudes (Fig. 4.9b). This phenomenon can be explained by considering the energy available for vertical mixing at different latitudes. Near 30°N, the largest amount of oceanic inertial energy is generated by sea breeze because of resonance. However, the internal *Poincare* waves are inefficient in propagating energy offshore due to the small group speed there. This indicates that most of the inertial energy dissipates near the coast at the critical latitude, and contributes to the enhanced vertical mixing. I will quantify this phenomenon in the following section by evaluating terms in the energy equation for internal *Poincare* waves.

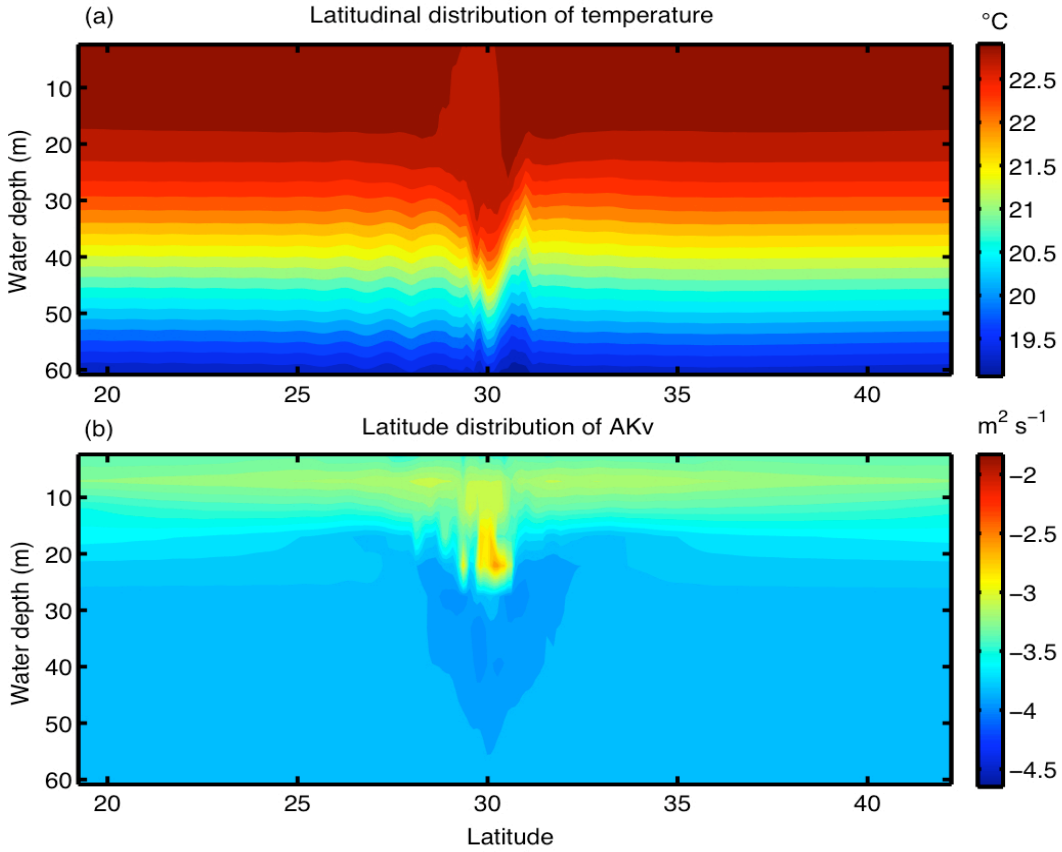

Fig. 4.9. Vertical sections of (a) temperature fields and (b) vertical mixing coefficients 100 km offshore after 30 days for the 3D idealized simulation. For clarity, only the upper 60 m is plotted. The colorbar for the panel b is in log scale.

4.2.2. Energy budget for the 3-D idealized case

In this section, the volume integrated energy equation for internal waves is evaluated with the output of the 3-D idealized numerical simulation (Eq. 4.5) (Nash et al. 2005).

$$\iiint_{v} \frac{\partial E}{\partial t} \cdot dv + \iiint_{v} (u \cdot \nabla) E \cdot dv = \oint_{ls} < u'p' > ds + \oint_{ss} \vec{\tau}_s \cdot \vec{u} ds + \oint_{bs} \vec{\tau}_b \cdot \vec{u} ds - Q_{\varepsilon}, \quad (4.5)$$

where $E(=KE+APE)$ is the energy density, KE $(=\vec{\rho}(<u^2>+<v^2>+<w>^2)/2)$ is the kinetic energy density, APE $(=\overline{\rho}\overline{N}^2<\varepsilon^2>/2)$ is the available potential energy density, $\varepsilon(z,t)$ is the vertical displacement of an isopycnal relative to its time-mean position, $\partial E/\partial t$ is the time rate of increase or decrease of energy density, $\vec{u}\cdot\nabla E$ is the advection of wave energy by mean velocity field, F_E $(=<u'p'>=\vec{c}_g E)$ is the energy flux carried by internal waves, $\vec{\tau}_s\cdot\vec{u}$ is the energy input from the wind, $\vec{\tau}_b\cdot\vec{u}$ is the energy removal by bottom drag, Q_- is volume integrated energy sinks associated with loss to turbulent dissipation, $<\cdots>$ indicates averaging over a few wave periods, $\iiint_v$ represents a volume integration, $\oint_{ls}$, $\oint_{ss}$. $\oint_{bs}$ represent area integrations over the lateral surface, sea surface, and sea bottom, respectively (Nash et al. 2005; MacKinnon and Gregg 2003; Kunze et al. 2002). The energy input by sea surface heat flux is not included in this equation because it is an order of magnitude smaller than the mechanical energy input from the wind.

The three-dimensional model is used to produce an 80-day time series of each term in Eq. 4.5 except the dissipation Q_-. These 80-day model outputs are then divided into twenty 4-day long segments. Each term in Eq. 4.5 (except Q_-) is calculated and time-averaged over this 4-day period (approximately 4 inertial wave periods). The advection of wave energy ($\vec{u}\cdot\nabla E$) and the energy removal by bottom drag ($\vec{\tau}_b\cdot\vec{u}$) are found negligible because they are at least an order of magnitude smaller compared to the energy flux carried out by internal waves ($F_E=<u'p'>=\vec{c}_g E$) and the energy input from

the wind ($\vec{\tau}_s \cdot \vec{u}$), respectively. Therefore, the energy available for vertical mixing (Q_-) at each latitude can be considered approximately as the residual of temporal change of the total energy for internal *Poincare* waves ($\partial E/\partial t$), the energy input from the wind ($\vec{\tau}_s \cdot \vec{u}$), and the energy removal from the lateral flux ($F_E = < u'p' > = \vec{c}_g E$). Since it is difficult to estimate $\vec{c}_g$ from the model output directly, the energy flux is calculated based on $< u'p' >$.

To compute the baroclinic energy flux, the internal-*Poincare*-wave-induced perturbation pressure p' and velocity u' can be inferred from density ρ and velocity u profiles from the model output (Nash et al. 2005). First, the density anomaly $\rho'(z,t)$ is calculated using the vertical displacement of an isopycnal $\varepsilon(z,t)$ relative to its time-mean position as

$$\rho'(z,t) = (\overline{\rho}/g)\overline{N}^2 \varepsilon(z,t), \tag{4.6}$$

The pressure anomaly $p'(z,t)$ is calculated from the density anomaly using the hydrostatic equation,

$$p'(z,t) = p_{surf}(t) + \int_z^0 \rho'(z,t) g dz, \tag{4.7}$$

The surface pressure $p_{surf}(t)$ can be inferred from the baroclinicity condition that the depth-averaged pressure perturbation must vanish,

$$\frac{1}{H}\int_{-H}^0 p'(z,t) dz = 0, \tag{4.8}$$

The perturbation velocity is defined as

$$u'(z,t) = u(z,t) - \overline{u}(z) - \overline{u}_0(t), \tag{4.9}$$

where $u(z,t)$ is the instantaneous velocity, $\overline{u}(z,t)$ is the time-mean of that velocity, and $\overline{u}_0(t)$ is determined by requiring baroclinicity:

$$\frac{1}{H}\int_{-H}^{0} u'(z,t)dz = 0, \tag{4.10}$$

The energy flux by internal waves is then estimated as $F_E = < u'p' > = \vec{c}_g E$, where $< \cdots >$ indicates averaging over a few wave periods.

The latitudinal distribution of time-volume averaged kinetic and potential energy over the period from day 17 to 20 is shown in Fig. 4.10 (integrated from the coast out to 50 km, 100 km, 200 km, and 500 km offshore, respectively). The kinetic energy of these internal *Poincare* waves is much larger than the potential energy near 30°N. The volume-normalized kinetic energy density is on the order of 1 J m^{-3}, while the potential energy density is on the order of 0.01 J m^{-3}. The ratio of these is ~O(100), which is consistent with the ratio between kinetic energy and potential energy for *Poincare* waves predicted by linear theory (Gill 1982),

$$\frac{KE}{APE} = \frac{\omega^2 + f^2}{\omega^2 - f^2}, \tag{4.11}$$

This ratio becomes large at 30°N ($\omega = f$). At other latitudes away from 30°N, this model KE/APE ratio is typically on the order of 1 (Fig. 4.10), which is also consistent with the analytical ratio (Eq. 4.11). As for the temporal change of the energy field, the volume-integrated total energy increases with time during the first 15 days with the gradual deepening of the mixed layer. The total energy density reaches maximum during the period days 16 to 20, when the mixed layer depth reaches its deepest and no longer deepens. The lateral energy flux starts to overcome the energy input from the wind, and

the energy density near the coast in the forcing area decreases gradually with time after day 20 (not shown).

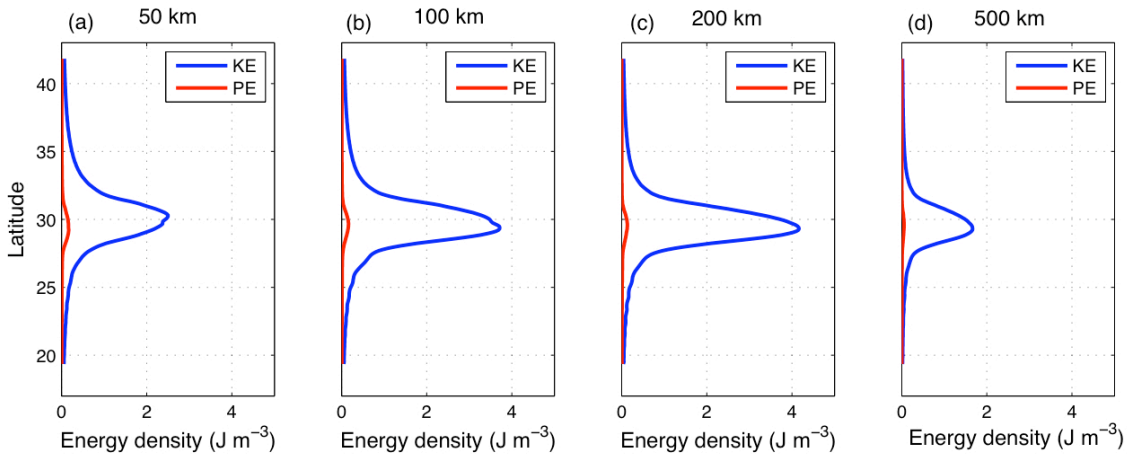

Fig. 4.10. Comparison of the volume-averaged kinetic and potential energy density as a function of latitude. Four panels correspond to four transects 50 km, 100 km, 200 km, and 500 km offshore, respectively (time-averaged over the period days 17 to 20).

Fig. 4.11 shows the temporal average (over the period days 17 to 20) of the energy input from the wind (panel a) and energy flux by internal *Poincare* waves (panel b) as a function of latitude and distance from the coast. Wind energy input is maximum (~10^5 Watts) at 30°N due to resonance, and is an order of magnitude larger than values at other latitudes although the magnitude of the wind forcing is uniform with latitude. Wind energy input is approximately symmetrical with respect to 30°N (Fig. 4.11a). In contrast, the lateral energy flux shows an asymmetric pattern on either side of 30°N (Fig. 4.11b). The maximum energy flux occurs near 30°N within 300 km offshore of the forcing area

(~ 10^6 Watts) (recall sea breeze extends to approximately 300 km offshore). Outside the forcing area, the lateral energy flux drops dramatically (~ 10^3 Watts at 500 km offshore) near 30°N, indicating a large horizontal flux gradient. In contrast, the energy flux is relatively small (~10^5 Watts) equatorward of 30°N in the forcing area, however, the lateral flux has similar magnitude within and outside the forcing area. At 500 km offshore, the energy flux peaks at ~25°N. The distribution of the magnitude of energy flux can be explained in terms of the distribution of group speed and energy of oceanic response to sea breeze. Although the group speed of *Poincare* waves is minimum near the critical latitude (Eqs. 4.1-4.4; for linear solution, the group speed is zero at 30°N.), the maximum energy density still makes the offshore energy flux largest at 30°N in the forcing area. Outside the forcing domain, the flux becomes much weaker because of the weak energy density and the small group speed. This indicates that near the critical latitude, sea breeze is very efficient in generating near-inertial energy because of resonance, however, the *Poincare* waves are inefficient in moving the energy offshore due to the small group speed. At lower latitudes south of 30°N, the sea breeze driven near-inertial motions are much weaker. However, the increased group speed makes the waves more efficient in transferring energy offshore. The direction of energy flux is generally southeastward (Fig. 4.11b) and consistent with the sea surface elevation distribution in Fig. 4.6. North of 30°N, the energy flux is small and trapped due to the absence of *Poincare* waves.

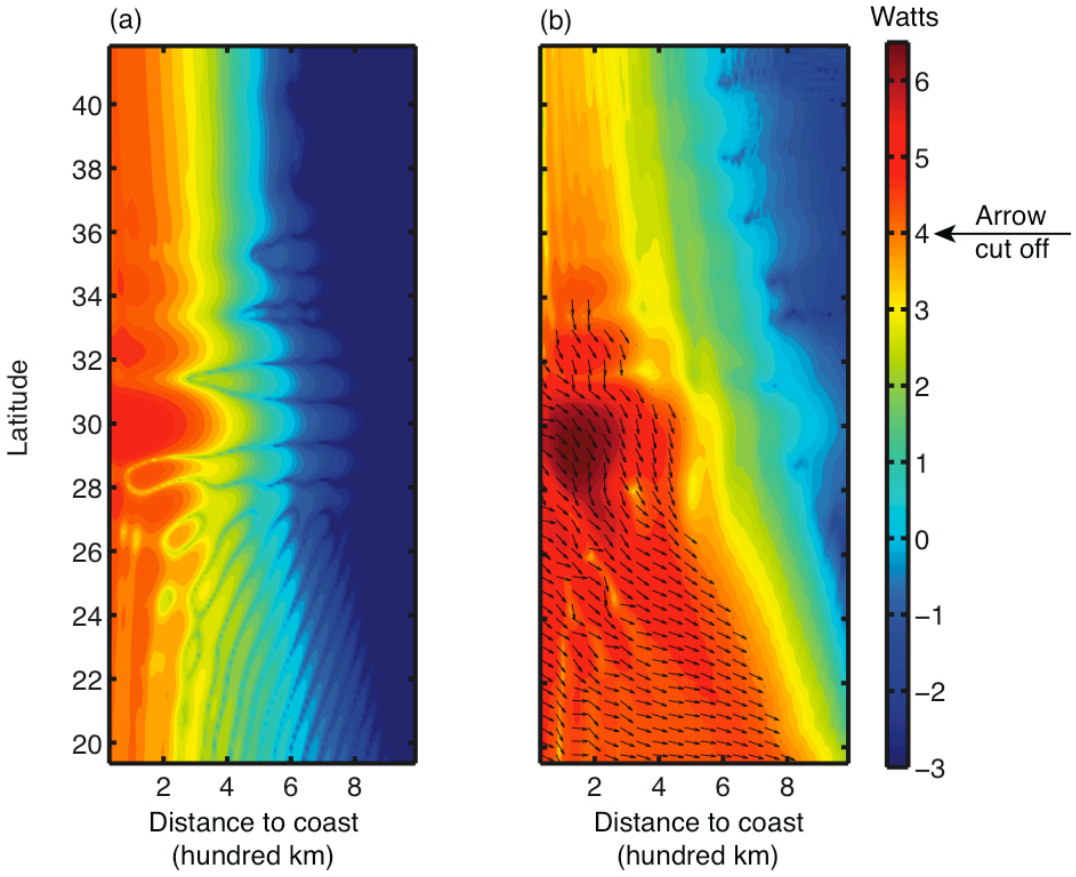

Fig. 4.11. (a) Time-averaged (over the period of days 17 to 20) magnitude of the energy input from the wind as a function of latitude and distance from the coast. (b) Time-averaged (over the period of days 17 to 20) lateral energy flux by internal *Poincare* waves as a function of latitude and distance to the coast. The color represents the magnitude of the flux. The arrows indicate the direction of the energy flux. Note: an arrow is plotted when the magnitude of the flux is greater than 10^4 Watts. The colorbar is in log scale. Sea breeze forcing extends from coast to 300 km only.

The temporal change of the lateral energy flux at 100 km and 500 km offshore is shown in Fig. 4.12. The horizontal flux at 100 km is maximum at 30°N during the whole period of 80-day simulation. However, little energy can reach 500 km offshore at 30°N even after 80 days (Fig. 4.12). Near 25°N, it takes about 20 days for the energy to

propagate to 500 km offshore indicating a 25 km day^{-1} group speed of *Poincare* waves at this latitude. The time for the wave energy to reach 500 km transect decreases with latitude, consistent with Fig. 4.12 and the larger group speed at lower latitudes. The temporal change of lateral energy flux at each latitude shown in Fig. 4.12 is caused by temporal change of the total energy density for the internal *Poincare* wave fields, which increases over the first 20 days and decreases gradually afterward.

After each term in Eq. 4.5 is analyzed, the residual energy ($Q\_$) is calculated in the water volume from the coast to 50 km, 100 km, 200 km, and 500 km offshore, respectively. The residual energy is then considered as the available vertical mixing energy. The latitudinal distribution of the residual energy averaged over the period days 17 to 20 is shown in Fig. 4.13. The residual energy is an order of magnitude larger at 30°N compared to other latitudes for these four different cases. This indicates more energy dissipates locally near the coast at 30°N, while the energy available for mixing is greatly reduced away from the critical latitude. Fig. 4.13 is shown here as an example, and during other periods the residual energy available for mixing displays similar patterns. This energy analysis explains why the idealized three-dimensional simulation shows enhanced vertical mixing and deeper mixed layer near the critical latitude (Fig. 4.9).

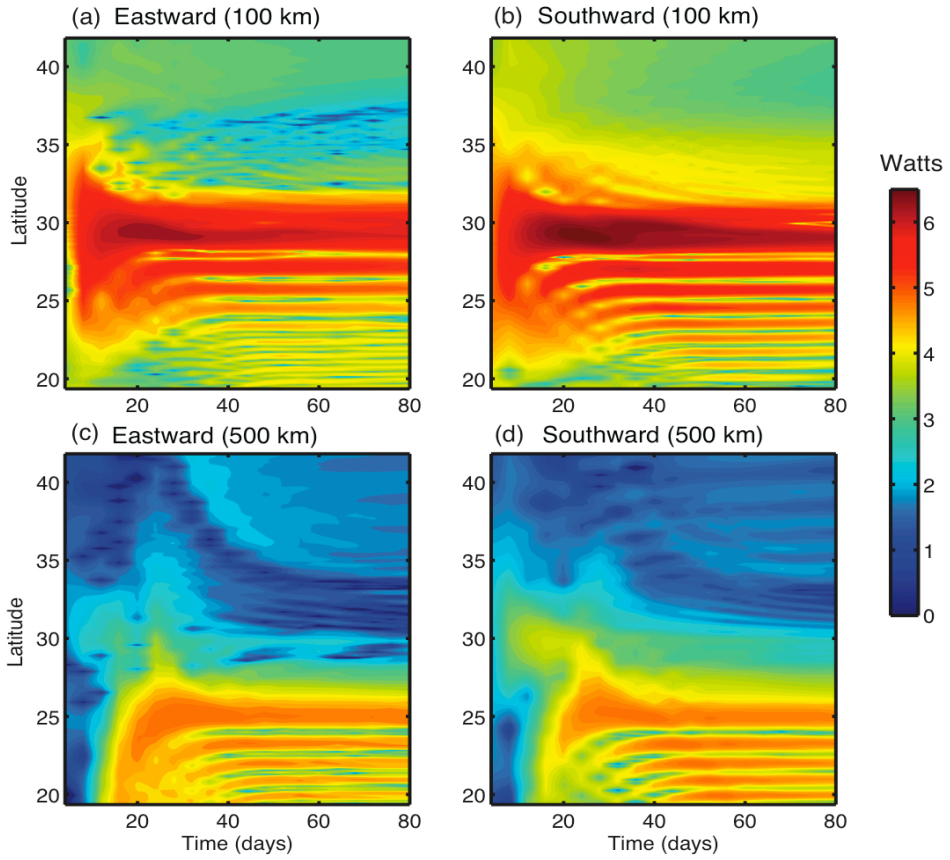

Fig. 4.12. (a) Eastward energy flux component across the transect 100 km offshore as a function of time and latitude. (b) Same as (a) but for the southward energy flux component. (c) Eastward energy flux component across the transect 500 km offshore as a function of time and latitude. (d) Same as (c) but for the southward energy flux component. Note: the colorbar is in log scale.

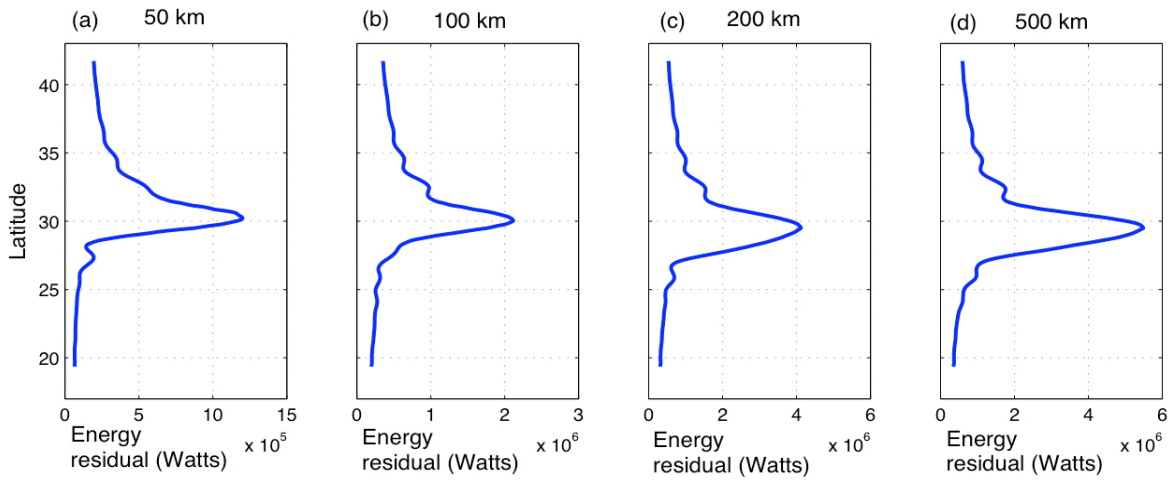

Fig. 4.13. Residual energy (energy available for vertical mixing; Q_{-} in Eq. 4.5) as a function of latitude. Four panels correspond to four transects 50 km, 100 km, 200 km, and 500 km, respectively (time-averaged over the period days 17 to 20).

4.3. Application for the Gulf of Mexico

A three-dimensional realistic case incorporating the bathymetry of the Gulf of Mexico is conducted to examine the ocean response to sea breeze in the real ocean near the critical latitude. The centers of the model grid cells used are shown in Fig. 4.14. Sea breeze is applied in a coastal strip extending approximately 300 km from the western and northern coasts. The magnitude of sea breeze is 4 m s^{-1} at the coast, and it decreases offshore gradually by a Gaussian taper function. Sea surface heat flux forcing and other initial conditions are identical to those used in the previous cases. To isolate the sea breeze effect, no other forcing is applied (e.g., tides, existing mesoscale flows, and buoyancy-driven river plume structures are excluded).

The previous numerical experiments have confirmed that the oceanic response to

sea breeze forcing depends significantly on the latitude of the coastal ocean (Figs. 4.2 and 4.8) and inertial response in form of *Poincare* waves occurs in the numerical simulations but is limited to latitudes below 30°N (Fig. 4.6). This makes the Gulf of Mexico particularly suited to study this phenomena in this regard, because the northern coastline of the Gulf of Mexico is approximately at 30°N, and spans more than 1000 km from 97°W to 84°W. Nearly all of the Gulf of Mexico lies to the south of 30°N. The simulations described in this section consider whether or not other factors such as coastline irregularities and bathymetry alter the *Poincare* wave response.

Fig. 4.15 shows the vertical component of the relative vorticity field ($\upsilon_x - u_y$) at 25 m from the Gulf of Mexico simulation. Red (blue) indicates anticyclonic (cyclonic) vorticity and illustrates the *Poincare* wave field that results after 6, 8, 10, and 12 days of sea breeze forcing, respectively. In contrast to the previous simulations, however, the *Poincare* wave crest structure is less regular with wave crests emanating from the curved coastal boundary. Regions of enhanced wave variability are clearly visible in the figure near DeSoto (28°N, 87°W) and Alaminos (27°N, 95°W) Canyons and east of the East Mexico Slope (between 21° and 25°N and 96°W). The waves have wavelengths of 100 km and phase speed of ~50 km day^{-1} and are able to propagate into the interior of the Gulf on short time scales, i.e., order of 10 days. Regions of wave propagation transport energy offshore preferentially in the SW, NW and NE corners of the Gulf. This indicates, in addition to latitudinal dependence, the wave response is largest in three regions in the Gulf where coastal bathymetry curvature is maximal. The theoretical phase speed of these *Poincare* waves can be estimated basing on the dispersion

relationship (Eq. 4.1). Assuming $g' = 0.01$ m s^{-2}, $h' = 10$ m, $k = l = 1\times10^{-5}$ m^{-1}, $f = 9.04\times10^{-6}$ s^{-1}, wave celerity $C_{px} \approx 80$ km day^{-1}. The celerity estimated from the model simulation is consistent with the theoretical wave theory.

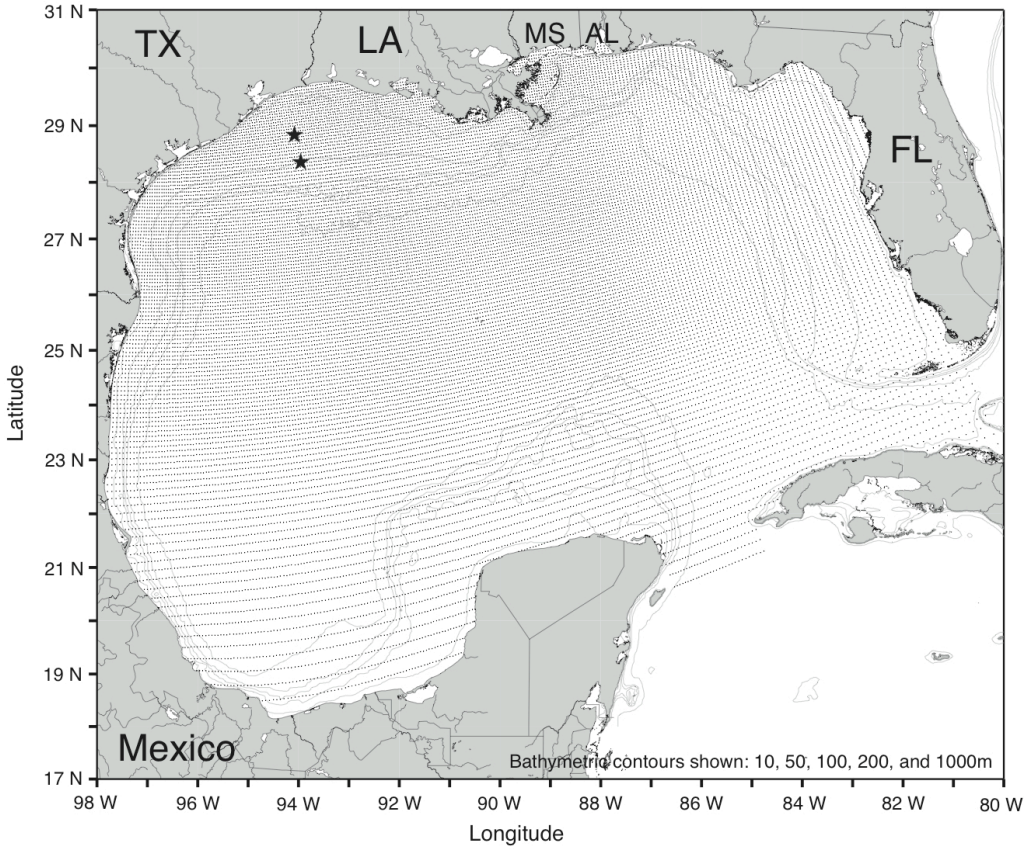

Fig. 4.14. Grid centers for the realistic Gulf of Mexico simulation. The two stars represent the locations of LATEX moorings 21 (28.84°N, 94.08°W) and 22 (28.36°N, 93.96°W).

Fig. 4.16 shows the temporal evolution of the model temperature profiles at the locations of LATEX moorings 21 (28.84°N, 94.08°W) and 22 (28.36°N, 93.96°W) on

the Texas-Louisiana Shelf (on map Fig. 4.14), which are close to the critical latitude. These locations are chosen to illustrate how vertical mixing near 30°N is influenced by water depth. The model outputs are discussed first, and observations from these mooring locations are shown and discussed later. Model mooring 21 has a total water depth of 24 m. Initially, the mixed layer depth is about 10 m, with a uniform temperature of 25°C. Below the mixed-layer depth, the temperature decreases with depth, and reaches 20 degrees near the bottom. The mixed layer depth starts to increase with time during the first two weeks after sea breeze starts to blow on top of the sea surface. After about two weeks, the water column at model mooring 21 becomes fully mixed, and the temperature changes to approximately 22.5°C throughout the water column. A 2.5°C temperature change in the mixed layer indicates the occurrence of strong vertical mixing. The ocean response shows a first baroclinic modal structure as seen previously in the 3-dimensional idealized case. However, it is noted that after the water column becomes fully mixed, the first-baroclinic modal structure persists with smaller amplitude (reduce from 20 cm s^{-1} to 5 cm s^{-1}; Fig. 4.16b). After the water column becomes fully mixed, the vertical mixing coefficients become large throughout the water column (Fig. 4.16c). This model result indicates that continuous sea breeze can significantly enhance the vertical mixing in the water column on the middle Texas-Louisiana Shelf during the summer months. Based on LATEX wind observations, sea breeze can persist for 2 weeks on the Texas-Louisiana Shelf without interruptions in the summer months (Zhang et al. 2008). It has been observed that the stratification in the water column at the LATEX moorings 21 and 22 is significantly suppressed during those uninterrupted sea breeze periods (section 6 for

details).

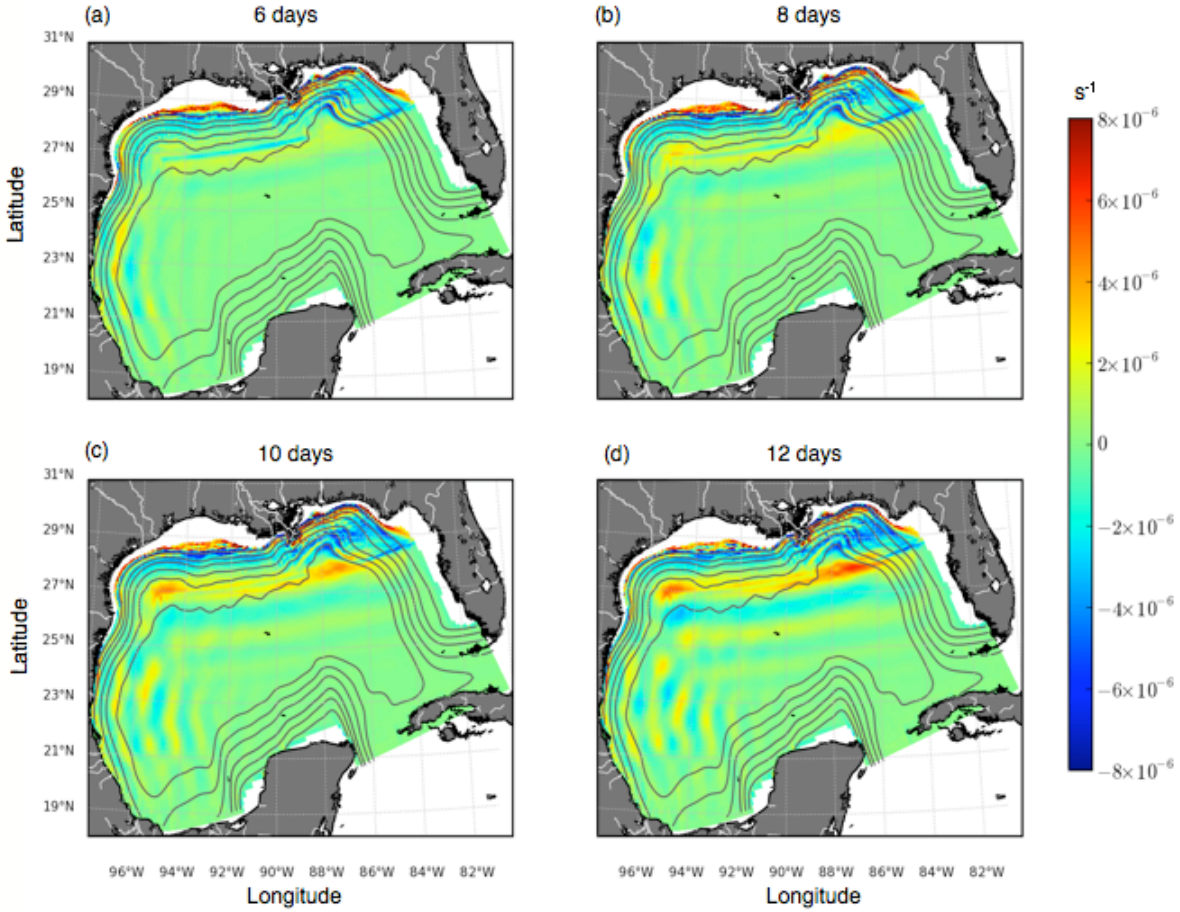

Fig. 4.15. Distribution of the vertical component of relative vorticity ($\upsilon_x - u_y$) field at 25 m at different time steps (a) 6 days (b) 8 days (c) 10 days (d) 12 days for the realistic GOM simulation. Red (blue) indicates anticyclonic and (cyclonic) vorticity.

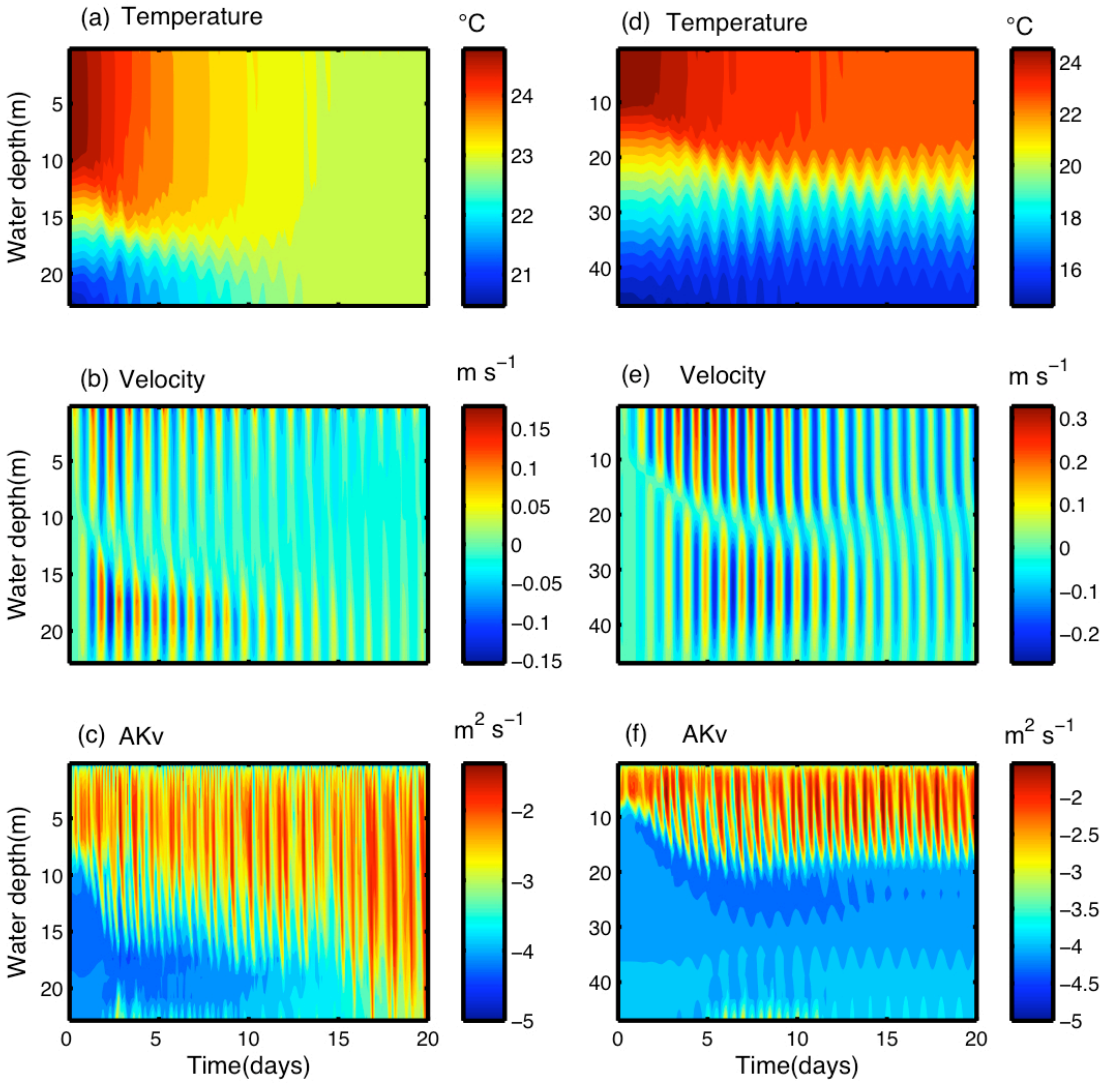

Fig. 4.16. Temporal evolution of model output temperature, east-west current component and vertical mixing coefficient fields at moorings 21 (left column) and 22 (right column) for the 3D realistic GOM simulation (see fig. 4.14 for locations). Note: the water depth and the colorbar are in different scale for clarity. The colorbar for the bottom row is in log scale.

The results at the location of model mooring 22 (total water depth 55 m) display a quite different situation, as the water column never fully mixes (Fig. 4.16def). However,

the mixed layer can reach to 20 m after ten days of continuous sea breeze forcing. Afterwards, the base of mixed layer starts to level off, and oscillate around 20 m. No further deepening occurs at model mooring 22 although sea breeze still exists in the following 10 days. Comparing results at model moorings 21 and 22 illustrate that sea breeze deepening of the mixed layer to the bottom is limited to the shallow water regions (<50 m).

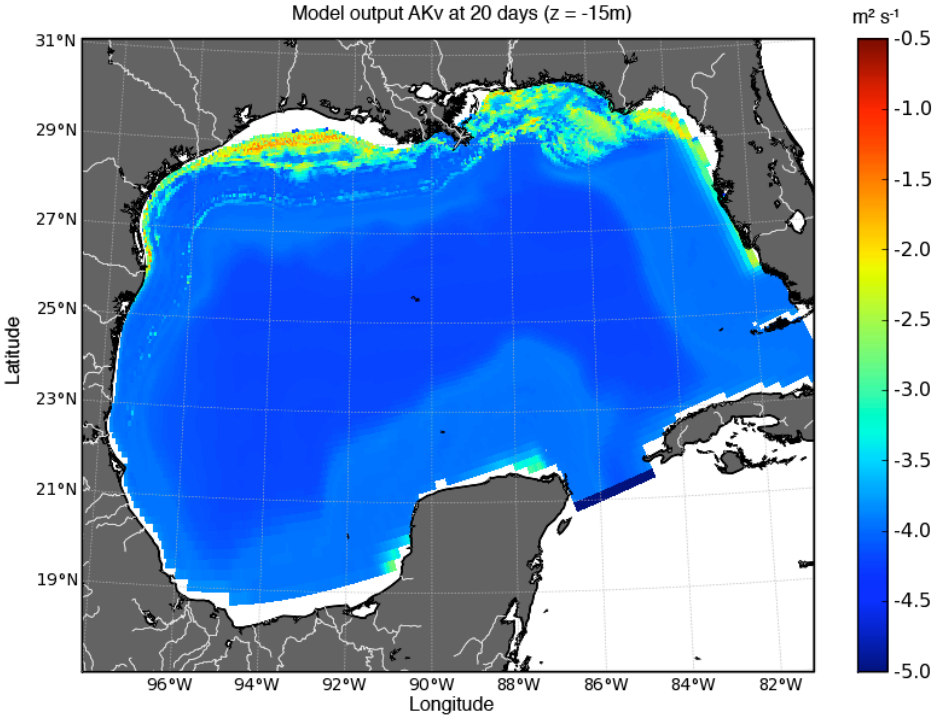

Fig. 4.17. Synoptic snapshot of vertical mixing coefficients at 15 m depth after 20 days for the 3D realistic GOM simulation. The colorbar is in log scale.

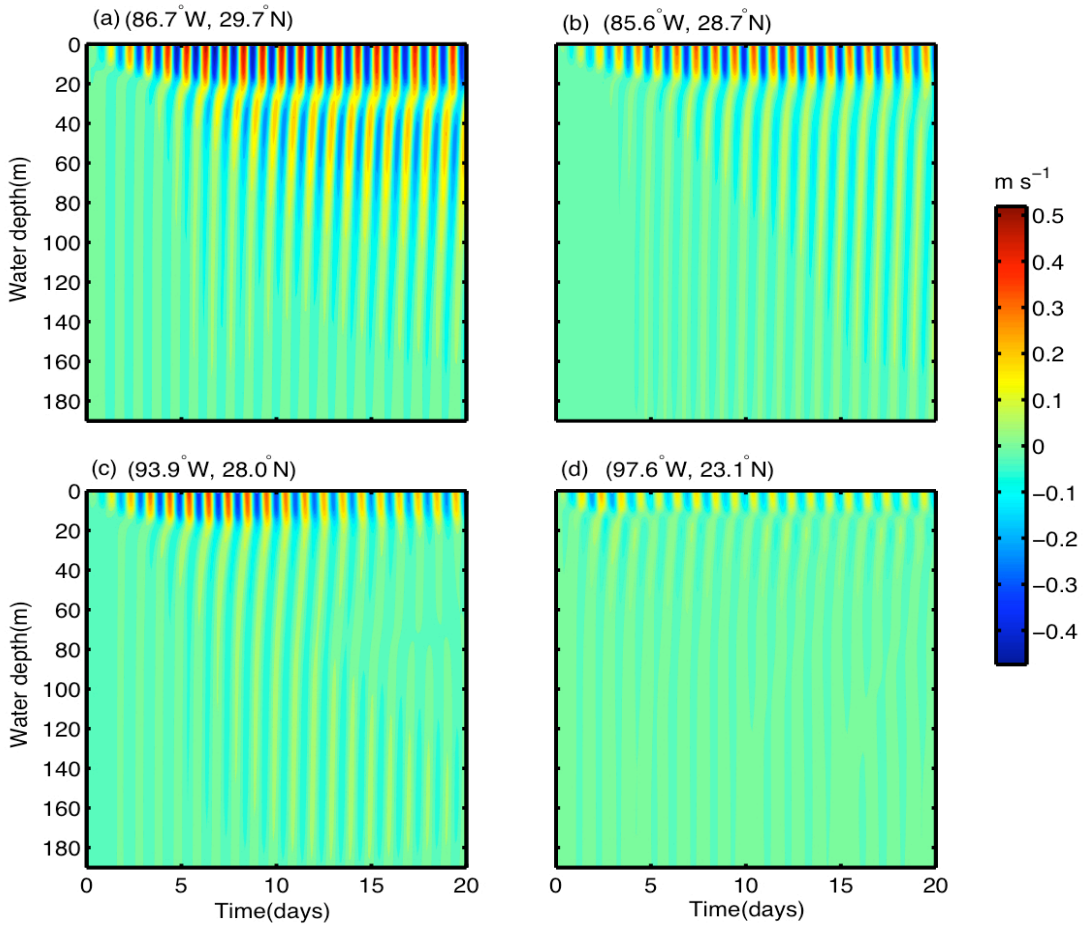

Fig. 4.18. Temporal evolution of current profiles at different latitudes along the 200-m isobath for the 3D realistic GOM simulation. (a) (86.7°W, 29.7°N) (b) (85.6°W, 28.7°N) (c) (93.9°W, 28.0°N) (d) (97.6°W, 23.1°N).

Fig. 4.17 is a synoptic snapshot of the vertical mixing coefficients at 15 m depth at the end of the 20-day simulation. The amplitudes are very similar at 5 m and 10 m on the northern and western shelves (not shown) (recall sea breeze forcing is only applied near the northern and western coasts). However, at 15 m, the vertical mixing coefficients are much larger near the northern boundary than the western boundary. This is consistent with the three-dimensional idealized simulation (Fig. 4.9). As discussed in the previous

section, the northern shelf of the Gulf of Mexico is close to 30°N, where the oceanic response is strongest and a large amount of energy dissipates locally and enhances vertical mixing because of the small group speed of *Poincare* waves. Further southward away from 30°N, less near-inertial energy is available for vertical mixing as a consequence of the weaker response to sea breeze and the larger group speed of near-inertial motions at lower latitude.

A consequence of the high vertical mixing coefficients on the northern shelf is that the water column can attain a deeper mixed layer. Fig. 4.18 displays the temporal evolution of current profiles at different latitudes along the 200 m isobath. The mixed layer depth is indicated in Fig. 4.18 by the depth of velocity reversal, which is ~ 30 m near 30°N (Fig. 4.18a) and ~10 m near 23°N (Fig. 4.18d). The oceanic inertial response is ~50 cm s^{-1} and strongest near 30°N (Fig. 4.18a), while it is less than 20 cm s^{-1} near 23°N (Fig. 4.18d).

CHAPTER V

DISCUSSION*

5.1. Cross-shelf phasing of sea breeze

The analyses of observations presented in this study have provided some new details of the character of the sea breeze wind field over the Gulf. Since the wind vectors in Fig. 3.2 represent a synoptic snapshot of the diurnal winds at 7 PM local time and all rotate clockwise, it can be seen that sea breeze blows onshore approximately from 9 PM to 8 AM and offshore from 9 AM to 8 PM in the middle of the shelf. This is counterintuitive with the traditional idea of onshore sea breeze during the day and offshore sea breeze at night, but consistent with the previous theoretical and numerical simulations (Rotunno 1983; Yan and Anthes 1987), which attributed this to a dominance of the Coriolis force over the thermal induced pressure gradient equatorward of 30°N/S. The same theory and numerical simulations also predicted poleward of 30°N/S, sea breeze winds are in phase with the heating cycle. The fact that sea breeze blows onshore north of 30°at 7 PM at stations DPIA1 and 42007 (Fig. 3.2) and in the opposite direction of sea breeze in the middle shelf, is in agreement with their theory and numerical simulations. However, I realize that this phase shift at those two stations might also be related to the complexity of the coastline, and more measurements over a larger spatial

* Part of this chapter is reprinted with permission from "Near-resonant ocean response to sea breeze on a stratified continental shelf" by X. Zhang, S. DiMarco, D. Smith, M. Howard, A. Jochens, and R. Hetland, *Journal of Physical Oceanography*, Copyright 2009 by American Meteorological Society.

scale are needed to fully evaluate this phenomenon in the future.

However, that the phasing of the onshore wind along the Texas coastline can be quite complicated. For example, by comparing the phase of the onshore wind of Fig. 3.2, it is noted that the diurnal wind will blow shoreward near Port Aransas, TX, roughly five hours prior to a shoreward breeze at Sabine, TX. Cases are also documented in which the onshore/seaward oscillation is in phase along the curved coastline. Whether this is due to differential heating and cooling along the coastline or to larger mesoscale wind variability is not clear and warrants further investigation.

5.2. Parametric sub-harmonic instability

This study examines the near resonant near-inertial coastal ocean response to sea breeze forcing near the critical latitude. Previously, modeling results and observations have demonstrated a locally enhanced near-inertial energy and decreased semidiurnal tidal energy near 30° N/S, which are partially due to another critical latitude mechanism: parametric sub-harmonic instability (PSI) (van Haren 2005, 2007). This mechanism that involves nonlinear transfer of energy among energetic tidal frequency ocean wave modes was not considered in the previous sea breeze papers. MacKinnon and Winters (2005) found significant energy transfer from semidiurnal tides to higher frequency near-inertial motions near 28.9°N using numerical simulations. Since the mooring locations are so close to this latitude, it is necessary to address this mechanism and my rationale for excluding it as a resonant mechanism on the Texas-Louisiana Shelf in more detail.

I believe the enhancement of near-inertial energy on Texas-Louisiana Shelf in summer is not mainly caused by PSI for the following reasons. Firstly, the dominant semidiurnal tide M2 is weak on the Texas-Louisiana Shelf, with an averaged amplitude of roughly 5 cm s^{-1} at mid shelf, and less than 1 cm s^{-1} at the shelf edge, which is an order of magnitude smaller and less than the near-inertial motions in summer (DiMarco and Reid 1998). The north-south semi-diurnal tidal current time series at mooring 22 in summer 1994 displays small variability from June to August (Fig. 3.6, lower panel). The tidal current ranges from 3.5 cm s^{-1} (neap tide) to 5.3 cm s^{-1} (spring tide) at this location. This is not consistent with the variation of near-inertial band variance during the same period (Fig. 3.6, middle panel). Secondly, there is no evidence that indicates the semi-diurnal tides are larger in summer than the non-summer seasons. Therefore, if the PSI mechanism is important on the shelf, we should see a transfer of semi-diurnal tidal energy to the near-inertial band in all seasons. However, these motions are much weaker during the non-summer seasons. Thirdly, modeling results and observations suggest PSI might be important near the hot spots of baroclinic semidiurnal tidal energy conversion (e.g., mid-ocean ridges) (van Haren 2005; Simmons et al. 2004). However, the Texas-Louisiana Shelf has a very shallow wide bathymetry and the baroclinic semidiurnal tidal conversion rate is low in the Gulf of Mexico (Simmons et al. 2004), which makes PSI less likely to be important in the Gulf.

5.3. Comparison between observations and numerical simulations

Although all of the numerical simulations presented in Chapter IV are driven by idealized forcing (e.g., sea breeze and sea surface heat flux), some qualitative comparisons can be made on sea breeze driven near-inertial motions between the LATEX observations reported in Chapter III and the model output shown in Chapter IV.

a. Oceanic response to sea breeze forcing

Observational results during summer on the Texas-Louisiana Shelf (~30°N) indicate that the ocean response to sea breeze has a first baroclinic modal structure near the coast. The coastal near-inertial ocean response is significantly enhanced near the critical latitude. Although the maximum sea breeze on the shelf is only about 4 m s^{-1}, the current can be as strong as 60 cm s^{-1} after 10-day of continuous forcing near the critical latitude. The model results are consistent with the observations on the Texas-Louisiana Shelf (Zhang et al. 2008).

b. Comparison of effects on mixing

Observations on the Texas-Louisiana Shelf (~30°N) show that strong sea breeze driven near-inertial motions can significantly enhance the vertical mixing in the water column by increasing the velocity shear and suppressing the stratification in the water column (Zhang et al. 2008). Fig. 5.1a shows the time series of near-surface (3m) near-inertial current at LATEX mooring 22 in June 1994. Sea breeze forcing with the magnitude of ~4 m s^{-1} persists continuously during the period of 5-15 June 1994. As a

consequence, the near-inertial current reaches ~60 cm s^{-1} by the end of this period. Fig. 5.1b displays the density difference between the top (3m) and middle (23m) meters, as calculated from the temperature and conductivity (salinity) measurements. It shows that the mean density difference (black curve in Fig. 5.1b) in the water column decreases from around 6.5 kg m^{-3} at the beginning of this period to approximately 2.5 kg m^{-3} near 15 June, which indicates that the sea breeze driven near-inertial motions have generated significant vertical mixing in the water column. The instantaneous density difference (gray curve in Fig. 5.1b) reaches zero around 15 June, showing that the depth of the mixed layer has reached at least 23 m during this sea breeze event, as opposed to the typical mixed layer depth of a few meters at mooring 22 in June. Strong diurnal variabilities in the density difference time series (gray curve in Fig. 5.1b) have been associated with the effects of tidal straining of the horizontally varying density field in the Irish Sea (Simpson et al. 1990; Rippeth et al. 2001; Thorpe et al. 2008). Here however the straining is caused by the sea breeze driven near-inertial motions. Sea breeze is suppressed during the period of 17-20 June. The near-inertial current is reduced and the density difference returns to 6 kg m^{-3} around 22 June 1994, indicating a reestablishment of the strong stratification in the water column (Fig. 5.1b). This observational evidence indicates that ~ 4 m s^{-1} sea breeze on this shelf can significantly enhance the vertical mixing in the water column during the summer time. It is consistent with our three-dimensional idealized and realistic Gulf of Mexico experiments, which show enhanced vertical mixing near 30°N (Figs. 4.9 and 4.17), and our energy budget

calculation, which shows that sea breeze is more efficient in promoting vertical mixing near 30°N (section 4.2.2).

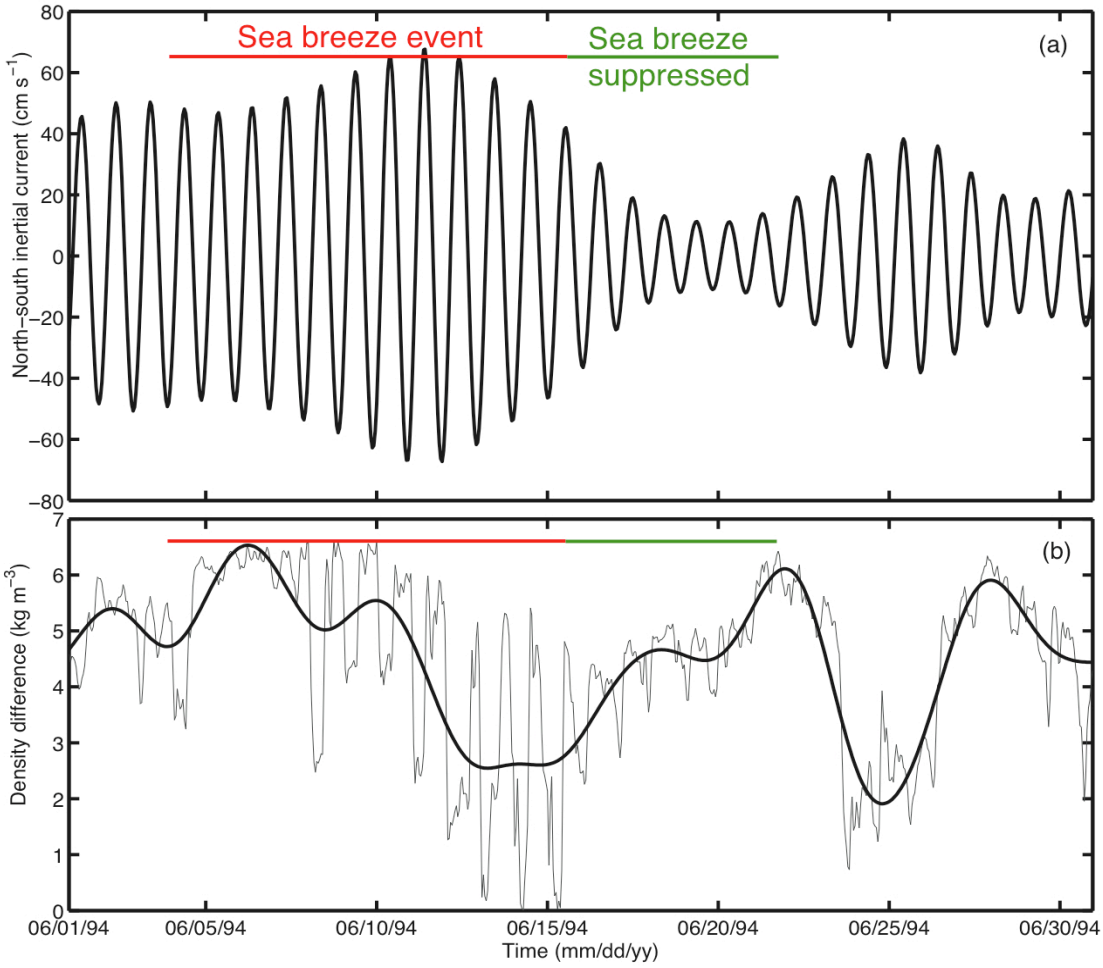

Fig. 5.1. (a) Bandpassed north-south near-inertial current time series (0.83cpd ~ 1.17cpd) observed at the top meter (3m) of mooring 22 in June 1994 during the LATEX project. The red line corresponds to a sea-breeze event (strong sea breeze based on the wind records) in this month. The green line indicates a period when sea breeze is suppressed at mooring 22 around June 17. (b) Same as (a) but for the density difference time series between the top meter (3m) and the middle meter (23m) at mooring 22. The gray thin line and the thick black line represent the hourly and 3-day low-passed density-difference time series, respectively. The stratification is weakened during the sea breeze event, and the water column is re-stratified when sea breeze is suppressed.

c. Indication of near-inertial *Poincare* wave propagation in the water column

Mooring data on the Texas-Louisiana Shelf indicate that when there are no synoptic wind events, the sea breeze forcing is primarily in phase with the near-inertial currents in the surface mixed layer with high and significant correlation (>0.9) (Zhang et al. 2008). This indicates that most of the near-inertial energy is locally generated, which is consistent with the relatively low group speed of the *Poincare* waves near the critical latitude (Fig. 4.6). Although Zhang et al. (2008) did not have ocean observations south of 27°N in the Gulf, results of this paper suggest that the in-phase relationship between the wind and oceanic response is likely more complicated away from 30°N, as the near-inertial band motions contain both locally and remotely generated propagating *Poincare* wave signature.

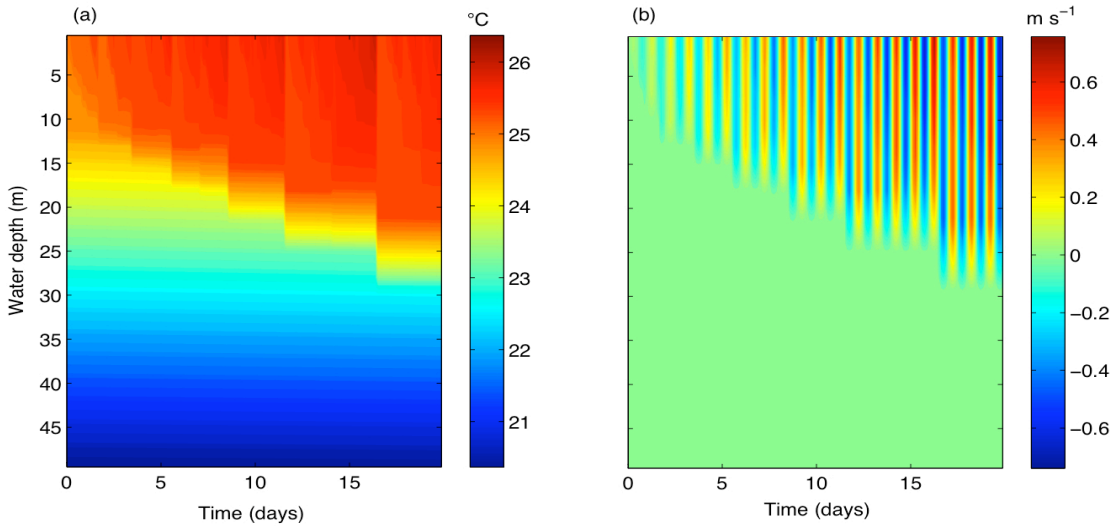

Fig. 5.2. Distribution of (a) temperature (b) velocity fields from PWP model. Same model setup as 1D ROMS simulation (Compare with Figs. 4.1 and 4.2).

5.4. Comparison with Price-Weller-Pinkel (PWP) model

To verify the results from the one-dimensional ROMS simulation, they are compared with those from the classic PWP model (Price et al. 1986). PWP model is a one-dimensional model widely used by oceanographers to study the oceanic response to wind forcing and the mixed layer dynamics. The PWP model is set up in the exact same way as the one-dimensional ROMS simulation for the case of 30°N. The temporal evolution of temperature and current profiles from PWP model is shown in Fig. 5.2. Comparing Fig. 5.2 and Figs. 4.1 and 4.2, we can see that they display very similar patterns, except that the results from ROMS simulation are smoother. Since Price et al. (1986) use the bulk and gradient *Ri* as the control of the deepening of the mixed layer depth and the corresponding mixing coefficients, the consistency between these two models indicate ROMS simulations have similar physics behind it. The deepening of mixed layer caused by sea breeze forcing mainly is controlled by the shear-instability.

5.5. Limitation of one-dimensional model

There are several significant differences between the one-dimensional and three-dimensional simulations of oceanic response to sea breeze. Firstly, the vertical structure of the current profiles in the three-dimensional simulation shows a first baroclinic modal structure instead of just a surface trapped jet (Compare Figs. 4.2, 4.4 and 4.16). This is consistent with previous research on sea breeze driven near-inertial motions (e.g., Simpson et al. 2002; Rippeth et al. 2002), which has proven the flow in the bottom layer is driven by the barotropic pressure gradient set up by the no-flow conditions at the

walls. In the one-dimensional case, a pressure gradient (i.e., surface tilt or isopycnal tilt) does not exist. Therefore, the current is trapped to the surface layer where the water is directly forced by the winds. Vertically the profile displays an Ekman spiral with the magnitude of the current decreasing exponentially with depth. Secondly, the magnitude of near-inertial currents at the critical latitude in the one-dimensional simulation can reach 70 cm s^{-1}, which is much larger than that in the three-dimensional simulation (Compare Figs. 4.2 and 4.16). Thirdly, the mixed layer depth reaches a steady state near the critical latitude after 10-day forcing in the three-dimensional realistic simulation (Fig. 4.16). However, this steady state can never be established in the one-dimensional simulation (Fig. 4.2c).

Through a comparison between the one- and three- dimensional models, I found that the one-dimensional model has limited applicability to study the oceanic response to sea breeze near the critical latitude primarily because it cannot reproduce the propagating wave field shown in the three-dimensional model. Because of this, it overpredicts the mixed layer deepening. The energy redistribution by the wave field is crucial and cannot be neglected near the critical latitude. At other latitudes, this may play a less important role because the strength of these waves is much weaker.

5.6. Significance of enhanced vertical mixing by diurnal wind forcing near the critical latitude – comparison with other critical latitude mechanisms

One of the primary findings of this research is that sea breeze can significantly promote the vertical mixing near the critical latitude. Vertical mixing affects many

biogeochemical processes as well as physical. Therefore, the seasonality of sea breeze induced mixing may enhance or limit these processes especially during the summer months. For example, hypoxia occurs in the summer months every year on the northern shelf of the Gulf (Wiseman et al. 1997; Hetland and DiMarco 2008). This summer sea breeze forcing could be a mechanism to ventilate the near-bottom hypoxic water, and mitigate the negative effects of hypoxia. The role of sea breeze in hypoxia has not yet been examined.

Mechanisms that produce enhanced localized vertical mixing have received attention recently as attempts to determine global energy dissipation locations (Munk and Wunsch 1998). However, these mechanisms have failed to account for global values need to close the energy budget. Parametric sub-harmonic instability (PSI) is a recently reported mechanism that can produce enhanced near-inertial baroclinic mixing near 30° latitude and is produced by the interaction of barotropic tides with steep topography (van Haren 2005, 2007; MacKinnon and Winters 2005). It is interesting to note that sea breeze driven near-inertial baroclinic mixing produces a comparable result for a different reason near 30° latitude. Our results indicate that in coastal regions where PSI is not expected to be a significant factor due to shallow topography and weak tides (Zhang et al. 2008), sea breeze driven ocean resonance may still produce enhanced vertical mixing near 30° latitude.

CHAPTER VI

CONCLUSIONS AND FUTURE DIRECTIONS*

This study illustrates the spatial and temporal evolution of sea breeze and the near resonant inertial oceanic responses and associated mixing to sea breeze on the Texas-Louisiana Shelf in the Gulf of Mexico using both field observations and numerical modeling. Data considered include wind, current and hydrography measured during the LATEX study. Numerical simulations use non-linear models from a simple one-dimensional model to a three-dimensional model of Gulf of Mexico. Specific new results are as follows:

(1) The temporal and spatial structure of sea breeze on the Texas-Louisiana Shelf is examined. Diurnal wind energy in summer is significantly enhanced both at the nearshore stations and at those stations as far as 300 km offshore (the offshore extent of available wind observations). The sea breeze winds are not trapped to the coast in summer, as previously thought, but extend to at least 300 km from the coast and also propagate with time from the coast outward with offshore observations lagging those at the coast by as much as 3 hours. These results are in agreement with linear theory, which posits that equatorward of 30°, the atmospheric response takes the form of inertia-gravity waves that can propagate long distances up- and outward from the coast (Rotunno 1983; Nielsen-Gammon 2001, 2002a,b). Sea breeze blows offshore during the day and onshore

---

* Part of this chapter is reprinted with permission from "Near-resonant ocean response to sea breeze on a stratified continental shelf" by X. Zhang, S. DiMarco, D. Smith, M. Howard, A. Jochens, and R. Hetland, *Journal of Physical Oceanography*, Copyright 2009 by American Meteorological Society.

at night south of 30°N on the middle Texas-Louisiana Shelf. This is counterintuitive with the traditional idea of onshore sea breeze during the day and offshore land breeze at night, but consistent with the previous theoretical and numerical simulations (Rotunno 1983; Yan and Anthes 1987).

(2) Considering the long east-west coastline, the near-resonant condition between local inertial and diurnal forcing frequencies makes the Gulf of Mexico particularly responsive to sea breeze forcing during summer. Wavelet analysis results indicate a strong correlation between the onset sea breeze forcing and subsequent near-inertial ocean response in the upper mixed layer during this period. The maximum near-inertial currents occur in June on the middle Texas-Louisiana Shelf despite the sea breeze peaks in August. In this dissertation, I use the wavelet analysis and hydrographic data to give an explanation of this apparent mismatch in phase of peak sea breeze (August) and peak near-inertial currents (June). It is mainly caused by two reasons. First, the in-phase relationship of sea breeze forcing and near-inertial currents can persist longer without interruptions in June compared to August, which allows for the near-inertial currents to have longer period to accumulate energy. Second, the ocean has a much shallower mixed layer in June (~ 3m) in comparison with August (~ 25m). The deepening of the mixed layer in August is mainly caused by the advection of the warmer and saltier water from the southwest portion of Texas-Louisiana Shelf upcoast to the middle Texas-Louisiana Shelf due to the change of prevailing wind direction in July (Nowlin et al. 2005; Nowlin et al. 1998; Cochrane and Kelly 1986; Cho et al. 1998).

(3) The Mississippi River discharge plays an important role in controlling the near-inertial ocean response to sea breeze forcing on the Texas-Louisiana Shelf and this can vary interannually during summer months. This is evidenced by the "great flood" of the Mississippi River in 1993. In summer 1993, the near-inertial current peak on the middle Texas-Louisiana Shelf is about one half to one third of that in 1992 and 1994 and the peak variance time is shifted forward for about one month. The Mississippi River discharge increases by about 50% in spring 1993 compared to the normal year. This large influx of fresh water reaches the mooring locations in June and contributes to the deepening of the mixed layer. The deepening of mixed layer depth weakens the near-inertial current variance in June 1993 and causes the shift of peak variance time.

(4) The sea breeze driven near-inertial currents could significantly enhance the vertical mixing on the Texas-Louisiana Shelf in summer as indicated by a reduction of the Richardson number. The bulk Richardson number calculated near the surface can be suppressed at least by a factor of 30 during strong near-inertial current events as compared to those periods when near-inertial responses are small. High vertical mixing associated with sea breeze is of particular interest in regions on the Texas-Louisiana Shelf where hypoxia is found (Wiseman et al. 1997; Hetland and DiMarco 2008).

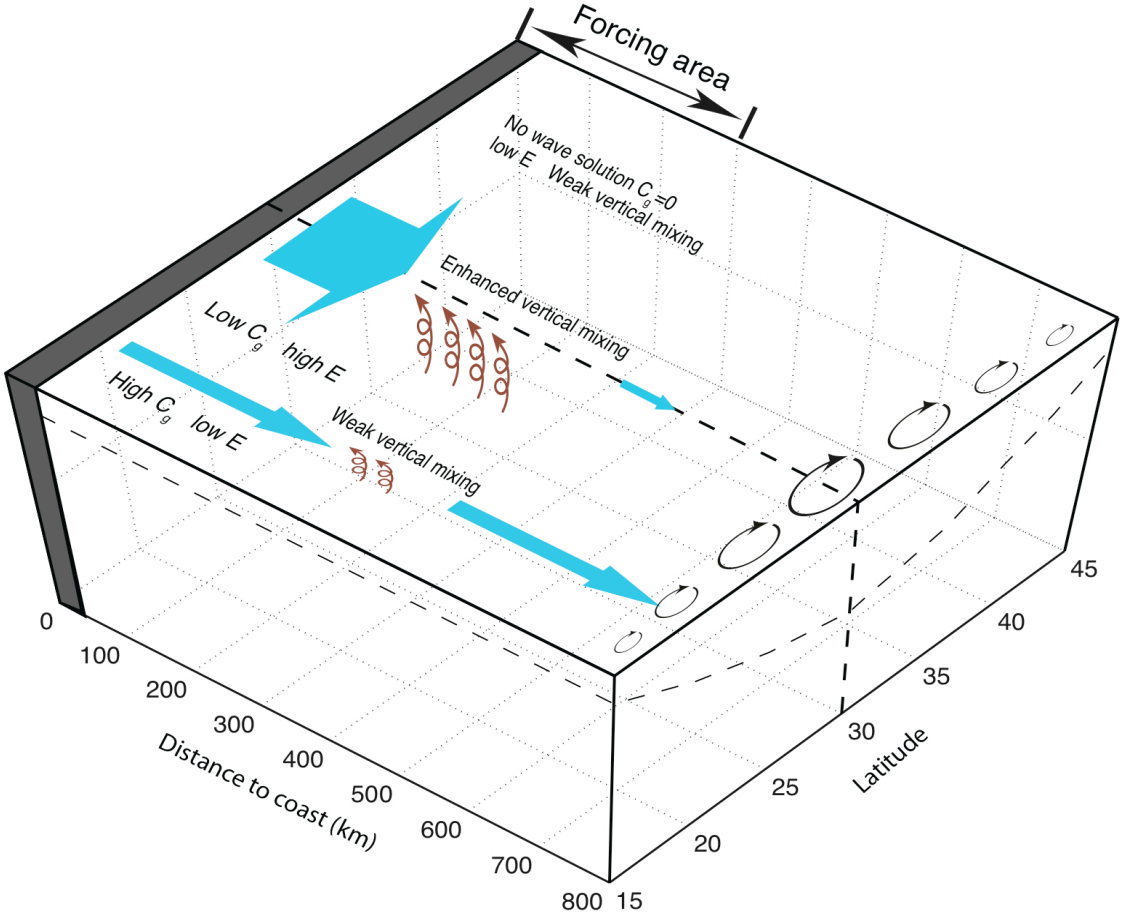

Fig. 6.1. A schematic diagram to summarize the latitudinal dependence of lateral propagation of sea breeze driven near-inertial motions, and explain the enhanced vertical mixing by sea breeze driven motions near the critical latitude. The blue arrows show the lateral energy flux by internal *Poincare* waves. The width and length of these blue arrows indicate the energy density (E) of the oceanic near-inertial response to sea breeze, and the magnitude of the group speed (C_g), respectively. The gray boundary is the location of the coast. The two near-coast arrows represent the lateral energy flux in the forcing area (maximum at 30°N; wind measurements indicate that sea breeze can extend at least 300 km offshore during summer). The two off-coast arrows represent the lateral flux outside the forcing area (maximum southward of 30°N). The radius of circle-arrows indicates the amount of energy input from sea breeze at different latitudes (maximum at 30°N). The upperward-pointing curvy arrows represent the amount of vertical mixing induced by sea breeze forcing at different latitudes (highest at 30°N). The gray-dashed line on the sidewall illustrates the latitudinal distribution of the mixed layer depth induced by sea breeze mixing effect (deepest at 30°N). North of 30°N, the internal *Poincare* wave does not exist. Therefore, the lateral energy flux is zero.

(5) Numerical simulations illustrate the latitudinal dependence of lateral propagation of sea breeze driven near-inertial motions, and explain the enhanced vertical mixing by these sea breeze driven motions at the critical latitude. Fig. 6.1 gives a schematic summary of the mechanisms and oceanic responses discussed in this research. The results indicate that the oceanic response to sea breeze is maximum at the critical latitude. The coastal generated near-inertial energy is trapped to the coast poleward of 30° latitude, however, equatorward of 30° latitude, it can propagate offshore in form of *Poincare* waves. The Gulf of Mexico is particularly well suited to investigate this phenomenon owing to its proximity to 30°N. The *Poincare* waves at 30° latitude have the characteristics of near-zero group speed, making them inefficient in transferring the maximum oceanic energy offshore. The lateral energy flux convergence plus the energy input from the wind is maximum near the critical latitude, and therefore more near-inertial energy dissipates near the coast and promotes vertical mixing near 30° latitude, consistent with previous observations on the northern shelf of the Gulf of Mexico. Equatorward of 30° latitude, the oceanic inertial response to sea breeze becomes much weaker. The coastal generated energy (albeit less) is efficiently moved offshore due to the increased group speed of *Poincare* waves. Therefore, the local dissipation is greatly reduced.

The propagation of *Poincare* waves is crucial for the understanding of physics of sea breeze driven near-inertial motions near the critical latitude. This effect cannot be neglected, and is a significant limitation of one-dimensional simulation of sea breeze near the critical latitude.

(6) Despite the fact that emphasis here is on the Texas-Louisiana Shelf, these results have significant applications for other coastal oceans near 30°N/S. Likely examples are the East China Sea where there is a broad shelf and large river inflow (Yangtze River), the Mid-Atlantic Bight region of the eastern U.S. coastline, and the Persian/Arabian Gulf.

In the real ocean, the background vorticity in the water column can change the effective *Coriolis* frequency by

$$f_{eff} = f + \eta/2,$$

where η denotes vorticity. In this case, the latitude resonant with sea breeze forcing could be shifted north or south. Therefore, the resonant latitudes may not be limited to near 30° latitude as reported in this research. This aspect may also be important, and warrants future investigation.

REFERENCES

Alford, M. H., 2003: Redistribution of energy available for ocean mixing by long-range propagation of internal waves. *Nature*, **423**, 159–162.

Aparna, M., S. R. Shetye, D. Shankar, S. S. C. Shenoi, P. Mahra, and R. G. P. Desai, 2005: Estimating the seaward extent of see breeze from QuikSCAT scatterometry. *Geophys. Res. Lett.*, **32**, L13601, doi:10.1029/2005GL023107.

Belabbassi, L., 2006: Examination of the relationship of river water to occurrences of the bottom water with reduced oxygen concentrations in northern Gulf of Mexico. Ph.D. dissertation, Texas A&M University, College Station, 119 pp.

Bunge, L., C. Provost, J. Lilly, M. D'Orgeville, A. Kartavtseff, and J. Melice, 2006: Variability of the horizontal velocity structure in the upper 1600 m of the water column on the equator at 10°W. *J. Phys. Oceanogr.*, **36**, 1287–1304.

Chen, C., and L. Xie, 1997: A numerical study of wind-induced, near-inertial oscillations over the Texas-Louisiana Shelf. *J. Geophys. Res.*, **102**(C7), 15583–15593.

Chen, C., R. O. Reid, and W. D. Nowlin, Jr., 1996: Near-inertial oscillations over the Texas-Louisiana Shelf. *J. Geophys. Res.*, **101**(C2), 3509–3524.

Cho, K., R. O. Reid, and W. D. Nowlin, Jr., 1998: Objectively mapped streamfunction fields on the Texas-Louisiana Shelf based on 32 months of moored current meter data. *J. Geophys. Res.*, **103**(C5), 10377–10390.

Cochrane, J. D., and F. J. Kelly, 1986: Low-frequency circulation on the Texas-Louisiana continental shelf. *J. Geophys. Res.*, **91**(C9), 10645–10659.

Craig, P. D., 1989a: Constant eddy-viscosity models of vertical structure forced by periodic winds. *Cont. Shelf Res.*, **9**, 343–358.

Craig, P. D., 1989b: A model of diurnally forced vertical current structure near 30° latitude. *Cont. Shelf Res.*, **9**, 965–980.

Davis, W. M., L. G. Schultz, and R. de C.Ward, 1890: An investigation of the sea breeze. *Ann. Observ. Astron. Harvard. Coll.*, **21**, 215–265.

DiMarco, S. F., and R. O. Reid, 1998: Characterization of the principal tidal current constituents on the Texas-Louisiana Shelf. *J. Geophys. Res.*, **103**(C2), 3092–3109.

DiMarco, S. F., A. E., Jochens, and M. K. Howard, 1997: LATEX shelf data report: current meter moorings, April 1992 through December 1994. Technical Report No. 97-01-T, 61 pp. plus appendices, Texas A&M University, Oceanography, College Station. (Available on CD-ROM NODC-88, *Texas-Louisiana Shelf Circulation and Transport Processes Study, Current Meter, Meteorological Buoy, XBT/XSV/XCP/CTD/IES Data and Reports*, 1992-1994)

DiMarco, S. F., M. K. Howard, and R. O. Reid, 2000: Seasonal variation of wind-driven diurnal current cycling on the Texas-Louisiana continental shelf. *Geophys. Res. Lett.*, **27**, 1017–1020.

DiMego, G. L., L. F. Bosart, and G. W. Endersen, 1976: An examination of the frequency and mean conditions surrounding frontal incursions into the Gulf of Mexico and Caribbean Sea. *Mon. Weather Rev.*, **104**, 708–718.

Dinnel, S. P., and W. J. Wiseman, Jr., 1986: Fresh water on the Louisiana and Texas Shelf. *Cont. Shelf Res.*, **9**, 765–784.

Etter, P. C., M. K. Howard, and J. D. Cochrane, 2004: Heat and freshwater budgets of the Texas-Louisiana Shelf. *J. Geophys. Res.*, **109**, C02024, doi:10.1029/2003JC001820.

Federiuk, J., and J. S. Allen, 1996: Model studies of near-inertial waves in flow over the Oregon continental shelf. *J. Phys. Oceanogr.*, **26**, 2053–2075.

Flather, R. A., 1976: A tidal model of the northwest European continental shelf. *Mem. Soc. R. Sci. Liege*, **10**(6), 141–164.

Foufoula-Georgiou, E., and P. Kumar (Eds.), 1995: *Wavelets in Geophysics*. Academic Press, 373 pp.

Furberg, M., D. G. Steyn, and M. Baldi, 2002: The climatology of sea breezes on Sardinia. *Int. J. Climatol.*, **22**, 917–932.

Gille, S. T., S. G. Llewellyn Smith, and S. M. Lee, 2003: Measuring the seabreeze from QuikSCAT scatterometry. *Geophys. Res. Lett.*, **30**, 1114, doi:10.1029/2002GL016230.

Gregg, M. C., 1989: Scaling turbulent dissipation in the thermocline. *J. Geophys. Res.*, **94**(C7), 9686–9698.

Gregg, M. C., T. B. Sanford, and D. P. Winkel, 2003: Reduced mixing from the breaking of internal waves in equatorial waters. *Nature*, **422**, 513–515.

Grinsted, A., J. C. Moore, and S. Jevrejeva, 2004: Application of the cross wavelet transform and wavelet coherence to geophysical time series. *Nonlinear Processes in Geophysics*, **11**, 561–566.

Helland-Hansen, B., and V. W. Ekman, 1931: Measurements of ocean currents (Experiments in the North Atlantic). *Kgl. Fysiiogr. Sallsk. Lund*, **1**.

Hetland, R. D., and L. Campbell, 2007: Covergent blooms of Karenia brevis along the Texas coast, *Geophys. Res. Lett.*, **34**, L19604, doi:10.1029/2007GL030474.

Hetland, R. D. and S. F. DiMarco, 2008: How does the character of oxygen demand control the structure of hypoxia on the Texas-Louisiana continental shelf. *J. Mar. Syst.*, **70**, 49–62.

Hibiya, T., M. Nagasawa, and Y. Niwa, 2002: Nonlinear energy transfer within the oceanic internal wave spectrum at mid and high latitudes. *J. Geophys. Res.*, **107**(C11), 3207, doi:10.1029/2003GL017998.

Howard, M. K., and S. F. DiMarco, 1998: LATEX shelf DATA report: Drifters and Miscellaneous Instruments, April 1992 through December 1994. TAMU Oceanography, Tech. Rpt. No. 98-2-T, 34 pp. plus appendices, Texas A&M University, College Station. (Available on CD-ROM NODC-88, *Texas-Louisiana*

Shelf Circulation and Transport Processes Study, Current Meter, Meteorological Buoy, XBT/XSV/XCP/CTD/IES Data and Reports, 1992-1994)

Hsu, S. A., 1972: Coastal air-circulation system: Observations and empirical model. *Mon. Weather Rev.*, **98**, 487–509.

Hunter, E., R. Chant, L. Bowers, S. Glenn, and J. Kohut, 2007: Spatial and temporal variability of diurnal wind forcing in the coastal ocean. *Geophys. Res. Lett.*, **34**, L03607, doi:10.1029/2006GL028945.

Hyder, P., J. H. Simpson, and S. Christopoulos, 2002: Sea-breeze forced diurnal surface currents in the Thermaikos Gulf, north-west Aegean. *Cont. Shelf Res.*, **22**, 585–601.

Kunze, E., L. K. Rosenfeld, G. S. Carter, and M. C. Gregg, 2002: Internal waves in Monterey Submarine Canyon. *J. Phys. Oceanogr.*, **32**, 1890–1913.

Leben, R. R., 2005: Altimeter-derived Loop Current metrics. In *Circulation in the Gulf of Mexico: Observations and Models,* AGU Geophysical Monograph Series 161, edited by W. Sturges and A. Lugo-Fernandez, pp. 181–201., AGU, Washington, D. C.

Liu, Y., X. S. Liang, and R. H. Weisberg, 2007: Rectification of the bias in the wavelet power spectrum. *J. Atmos. Oceanic. Technol.*, **24**, 2093–2102.

MacKinnon, J. A., and M. C. Gregg, 2003: Shear and baroclinic energy flux on the summer New England Shelf. *J. Phys. Oceanogr*. **33**, 1462–1475.

MacKinnon, J. A., and K. B. Winters, 2005: Subtropical catastrophe: significant loss of low-mode tidal energy at 28.9°N. *Geophys. Res. Lett.*, **32**, L15605, doi:10.1029/2005GL023376.

Masselink, G., and C. B. Pattiaratchi, 2001: Characteristics of the sea breeze system in Perth, Western Australia, and its effect on the nearshore wave climate. *J. Coastal Res.*, **17**, 173–187.

Milliman, J. D., and R.H. Meade, 1983: World-wide delivery of river sediment to the oceans, *J. Geol.,* **91**(1), 1–21.

Munk, W., and N. Philips, 1968: Coherence and hand structure of inertial motion in the sea. *Rev. Geophys.*, **6**, 447–472.

Munk, W., and C. Wunsch, 1998: Abyssal recipes: energetics of tidal and wind mixing. *Deep-Sea Res.*, **45**, 1977–2010.

Nash, J. D., M. H. Alford, and E. Kunze, 2005: On estimating internal-wave energy fluxes in the ocean. *J. Atmos. Oceanic. Technol.*, **22**, 1551–1570.

Nielsen-Gammon, J. W., 2001: Initial Modeling of the August 2000 Houston-Galveston Ozone Episode, Report to the Texas Natural Resource Conservation Commission (TNRCC). 71 pp. (Available from http://www.met.tamu.edu/results and http://www.tceq.state.tx.us)

Nielsen-Gammon, J. W., 2002a: Evaluation and Comparison of Preliminary Meteorological Modeling for the August 2000 Houston-Galveston Ozone Episode.

Report to TNRCC, 83 pp. (Available from http://www.met.tamu.edu/results and http://www.tceq.state.tx.us)

Nielsen-Gammon, J. W., 2002b: Meteorological Modeling for the August 2000 Houston-Galveston Ozone Episode: PBL Characteristics, Nudging Procedure, and Performance Evaluation. Report to TNRCC, 109 pp. (Available from http://www.met.tamu.edu/results and http://www.tceq.state.tx.us)

Nowlin, W. D., Jr., A. E. Jochens, S. F. DiMarco, R. O. Reid, and M. K. Howard, 2001: Deepwater physical oceanography reanalysis and synthesis of historical data: Synthesis Report, OCS Study MMS 2001-064, 528 pp., U.S. Dept. of the Interior, Minerals Management Service, Gulf of Mexico OCS Region, New Orleans.

Nowlin, W. D., Jr., A. E. Jochens, S. F. DiMarco, R. O. Reid and M. K. Howard, 2005: Low-frequency circulation over the Texas-Louisiana continental shelf. In *Circulation in the Gulf of Mexico: Observations and Models,* AGU Geophysical Monograph Series 161, edited by W. Sturges and A. Lugo-Fernandez, pp. 219–240., AGU, Washington, D. C.

Nowlin, W. D., Jr., A. E. Jochens, R. O. Reid, and S. F. DiMarco, 1998: Texas-Louisiana Shelf Circulation and Transport Processes Study: Synthesis Report. Volume I: Technical Report. OCS Study MMS 98-0035. 502 pp., U.S. Dept. of the Interior, Minerals Management Service, Gulf of Mexico OCS Region, New Orleans.

Oey, L-Y., 1995: Eddy- and wind-forced shelf circulation. *J. Geophys. Res.*, **100**(C5), 8621–8637.

Orlic, M., 1987: Oscillations at the inertial period on the Adriatic Sea Shelf. *Cont. Shelf. Res.*, **7**, 577–598.

Pawlowicz, R., B. Beardsley, and S. Lentz, 2002: Classical tidal harmonic including error estimates in MATLAB using T-TIDE. *Comput. Geosci.*, **28**, 929–937.

Pedlosky, J., 1987: *Geophysical Fluid Dynamics*. 2nd ed. Springer-Verlag, 710 pp.

Price, J. F., R. A. Weller, and R. Pinkel, 1986: Diurnal cycling: observations and models of the upper ocean response to diurnal heating, cooling, and wind mixing. *J. Geophys. Res.*, **91**(C7), 8411–8427.

Rabalais, N. N., R. E. Turner, B. K. Sen Gupta, D. F. Boesch, P. Chapman, and M. C. Murrell, 2007: Hypoxia in the northern Gulf of Mexico: does the science support the plan to reduce, mitigate, and control hypoxia. *Estuaries and Coasts*, **30**(5), 753–772.

Rippeth, T. P., J. H. Simpson, R. J. Player, and M. Garcia, 2002: Current oscillations in the diurnal-inertial band on the Cataloninan Shelf in spring. *Cont. Shelf Res.*, **22**, 247–265.

Rosenfeld, L. K., 1988: Diurnal period wind stress and current fluctuations over the continental shelf off northern California. *J. Geophys. Res.*, *93*(C3), 2257–2276.

Rotunno, R., 1983: On the linear theory of the land and see breeze. *J. Atmos. Sci.*, **40**, 1999–2009.

Schott, F. A., M. Dengler, R. Zantopp, L. Stramma, J. Fischer, and P. Brandt, 2005: The shallow and deep western boundary circulation of the south Atlantic at 5° - 11° S. *J. Phys. Oceanogr.*, **35**, 2031–2053.

Shchepetkin, A. F., and J. C. McWilliams, 2005: The regional oceanic modeling system (ROMS): a split-explicit, free-surface, topographically-following-coordinate oceanic model. Ocean Model, **9**, 347–404.

Simmons, H. L., R. W. Hallberg, and B. K. Arbic, 2004: Internal wave generation in a global baroclinic tide model. *Deep Sea Res., Part II*, **51**, 3043–3068.

Simpson, J. E., 1994: *Sea Breeze and Local Wind*. Cambridge University Press, 234 pp.

Simpson, J. H., T. P. Rippeth, P. Hyder and I. M. Lucas, 2002: Forced oscillations near the critical latitude for diurnal-inertial resonance. *J. Phys. Oceanogr.*, **22**, 177–187.

Solis, R. S., and G. L. Powell, 1999: Hydrography, mixing characterisctics, and residense times of Gulf of Mexico estuaries. in *Biochemistry of Gulf of Mexico estuaries*, edited by T. S. Bianchi, J. R. Pennock, and R. R. Twilley, pp. 29-61, John Wiley and Sons, New York.

Sturges, W., and R. R. Leben, 2000: Frequency of ring separations from the Loop Current in the Gulf of Mexico: A revised estimate. *J. Phys. Oceanogr.*, **30**, 1814–1818.

Sturges, W., A. Lugo-Fernandez, and M. D. Shargel, 2005: Introduction to circulation in the Gulf of Mexico. In *Circulation in the Gulf of Mexico: Observations and Models,*

AGU Geophysical Monograph Series 161, edited by W. Sturges and A. Lugo-Fernandez, pp. 1–10., AGU, Washington, D. C.

Tintore, J., D. -P. Wang, E. Garcia, and A. Viudez, 1995: Near-inertial motions in the coastal ocean. *J Mar. Syst.*, **6**, 301–312.

Torrence, C. and G. P. Compo, 1998: A practical guide to wavelet analysis. *Bull. Amer. Meteor. Soc.*, **79**, 61–78.

Torrence, C., and P. J. Webster, 1999: Interdecadal changes in the ENSO-Monsoon System. *J. Climate*, **12**, 2679–2690.

Turner, R. E., and N. N. Rabalais, 1994: Coastal eutrophication near the Mississippi River delta. *Nature*, **368**, 619–621.

Umlauf, L., and H. Burchard, 2003: A generic length-scale equation for geophysical turbulence models. *J. Mar. Res.*, 61, 235–265.

van Haren, H., 2005: Tidal and near-inertial peak variations around the diurnal critical latitude. *Geophys. Res. Lett.*, **32**, L23611, doi:10.1029/2005GL024160.

van Haren, H., 2007: Longitudinal and topographic variations in North Atlantic tidal and inertial energy around latitudes 30 ± 10° N. *J. Geophys. Res.*, **112**, C10020, doi:10.1029/2007JC004193.

Walker, N. D., G. S. Fargion, L. J. Rouse, and D. C. Biggs, 1994: The great flood of summer 1993: Mississippi River discharge studied. *Eos Trans. AGU*, **75**(36), 409.

Wang, W., M. K. Howard, W. D. Nowlin, Jr., and R. O. Reid, 1996: LATEX shelf DATA report: Meteorological, April 1992 through December 1994. TAMU Oceanography, Tech. Rpt. No. 96-2-T, 34 pp. plus appendices, Texas A&M University, College Station. (Available on CD-ROM NODC-88, *Texas-Louisiana Shelf Circulation and Transport Processes Study, Current meter, meteorological buoy, XBT/XSV/XCP/CTD/IES Data and Reports*, 1992-1994)

Wang, W., W. D. Nowlin, and R.O. Reid, 1998: Analyzed surface meteorological fields over the northwestern Gulf of Mexico for 1992-2004: mean, seasonal, and monthly patterns. *Mon. Wea. Rev.*, **126** (11), 2864–2883.

Webster, F., 1968: Observations of inertial period motions in the deep sea. *Rev. Geophys.*, **6**, 473–490.

Wiseman, W. J., N. N. Rabalais, R. E. Turner, S. P. Dinnel and A. MacNaughton, 1997: Seasonal and interannual variability within the Louisiana coastal current: stratification and hypoxia. *J. Mar. Syst.*, **12**, 237–248.

Xing, J., A. M. Davies, and P. Fraunie, 2004: Model studies of near-inertial motion on the continental shelf off northwest Spain: a three-dimensional/two-dimensional/one-dimensional model comparison study. *J. Geophys. Res.,* **109***,* C01017, doi:10.1029/2003JC001822.

Yan, H., and R. A. Anthes, 1987: The effect of latitude on sea breeze. *Mon. Weather Rev.*, **115**, 936–956.

Zhang, X., S. F. DiMarco, D. C. Smith, IV, M. K., Howard, A. E. Jochens, and R. D. Hetland, 2008: Near-resonant ocean response to sea breeze on a stratified continental shelf. *Journal of Physical Oceanography*, accepted.

Zhang, X., D. C. Smith, IV, S. F. DiMarco, and R. D. Hetland, 2009: Sea breeze driven ocean *Poincare* wave propagation and mixing near the critical latitude with application to the Gulf of Mexico. *Journal of Physical Oceanography*, submitted.

VITA

Name: Xiaoqian Zhang

Address: Department of Oceanography, 3146 TAMU, College Station, TX 77843-3146

Email Address: zhangxiaoqianok@hotmail.com

Education: B.S., Oceanography, Ocean University of China, 2002
M.S., Physical Oceanography, Ocean University of China, 2005
Ph.D., Physical Oceanography, Texas A&M University, 2009